12-2021

Investigation of Iron-Nickel Films Based Catalysts: Controlling Hydrogen Evolution Reaction (HER) Through an Electrode-Electrolyte Engineering Approach

Sergio Ivan Perez Bakovic
University of Arkansas, Fayetteville

Investigation of Iron-Nickel Films Based Catalysts: Controlling Hydrogen Evolution Reaction (HER) Through an Electrode-Electrolyte Engineering Approach

A dissertation submitted in the partial fulfillment
of the requirements for the degree of
Doctor of Philosophy in Engineering with a concentration in Chemical Engineering

by

Sergio I. Perez Bakovic
University of Central Arkansas
Bachelor of Science in Chemistry, 2014

December 2021
University of Arkansas

This dissertation is approved for recommendation to the Graduate Council.

_____
Lauren Greenlee, PhD
Dissertation Director

_____
Jingyi Chen, PhD
Committee Member

_____
Robert Coridan, PhD
Committee Member

_____
Greg Thoma, PhD
Committee Member

_____
David M. Ford, PhD
Committee Member

Abstract

Electrochemical energy conversion technologies need to be economically viable in order to be adopted. Earth-abundant transition metals (i.e., Fe, Co, and Ni) have attracted attention due to their high availability, low cost, and catalytic characteristics that are in many cases found in and exploited by nature. Herein, we synthesize $Fe_xNi_{100-x}O_y$ electrocatalyst films and study how the electrocatalyst-electrolyte interactions alter the hydrogen evolution reaction (HER).

In this work, $Fe_xNi_{100-x}O_y$ films were synthesized to study the composition, chemical state, and morphology. Characterization results provided a well-established electrocatalyst film platform to then proceed with electrochemical evaluations. The effects of the electrode composition and electrochemically active surface area on HER current density and overpotential were initially evaluated in alkaline electrolyte. We found that the HER activity of $Fe_xNi_{100-x}O_y$ films is greatly influenced by the active surface area, which is dependent on the composition. Therefore, the HER activities observed for the electrodeposited $Fe_xNi_{100-x}O_y$ films can be attributed to changes in surface area, rather than by an enhancement of the intrinsic catalytic activity of the components. To further build on our work, we studied the effects of the alkaline electrolyte composition for the application of $Fe_xNi_{100-x}O_y$/Si films.

A simple two-sided electrode was used, one side composed of a $Fe_xNi_{100-x}O_y$ film, and another composed of Si, were evaluated in LiOH, NaOH, and KOH. The $Fe_xNi_{100-x}O_y$ was implemented as the electrocatalyst, while the Si was used as a substrate and as a method to enhance hydrogen production. The electrodes were evaluated using electrochemical methods coupled with the quantification of hydrogen both with applied voltage and at open circuit voltage. The activation of Si was only demonstrated in 0.1 M KOH and NaOH but not in LiOH under the time scales studied. At the same time the $Fe_{80}Ni_{20}$/Si system performed at lower overpotential and allowed

the faster activation of Si to boost the production of hydrogen compared to $Fe_{20}Ni_{80}$/Si. The results demonstrate that the $Fe_xNi_{100-x}O_y$ composition and the electrolyte composition influence the performance of the $Fe_xNi_{100-x}O_y$/Si system.

Next, we investigated the application of $Fe_xNi_{100-x}O_y$ electrodes in neutral buffered conditions, 0.1 M sodium phosphate at pH of 7.2. The surface chemistry was studied post-electrochemistry with x-ray photoelectron spectroscopy (XPS). At the same time, the HER electrochemical activity and hydrogen production were evaluated for different $Fe_xNi_{100-x}O_y$ electrodes. The post-electrochemistry surface chemistry analysis demonstrates a compositional dependence of the $Fe_xNi_{100-x}O_y$ electrocatalyst on electrolyte species chemical deposition during electrocatalytic HER studies. Deposition of both sodium and phosphate were observed at high iron content compositions. At the same time, the electrochemical activity, hydrogen production, and faradaic efficiency were demonstrated to be dependent on the $Fe_xNi_{100-x}O_y$ composition under neutral buffered conditions.

Acknowledgments

I would like to thank my advisor, Dr. Lauren Greenlee. Without her guidance, support, patience, mentorship, and encouragement, none of this work would have been possible over the past years. I will forever be grateful for trusting in me and allowing me to have this fantastic opportunity to work on my Ph.D. along her side.

I would also like to thank my committee members, Dr. Jingyi Chen, Dr. Robert Coridan, Dr. Greg Thoma, and Dr. David M. Ford for their encouragement, insightful comments, and fantastic suggestions. I would like to express my gratitude to Dr. Heather L. Walker, Dr. Shannon Servoss, Dr. Jingyi Chen, and Dr. Robert Coridan for always making time to help me.

My sincere thanks to Dr. Mourad Benamara, Erik D. Pollok, and Dr. Clemens Heske for opening their laboratories and allowing me to collaborate with their groups. A special thanks must be given to Dr. Jingyi Chen for taking me in as one of her graduate students and for all her help, especially during my last semester. I would also like to thank my friends and colleagues in the Greenlee lab; it has been my pleasure to work and learn together over the years.

I would also like to give a special thanks to Dr. Katherine Ayers, Christopher Capuano, Dr. Diana De Porcellinis, and Alex Keane for their mentorship and kind welcoming during my internship at Nel.

Lastly, I would like to thank my family for their unconditional support and love.

Table of Contents

List of Published Papers

Chapter 2 (Published):

Perez Bakovic, S. I., Acharya, P., Watkins M., Thornton H., Hou S., and Greenlee, L. F. Electrochemically Active Surface Area Controls HER Activity for Fe_xNi_{100-x} Films in Alkaline Electrolyte. *J Catalysis*, (Submitted August 2020).

Further permissions related to the material excerpted should be directed to J. Catal.

1. Chapter 1. Introduction

1.1 Water Electrolysis

As the adoption of renewable energy increases, the challenge is to find methods to store the energy generated from intermittent sources to regulate energy distribution as needed.[1-4] Electrochemical processes that allow the storage of electrical energy in the form of chemical energy have been proposed as large-scale solutions. Specifically, the use of electrical energy generated from renewable resources can be used to produce energy-rich molecules (hydrogen, ammonia, and methanol).[1,2,5]

Hydrogen has been proposed as the fuel of the future and the basis for a hydrogen economy. The high specific energy, around 120 MJ/kg, a high abundance of hydrogen element, and no CO_2 emissions during consumption have made hydrogen an attractive solution to creating an environment-friendly economy.[6] However, besides hydrogen being proposed as an energy carrier, hydrogen is nowadays used in many industrial applications. Currently, most hydrogen is produced through steam reforming, which depends on fossil fuels and has a large carbon footprint.[7,8] Water electrolysis is an alternative process to produce hydrogen that does not emit CO_2 and can be fully powered by renewable energies.[8] Electrolyzers can be directly coupled with electric power generated from renewable energy sources to produce hydrogen and oxygen from water.[1,9] The energy consumption of electrolyzers depends on the cell voltage needed to drive both half-reactions, the hydrogen evolution reaction (HER) and oxygen evolution reaction (OER).[10,11]

1.2 Hydrogen Evolution Reaction (HER)

Hydrogen production through electrochemical water splitting is powered by electrical energy input. The minimum theoretical voltage required to drive water-splitting is 1.23 V at room

temp.[12] The electrochemical water splitting reaction involves two half-reactions: 1) the hydrogen evolution reaction (HER) and 2) the oxygen evolution reaction (OER). The HER and OER half-reactions are:

In acid:

$$HER: \quad 4H_3O^+ + 4e^- \rightarrow 2H_2 + 4H_2O$$

$$OER: \quad 6H_2O \rightarrow O_2 + 4H_3O^+ + 4\,e^-$$

In base:

$$HER: \quad 4H_2O + 4\,e^- \rightarrow 2H_2 + 4\,OH^-$$

$$OER: \quad 4OH^- \rightarrow O_2 + 2H_2O + 4\,e^-$$

The reaction rate can be increased; however, increasing the reaction rate requires additional energy. The term overpotential defines the additional voltage that must be applied to obtain a current density.[12] Electrocatalysts are implemented to reduce the overpotential, thus achieving high reaction rates with lower energy requirements.

1.3 Iron-Nickel based electrocatalyst for HER

Technological efforts have been focused on the development of electrocatalysts to reduce the required cell voltage, thus lowering the cost. When it comes to HER, platinum (Pt) is considered one of the best catalysts.[11,13] However, the high cost and scarcity make noble metals as Pt hard to be considered for large-scale applications. A lower-cost electrocatalyst alternative are earth-abundant transition metals as Ni, Fe, and Co. However, earth-abundant transition metals have lower activity compared to Pt catalysts.

Different techniques have been developed and used to increase the activity and stability of catalysts as the development of alloys and the increase in active surface area. The increase in the intrinsic catalytic activity and long-term stability has been demonstrated in Ni-based alloys by the incorporation of molybdenum (Mo),[14] cobalt (Co),[15] and iron (Fe)[16]. On the other hand, HER activity can be greatly enhanced by increasing the electrochemical surface area (ECSA) of Ni catalysts by the incorporation of nano-structuring.[17] The increase in the catalytic surface area has also been demonstrated to occur through the incorporation of other components, ultimately leading to an increase in HER.[14,18,19] Therefore, techniques that increase the active surface area and the intrinsic electroactivity can be used in order to increase the efficiency of hydrogen production.

1.4 HER in neutral buffered conditions

Electrolyte components, once considered to be simply spectator ions (anions and cations), have gained attention as these components have been shown to influence electrochemical reactions.[20-22] In particular, extensive work has demonstrated that cations and anions affect the electrochemical reduction reactions of CO_2.[23,24] More recently, studies have implicated cations and anions in roles ranging from mediating nitrogen reduction[25,26] to acting as a source of protons[24] for reduction reactions. As stated by Waegele et al.,[22] the electrolyte (i.e., solvent, cation, anion) and electrode define the liquid/solid interface, thus setting the catalytic properties.

Historically, HER studies have been performed in acidic or alkali electrolytes; however, few studies have been performed in neutral electrolyte conditions.[27,28] Interest in neutral pH conditions has attracted attention as the milder conditions provide safety advantages,[29] prevent the corrosion of materials,[30] and potentially allow the use of seawater overall,[27] reducing the cost of H_2 production.[31]

The mechanism of the HER under neutral conditions is still under debate. HER in neutral conditions is more complicated than traditional acid or alkaline conditions as it is believed that both H_2O molecules and dissociated H_3O^+ ions participate.[32] Therefore, the HER in neutral electrolytes is considered to follow a two-step reduction process.[21,33-35] Neutral buffer electrolytes have been proposed to be able to hold the local surface pH. It has been proposed that buffer electrolytes allow the system to: 1) replenish the H_3O^+ ions through the buffering mechanism of the electrolyte components and 2) provide H_3O^+ by the direct decomposition of phosphate ions on the electrode surface or through the release of protons at the electrode surface.[29,32] An understanding of the electrode-electrolyte interface can open up the possibility of engineering based on the needs to either boost or suppress the HER.

1.5 Reduction reactions for the conversion and storage of renewable energy

Today, there is a need for alternative technologies for energy conversion and storage. There is a growing interest as to whether an electrochemically-based system may succeed as a replacement for technologies that depend on hydrocarbons. In addition to hydrogen, electrocatalytic reduction reactions of carbon dioxide (CO_2),[36] and nitrogen (N_2)[37] have attracted attention as sustainable methods to create alternative fuels and chemicals of added value, including methane and ammonia.

Ammonia is considered a future fuel alternative and hydrogen storage molecule. Currently, ammonia is essential to the global economy as a fertilizer feedstock, industrial and household chemical, and chemical precursor. The supply of abundant and low-cost NH_3 production is essential to provide a stable and affordable food supply. Currently, 500 million tons of NH_3 per year, through the Haber-Bosch process (HBP).[38] In the HBP, a mixture of hydrogen gas (H_2) and nitrogen gas, termed synthetic gas, are required to produce NH_3. H_2 is produced through

steam reforming of coal and/or natural gas, a process that results in the production of 1.87 tons of the greenhouse gas carbon dioxide (CO_2) per 1 ton of NH_3.[39] An alternative method to produce NH_3 is the electrochemical nitrogen reduction reaction (NRR).[40] The synthesis of ammonia through the electrochemical reduction of N_2 and H_2O would provide the advantage of eliminating fossil fuels and could be powered by the integration with other renewable energy technologies.

Hydrocarbons and alcohols (i.e., methanol, ethylene, ethanol) are the desired products from the electrochemical CO_2 reduction reaction (CO2RR) as they are molecules of high energy density.[36,41] With the increasing concerns with the rise of CO_2 atmospheric concentration, methods to lower the CO_2 atmospheric concentrations through the reduction of CO_2 emissions, usage, and storage of CO_2 are required.[36,41] CO_2 reduction is considered a means of reducing the atmospheric CO_2 concentration through the usage of CO_2 to produce fuels or molecules of added value.[41] Thus, in addition to producing alternative fuels, CO2RR has gained a lot of attention as it has the potential of mitigating the unbalance humans have created in the carbon cycle.

The electrochemical catalysis community has, for the most part, made incremental progress towards enabling efficient electrochemical N_2 and CO_2 reduction, although efforts are plagued by low Faradaic efficiencies and low production rates. Theoretically, NRR and CO2RR should proceed as a negative potential is applied. However, kinetics favor HER, as HER only requires two electrons per H_2 compared to the multi-step reductions required to produce NH_3 and CH_3OH, which both require 6 e^- per molecule.[42,43] Thus, the HER dominates electrocatalytic surfaces in aqueous systems at reducing potentials, thus becoming the overriding competitive side reaction to all electroreduction processes (i.e., NRR and CO2RR). Electrochemical reduction reactions other than HER become almost impossible and impractical due to the low

efficiencies. Therefore, it is clear that one of the primary challenges that must be solved to enable electrocatalytic ammonia or methanol synthesis is the understanding of the HER.

References

1 Lewis, N. S. & Nocera, D. G. Powering the planet: Chemical challenges in solar energy utilization. *Proceedings of the National Academy of Sciences* **103**, 15729-15735 (2006).

2 Gray, H. B. Powering the planet with solar fuel. *Nature chemistry* **1**, 7-7 (2009).

3 Buttler, A. & Spliethoff, H. Current status of water electrolysis for energy storage, grid balancing and sector coupling via power-to-gas and power-to-liquids: A review. *Renewable and Sustainable Energy Reviews* **82**, 2440-2454 (2018).

4 Marcy, C. *U.S. renewable electricity generation has doubled since 2008*, <https://www.eia.gov/todayinenergy/detail.php?id=38752> (2019).

5 Wang, G., Mitsos, A. & Marquardt, W. Conceptual design of ammonia-based energy storage system: System design and time-invariant performance. *AIChE Journal* **63**, 1620-1637 (2017).

6 Abe, J. O., Popoola, A. P. I., Ajenifuja, E. & Popoola, O. M. Hydrogen energy, economy and storage: review and recommendation. *International journal of hydrogen energy* **44**, 15072-15086 (2019).

7 Crabtree, G. W., Dresselhaus, M. S. & Buchanan, M. V. The hydrogen economy. *Physics today* **57**, 39-44 (2004).

8 Holladay, J. D., Hu, J., King, D. L. & Wang, Y. An overview of hydrogen production technologies. *Catalysis today* **139**, 244-260 (2009).

9 Grigoriev, S. A., Fateev, V. N., Bessarabov, D. G. & Millet, P. Current status, research trends, and challenges in water electrolysis science and technology. *International Journal of Hydrogen Energy* (2020).

10 Li, X., Hao, X., Abudula, A. & Guan, G. Nanostructured catalysts for electrochemical water splitting: current state and prospects. *Journal of Materials Chemistry A* **4**, 11973-12000 (2016).

11 Zeng, K. & Zhang, D. Recent progress in alkaline water electrolysis for hydrogen production and applications. *Progress in Energy and Combustion Science* **36**, 307-326, doi:http://dx.doi.org/10.1016/j.pecs.2009.11.002 (2010).

12 Roger, I., Shipman, M. A. & Symes, M. D. Earth-abundant catalysts for electrochemical and photoelectrochemical water splitting. *Nature Reviews Chemistry* **1**, 1-13 (2017).

13 Gong, M., Wang, D.-Y., Chen, C.-C., Hwang, B.-J. & Dai, H. A mini review on nickel-based electrocatalysts for alkaline hydrogen evolution reaction. *Nano Res.* **9**, 28-46 (2016).

14 Csernica, P. M. *et al.* Electrochemical hydrogen evolution at ordered Mo7Ni7. *ACS Catal.* **7**, 3375-3383 (2017).

15 Yin, X. *et al.* 3D hierarchical network NiCo2S4 nanoflakes grown on Ni foam as efficient bifunctional electrocatalysts for both hydrogen and oxygen evolution reaction in alkaline solution. *International Journal of Hydrogen Energy* **42**, 25267-25276 (2017).

16 Ganesan, P., Sivanantham, A. & Shanmugam, S. Inexpensive electrochemical synthesis of nickel iron sulphides on nickel foam: super active and ultra-durable electrocatalysts for alkaline electrolyte membrane water electrolysis. *Journal of Materials Chemistry A* **4**, 16394-16402 (2016).

17 Ahn, S. H. *et al.* Electrodeposited Ni dendrites with high activity and durability for hydrogen evolution reaction in alkaline water electrolysis. *Journal of Materials Chemistry* **22**, 15153-15159 (2012).

18 Hu, C.-C. & Wu, Y.-R. Bipolar performance of the electroplated iron–nickel deposits for water electrolysis. *Materials chemistry and physics* **82**, 588-596 (2003).

19 Müller, C. I. *et al.* The activity of nanocrystalline Fe-based alloys as electrode materials for the hydrogen evolution reaction. *Journal of Power Sources* **304**, 196-206 (2016).

20 Exner, K. S. Electrolyte Engineering as a Key Strategy Towards a Sustainable Energy Scenario? *ChemElectroChem* **7**, 594-595 (2020).

21 Shinagawa, T. & Takanabe, K. Towards versatile and sustainable hydrogen production through electrocatalytic water splitting: electrolyte engineering. *ChemSusChem* **10**, 1318 (2017).

22 Waegele, M. M., Gunathunge, C. M., Li, J. & Li, X. How cations affect the electric double layer and the rates and selectivity of electrocatalytic processes. *The Journal of chemical physics* **151**, 160902 (2019).

23 Resasco, J. *et al.* Promoter effects of alkali metal cations on the electrochemical reduction of carbon dioxide. *Journal of the American Chemical Society* **139**, 11277-11287 (2017).

24 Resasco, J., Lum, Y., Clark, E., Zeledon, J. Z. & Bell, A. T. Effects of anion identity and concentration on electrochemical reduction of CO2. *ChemElectroChem* **5**, 1064-1072 (2018).

25 Lazouski, N., Schiffer, Z. J., Williams, K. & Manthiram, K. Understanding continuous lithium-mediated electrochemical nitrogen reduction. *Joule* **3**, 1127-1139 (2019).

26 Lazouski, N., Chung, M., Williams, K., Gala, M. L. & Manthiram, K. Non-aqueous gas diffusion electrodes for rapid ammonia synthesis from nitrogen and water-splitting-derived hydrogen. *Nature Catalysis* **3**, 463-469 (2020).

27 Lu, X. *et al.* A sea-change: manganese doped nickel/nickel oxide electrocatalysts for hydrogen generation from seawater. *Energy & Environmental Science* **11**, 1898-1910 (2018).

28 Zhang, W. *et al.* Single-crystalline (FexNi1-x) 2P nanosheets with dominant {011^{-} 1^{-}} facets: Efficient electrocatalysts for hydrogen evolution reaction at all pH values. *Nano Energy* **56**, 813-822 (2019).

29 Murthy, A. P., Govindarajan, D., Theerthagiri, J., Madhavan, J. & Parasuraman, K. Metal-doped molybdenum nitride films for enhanced hydrogen evolution in near-neutral strongly buffered aerobic media. *Electrochimica Acta* **283**, 1525-1533 (2018).

30 Ďurovič, M., Hnát, J. & Bouzek, K. Electrocatalysts for the hydrogen evolution reaction in alkaline and neutral media. A comparative review. *Journal of Power Sources* **493**, 229708 (2021).

31 Shinagawa, T. & Takanabe, K. New insight into the hydrogen evolution reaction under buffered near-neutral pH conditions: Enthalpy and entropy of activation. *The Journal of Physical Chemistry C* **120**, 24187-24196 (2016).

32 Zhou, Z. *et al.* Electrocatalytic hydrogen evolution under neutral pH conditions: current understandings, recent advances, and future prospects. *Energy & Environmental Science* **13**, 3185-3206 (2020).

33 Shinagawa, T., Garcia-Esparza, A. T. & Takanabe, K. Mechanistic switching by hydronium ion activity for hydrogen evolution and oxidation over polycrystalline platinum disk and platinum/carbon electrodes. *ChemElectroChem* **1**, 1497-1507 (2014).

34 Shinagawa, T. & Takanabe, K. Electrocatalytic hydrogen evolution under densely buffered neutral pH conditions. *The Journal of Physical Chemistry C* **119**, 20453-20458 (2015).

35 Katsounaros, I. *et al.* The effective surface pH during reactions at the solid–liquid interface. *Electrochemistry communications* **13**, 634-637 (2011).

36 Qiao, J., Liu, Y., Hong, F. & Zhang, J. A review of catalysts for the electroreduction of carbon dioxide to produce low-carbon fuels. *Chemical Society Reviews* **43**, 631-675 (2014).

37 Foster, S. L. *et al.* Catalysts for nitrogen reduction to ammonia. *Nature Catalysis* **1**, 490-500, doi:10.1038/s41929-018-0092-7 (2018).

38 Montoya, J. H., Tsai, C., Vojvodic, A. & Norskov, J. K. The Challenge of Electrochemical Ammonia Synthesis: A New Perspective on the Role of Nitrogen Scaling Relations. *ChemSusChem* **8**, 2180-2186, doi:10.1002/cssc.201500322 (2015).

39 Strait, R. & Negvekar, M. Carbon dioxide capture and storage in the nitrogen and syngas industries. Nitrogen + Syngas 2010, 303, 1−3 (Jan−Feb) at http://www.kbr.com/Newsroom/Publications/Articles/Carbon-Dioxide-Capture-and-Storage-in-the-Nitrogen-SyngasIndustries.pdf. (2010).

40 Lipman, T. & Shah, N. Ammonia as an alternative energy storage medium for hydrogen fuel cells: scientific and technical review for near-term stationary power demonstration projects Final report UC Berkeley Transportation Sustainability Research Centre, Institute of Transportation Studies (UCB), UC Berkeley (11-01-2007) Available at: http://www.escholarship.org/uc/item/7z69v4wp.

41 Mikkelsen, M., Jørgensen, M. & Krebs, F. C. The teraton challenge. A review of fixation and transformation of carbon dioxide. *Energy & Environmental Science* **3**, 43-81 (2010).

42 Qing, G. *et al.* Recent Advances and Challenges of Electrocatalytic N2 Reduction to Ammonia. *Chemical Reviews* (2020).

43 Kortlever, R., Shen, J., Schouten, K. J. P., Calle-Vallejo, F. & Koper, M. T. M. Catalysts and reaction pathways for the electrochemical reduction of carbon dioxide. *The journal of physical chemistry letters* **6**, 4073-4082 (2015).

2. Chapter 2. The role of Fe_xNi_{100-x} electrocatalyst composition on the hydrogen evolution reaction in alkaline medium

Authors: Perez Bakovic, S. I., Acharya, P., Watkins M., Thornton H., Hou S., and Greenlee, L. F. Electrochemically Active Surface Area Controls HER Activity for Fe_xNi_{100-x} Films in Alkaline Electrolyte. *J Catalysis*, (Submitted August 2020).

Abstract

The synthesis and electrocatalytic activity of Fe_xNi_{100-x} electrochemically deposited films were investigated. Films were evaluated for the hydrogen evolution reaction (HER) in alkaline media with respect to composition and electrochemically active surface area (ECSA). Results demonstrate that films of higher or equal Fe content had an ECSA tenfold greater than films with higher Ni. When normalized by geometric surface area, $Fe_{50}Ni_{50}$ films required the lowest overpotential of -390 mV to reach a current density of -10 mA cm^{-2}. However, when normalized by the ECSA, intrinsic HER activity increases as Ni content increases. Tafel slope, ECSA, microscopy, and impedance spectroscopy analyses allow a decoupled analysis of surface area versus activity effects on overall measured HER activity. These analyses collectively demonstrate that the increase in electrocatalytic activity is attributed to the increase in ECSA and not to an enhancement in the intrinsic activity by Fe and Ni component interactions.

Keywords: electrodeposition, iron, nickel, films, alkaline, hydrogen evolution reaction, electrochemically active surface area, intrinsic activity.

2.1 Introduction

The conversion of renewable energy (solar and wind) to electrical energy has increased, nearly doubling from 2008 to 2018 in the United States [1]. As a result, a key challenge is to find methods to store energy from renewable and intermittent sources so that the stored energy is readily available [2-4]. The storage of renewable energy in the form of energy-rich molecules (hydrogen,

ammonia, and methanol) has been proposed as a solution [2,3,5]. Currently, most hydrogen is produced through steam reforming, a process that depends on fossil fuels and has a large carbon footprint [6,7]. Water electrolysis is an alternative process to produce hydrogen [7]. Electrolyzers are suited to be directly coupled with electric power generated from renewable energy sources, where hydrogen and oxygen are produced from water [2].

Alkaline electrolysis (AEL) is one of the large scale alternatives for the electrochemical production of hydrogen [4]. Currently, one of the main hurdles is the energy consumption, which depends on the cell voltage needed for water splitting [8,9]. Technological efforts have been focused on the development of electrocatalysts to reduce the required cell voltage, thus lowering the cost. Platinum (Pt) is considered one of the best hydrogen evolution reaction (HER) catalysts under acidic conditions, with extremely low overpotentials and large currents [9,10]. However, Pt faces limitations for scale-up applications due to the high cost and scarcity of noble metals. Earth-abundant transition metals are a lower-cost alternative that could enable large-scale production and implementation of alkaline electrolyzers if high activity and durability can be achieved, as compared to Pt as the benchmark comparison for both acidic and alkaline systems.

Nickel (Ni) is a well-known HER catalyst for water electrolysis in alkaline media [9,10]. Efforts have been made to increase the activity and stability of Ni-based catalysts through different approaches, including increased active surface area and the development of Ni-based alloys. HER current density can be increased as the electrochemical surface area (ECSA) is increased for Ni-based electrodeposited catalysts [11]. However, the activity is limited by the intrinsic activity of the catalyst composition [10]. The intrinsic activity is most accurately described by the turnover frequency (TOF). However, due to the difficulty of determining the TOF, in electrocatalysis it has been commonly adopted to use the specific activity to represent the

intrinsic activity. Therefore, the intrinsic activity is most commonly defined as the specific activity where the current is normalized by the real surface area of the electrocatalyst. The incorporation of additional components to form Ni-based alloys such as molybdenum (Mo) [12], cobalt (Co) [13], and iron (Fe) [14] have shown to influence HER activity positively by increasing either the intrinsic catalytic activity or the long term stability. Through the combination of different elements, the intrinsic activity of a catalyst can be improved through a synergistic effect among the components. Alloys can change the electronic structure of the catalyst, and chemical environment changes can positively influence HER activity through effects on charge transport, charge redistribution, and reduction of energy barriers [10,15-17]. However, it has also been shown that incorporation of other components can change the catalyst surface area [12,18,19]. Thus, when different catalysts are compared, it is crucial to delineate the cause for such observed changes in HER performance.

Since both the active surface area and the intrinsic electroactivity can affect measured activity, it is important to experimentally determine the active surface area of the electrocatalyst. Such an evaluation and distinction has demonstrated that Ni-Co and Ni_3S_2@$Co(OH)_2$ compositions result in an increase in intrinsic HER activity through synergistic effects among the components [15,20]. On the other hand, a study of the surface composition, crystallite size, and surface area of a Fe-based catalyst allowed Muller et al. [19] to demonstrate that the incorporation of the metalloids silicon (Si) and boron (B) caused an increase in HER activity due to an increase in surface area, but the integration of Co increased the intrinsic HER activity. With Ni, Fe has been demonstrated to prevent nickel hydride phase formation, which prevents deactivation and improves the stability of Ni catalysts [21]. Therefore, Fe has been frequently implemented in Ni-based catalysts with compositions such as NiFeS/NF [14], Pt-FeNi@C [22], FeNi-P/NF [23], and

NiFe/NC [24] due to the stability it provides. Nonetheless, the benefits of Fe as a transition metal dopant for Ni-based electrocatalysts for HER are not clear because active surface area and intrinsic activity have not been fully and separately evaluated.

Navarro-Flores et al. [25] concluded that the overall electrocatalytic activity of bi-metallic Fe-Ni films for acidic HER was greater than that of pure Ni due to changes in surface roughness but the authors point out that the intrinsic electrocatalytic activity of bi-metallic Ni-Fe was actually lower than that of pure Ni films. However, at the same time, Navarro-Flores et al. [25] suggest that differences between Ni and Ni-Fe activity could be due to an oxide film on the catalyst surface. However, the authors do not provide a chemical analysis of the catalyst surfaces to clearly show these differences. In alkaline media, Solmaz et al. [26] concluded that Fe-Ni alloy films increased HER performance compared to mono-metallic Fe and Ni films. In addition, Solmaz et al. [26] proposed that a film synthesized from a 4:6 molar concentration ratio of Ni^{2+}:Fe^{2+} precursors was the best cathode for HER. Surface area variability between films was observed from atomic force microscopy (AFM) and EIS measurements, but a full evaluation of the intrinsic activity taking in consideration the differences in surface area was not performed; experimentally-determined bi-metallic ratio was not reported. Nonetheless, the study by Solmaz et al. [26] is of importance as it focused on testing the catalysts for extended periods (24 and 120 h) and evaluated the catalysts based on corrosion and long-term stability, further demonstrating that incorporation of Fe increases the stability of Ni-based catalysts during HER.

Using the electrodeposition synthesis method developed by Solmaz et al., [26] McCrory et al. [27] benchmarked Fe, Ni, and FeNi electrocatalyst films in acid and base. When electrocatalyst films were compared at 10 mA cm^{-2} (geometric surface area), NiFe films outperformed both mono-metallic Fe and Ni in alkaline HER activity. McCrory et al. [27] reported that the roughness factor

of the films increased in the order of Ni < Fe < NiFe, suggesting that surface roughness differences were the source of FeNi HER activity enhancement. This result indirectly demonstrates that the intrinsic activity of Ni may in fact be higher than that of Fe and NiFe films. However, the authors did not determine the experimental bi-metallic composition of the films, nor was an analysis of element-specific speciation and surface chemistry performed, leaving questions around the roles of composition and chemical structure. An evaluation of the physical surface area of Fe-Ni films was performed by Hu et al. [18]. A profilometer was used to determine the mean roughness factor and demonstrate that the surface roughness depends on the Fe-Ni film composition. Hu et al. [18] suggested that the HER of Fe-Ni films mainly depended on the true physical surface area. However, the study did not determine the electrochemically active surface area.

In contrast to these studies, a study performed by Suffredini et al. [28] is, to the best of our knowledge, the only study to attribute the increase in HER activity of Ni-Fe alloy films to an intrinsic synergistic effect. A clear explanation as to how such a synergistic effect could happen is not provided, but Suffredini et al. [28] point out that such observation is only possible on rough surfaces as the area enhancement is minimal. Conflicting evidence was recently reported by Zhang et al. [24] on nanoparticles, demonstrating that HER activity decreases with an increase in Fe content, but a $Ni_{0.9}Fe_{0.1}$/NC was ultimately selected in the study as it showed excellent stability for HER and the best performance as a bifunctional OER and HER catalyst. There thus remains a gap in the field in terms of understanding the role of Fe in Ni electrocatalyst activity for the HER, and there is a lack of a complete study focused on elucidating the effect of Fe composition on HER in Fe-Ni films. Studies do consistently show increased Ni durability when

Fe is included in the catalyst composition, motivating further delineation of the role of Fe on activity.

To understand whether an Fe dopant into Ni electrocatalysts does in fact enhance the HER and to understand the chemical nature of the electrocatalyst surface, we thus pursued a study on a suite of electrodeposited Fe_xNi_{100-x} films. We focus herein on understanding whether surface area or intrinsic activity is the main effect responsible for HER activity on different Ni-Fe bi-metallic catalysts in alkaline media. In addition, we probe the surface chemistry of this electrocatalyst suite to understand metallic and oxide contributions to the as-synthesized films. Film morphology was studied by scanning electron microscopy (SEM), and the composition of as-deposited samples was determined by energy dispersive x-ray spectroscopy (EDX), x-ray photoelectron spectroscopy (XPS), and inductive coupled plasma mass spectrometry (ICP-MS). The electronic structure was evaluated through XPS and EIS.

Surface chemistry analysis suggests as-synthesized films are composed of a metallic subsurface with a top oxidic layer. However, when films were tested in alkaline electrolyte, cyclic voltammetry analysis demonstrated that Ni on the surface is fully reduced, but Fe can be found as Fe^{2+} and Fe^0. The ECSA was determined and used to compare the intrinsic electrochemical activity of the different catalysts. We have found that the electrochemically active surface area depends on the composition and in general increases with the incorporation of Fe. The bi-metallic film with the lowest overpotential needed to reach -10 mA cm^{-2} was $Fe_{50}Ni_{50}$ demonstrating to have the highest geometric surface area normalized HER activity, which we attribute to the high ECSA. We thus demonstrate in this study that the HER activities observed for electrodeposited Fe_xNi_{100-x} films are likely due to changes in surface area, which depend on

the composition, rather than by an enhancement of the intrinsic catalytic activity of the components.

2.2 Experimental Section

2.2.1 Materials

The following chemicals were purchased and used without further purification. Iron(II) sulfate heptahydrate ($FeSO_4 \cdot 7H_2O$) (≥99.0% Sigma-Aldrich), nickel(II) sulfate hexahydrate ($NiSO_4 \cdot 6H_2O$) (≥99.99% Sigma-Aldrich), boric acid (H_3BO_3) (≥99.5% Sigma-Aldrich), 70% nitric acid (HNO_3) (≥99.999% Sigma-Aldrich), concentrated sulfuric acid (H_2SO_4) (ACS reagent Sigma-Aldrich), and iron and nickel ICP standards (Aristar, BDH). Ultrapure water (18.2 MΩ·cm) was obtained from a Milli-Q system. Gold coated silicon wafers (100 nm gold, 5 nm titanium) were purchased from Platypus Technologies and Au with Ti adhesion 5 MHz quartz crystals from Biolin Scientific.

2.2.2 Synthesis of Fe_xNi_{100-x} Heterogeneous Catalysts

Different Fe_xNi_{100-x} ratios were directly deposited on conductive substrates using cathodic electrodeposition. The substrate used were silicon wafers coated with 100 nm gold. Wafers were cut into 1 cm x 2 cm rectangles and later covered with Kapton tape in order to limit the area exposed to the electrolyte to about 1 cm^2. A three-electrode electrochemical system was used to hold the potentials at (-1.5V) for 30 seconds, where Ag/AgCl (3M NaCl) was used as the reference electrode, and a graphite rod was used as the counter electrode.

Solution of different ratios (Table S2.1) of Fe_xNi_{100-x} salts were prepared to produce the desired compositions of Fe_xNi_{100-x} catalyst films from a 150 ml plating bath. For each synthesized film, an aqueous solution of 0.1 M total metal content of iron(II) sulfate heptahydrate and nickel(II) sulfate hexahydrate, and 0.1 M of boric acid, was prepared accordingly. The ultrapure water

(18.2 MΩ·cm resistance) used to prepare the deposition bath was deaerated for 30 min with Argon before being used and also while the solution was being mixed to dissolve the salts and prevent Fe oxidation and precipitation. Afterward, the deposited films were rinsed with water (18.2 MΩ·cm resistance) and dried with nitrogen gas to remove any excess deposition bath solution. To prevent contamination between different syntheses, all materials used during the deposition were soaked in 1 M sulfuric acid and rinsed thoroughly with water (18.2 MΩ·cm resistance) to clean surfaces and prior to the next synthesis.

2.2.3 Physical Characterization

Quartz crystal microbalance with dissipation monitoring (QCM-D) from Biolin Scientific was used to determine mass loaded after film synthesis. The change in mass per unit area (Δm) was calculated using the Sauerbrey equation ($\Delta f = -C_f \times \Delta m$), where ($C_f$) is the sensitivity factor of the AT-cut quartz-crystal sensor and (Δf) is the measured frequency change [29].

Scanning electron microscopy (SEM) (Nova Nanolab 200 5 keV) was implemented to study the surface morphology, and electron dispersive X-ray spectroscopy (EDX) was used to find the relative atomic ratio of Fe and Ni in the films. X-ray photoelectron spectroscopy (XPS) was carried out on a VersaProbe 5000 station from Physical Electronics with a monochromated Al Kα X-ray source. All XPS data analysis was performed with the PHI MultiPack software. The survey scans were used to find the Fe_xNi_{100-x} ratio of the electrocatalyst surface. Additionally, C 1s, O 1s, Fe 2p, and Ni 2p detailed regions were scanned to further study the surface chemistry. Inductive coupled plasma mass spectrometry (ICP-MS) was performed using IcapQ ICP-MS (Thermo Scientific) to quantify and confirm the bulk Fe and Ni composition of the electrodeposited catalysts. Films were digested in concentrated nitric acid and later diluted to a

final 2% nitric acid. A matrix of 2% nitric acid was used to dilute the ICP standards and as a blank.

2.2.4 Electrochemical Characterization

All electrochemical experiments were performed with a VSP-300 BioLogic potentiostat using an H-cell separated by a Celgard 3401 (25 µM thickness) membrane with a three-electrode system. A graphite rod was used as the counter electrode, Ag/AgCl (3 M NaCl) as the reference electrode, and different Fe_xNi_{100-x} ratios as working electrodes. For all experiments, the electrolyte was deaerated with argon for 30 min before the tests, and Ar was used to purge the headspace during the electrochemical analysis.

The uncompensated resistance between the reference electrode and the working electrode was corrected by compensating at 85% IR drop, using the BioLogic EC-Lab software. The uncompensated resistance was measured by performing an impedance measurement at high frequencies (100 kHz) with a 20 mV sinusoidal amplitude at open-circuit potential (OCP). All electrochemical experiments were performed in 1 M NaOH at pH 12.00, with pH controlled through the addition of sulfuric acid. CVs were performed for ten cycles in the potential range (0.2 V to -0.5 V vs. RHE) at a 50 mV s^{-1} scan rate to evaluate their catalytic characteristics under alkaline media (Fig. S2.3). Furthermore, linear sweep voltammetry (LSV) was performed at a scan rate of 5 mV s^{-1} in the same potential window used for the CV.

The ECSA was estimated through the cyclic voltammetry method; a method used to benchmark numerous electrocatalysts for HER [27]. Under a non-Faradaic region, a series of CV scans were performed at different scan rates (25, 50, 100, 200 mV s^{-1}). The average difference between the anodic and cathodic charging current densities were plotted as a function of scan rate, Fig. S2.3(a-e). The double-layer capacitance (C_{dl}) was found by obtaining the slope of the

linear fit. The ECSA of each different Fe_xNi_{100-x} catalyst was estimated by dividing the C_{dl} found by the specific capacitance. The specific capacitance used for our calculations was (0.040 mF cm^{-2}), commonly used for metals in 1 M NaOH [27,30].

2.3 Results and Discussion

2.3.1 Composition and Morphology

Prior to electrochemical analysis of the synthesized Fe_xNi_{100-x} films, several complementary characterization techniques were used to confirm both the bulk and the surface composition of the films. In particular, characterization of the films was pursued to determine if the composition of the samples deposited was consistent and reproducible and if the theoretical and experimental compositions were the same. Surface/near-surface elemental quantification of Fe and Ni content was initially determined by EDX and XPS. PHI MultiPack software was used for the quantification analysis of the XPS survey spectra. Fe and Ni relative content were obtained by using the Fe 3s and Ni 3s binding energy regions (Fig. S2.2) of XPS data to avoid any issues in analysis resulting from the overlap of the Fe 2p binding region and the Ni LMM Auger region. The influence of the Ni LMM Auger peaks on the Fe 2p region can be observed in the spectrum for Fe_0Ni_{100} in Fig. 2.1b (purple spectrum), where based on calculations using the Fe 3s peak, no Fe was detected. The results in Fig. 2.1a demonstrate that the surface composition was tuned according to the theoretical ratios of the deposition bath with minimal variation between replicates (n=3). The compositions determined by XPS and EDX are quite similar, and no major deviations or differences are observed across the compositional space explored. Additionally, the bulk composition of the electrodeposited films was determined by ICP-MS. As demonstrated in Fig. 2.1a, the bulk composition of each film matches the surface composition determined through EDX and XPS. The bulk ICP measurements (Fig. 2.1a) further confirm that each film was

deposited according to the theoretical composition. These results demonstrate that the synthesis method allows compositional tunability and reproducibility of electrocatalyst films with the desired composition. Additionally, electrodeposition of the different Fe_xNi_{100-x} films was performed on a gold (Au) sensor with a titanium adhesion layer (Ti) (5 MHz quartz crystal with Au-Ti coating layers) and analyzed with a quartz crystal microbalance with dissipation monitoring (QCM-D). Through the QCM-D analysis of replicated (n=3) depositions (Table S2.2), we demonstrate that our synthesis technique allows for consistent and repeatable mass deposition. Most compositions deposit a film of around 60 μg cm^{-2} except for the $Fe_{80}Ni_{20}$ ratio, which was around half that value, or ~30 μg cm^{-2} (Table S2.2).

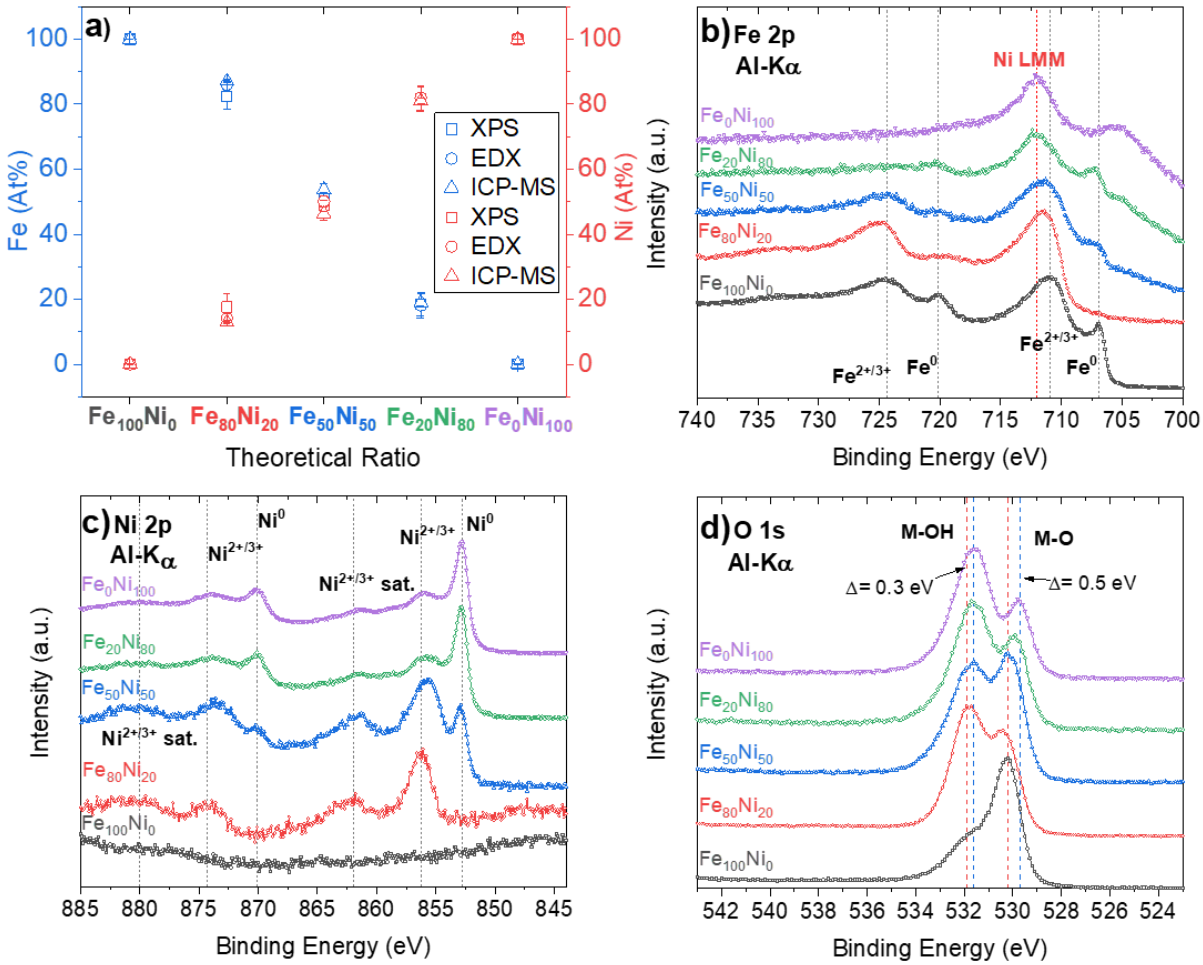

Fig. 2.1. a) Atomic percent of Fe and Ni electrodeposited of as-synthesized films. XPS spectra of b) Fe 2p c) Ni 2p and d) O 1s of the as-synthesized films.

The morphology of the as-deposited samples was also examined. SEM images were obtained of the top surfaces of all the synthesized Fe_xNi_{100-x} films. The images for the different samples (Fig. S2.1) demonstrate that the morphology of the electrodeposited surface varies depending on the Fe_xNi_{100-x} composition. The electrodeposited surfaces of Ni-rich films appear to be more homogeneous and smooth, with less visible clusters, compared to those where Fe is present in higher amounts. The largest clusters with a spherical shape and a diameter of around 2 μm were observed on $Fe_{80}Ni_{20}$. The clusters decrease in size to a sub-micron scale on $Fe_{50}Ni_{50}$ samples and then become un-detectable for $Fe_{20}Ni_{80}$ and Fe_0Ni_{100}. The images obtained suggest there is

likely to be a difference in surface area due to the topological variation among samples of different compositions. However, an ECSA analysis is ultimately necessarily to evaluate the active and electrochemically-accessible surface area of the films.

2.3.2 Analysis of Film Surface Chemistry

The XPS survey spectra (Fig. S2.2) revealed the presence of Fe, Ni, oxygen (O), and carbon (C) on the surface of the as-deposited samples. High-resolution XPS scans were performed on the Fe 2p, Ni 2p, and O 1s binding energy regions (Fig. 2.1b-d) to investigate the chemical state of these elements in the surfaces of the different as-deposited Fe_xNi_{100-x} films. All XPS spectra were calibrated by the C 1s peak (284.8 eV). Fe 2p spectra (Fig. 2.1b) reveal peaks at binding energies of 706.9 eV and 720.2 eV, which can be assigned to the Fe $2p_{3/2}$ and Fe $2p_{1/2}$ of metallic Fe^0 [31-33]. In addition, peaks around 711 eV and 724 eV correspond to the Fe $2p_{3/2}$ and Fe $2p_{1/2}$ of oxidic iron [31-33]. Iron phases with a higher oxidation state (Fe_3O_4, Fe_2O_3, and FeOOH) have similar XPS spectra (shape and peak positioning) [33]. Recognizing the difficulty in distinguishing between Fe speciation, to avoid reporting misleading interpretations, and in agreement to other studies [34,35], we acknowledge the possibility of having Fe^{2+} and Fe^{3+} but due to the strong overlap in peak location, we group them as oxidic iron. Our results agree with those results obtained on deposited Fe films by Louie et al., [35] where peaks at 707 eV and 720 eV were assigned to metallic iron and the main oxidic peak was identified at 710.8 eV. There are no apparent metallic iron features in the spectra of as-deposited $Fe_{80}Ni_{20}$ samples; however, after the sample was argon-ion sputter cleaned, metallic Fe features were revealed (Fig. S2.3), suggesting that the $Fe_{80}Ni_{20}$ film had a thicker surface oxidic layer. Hu et al. [34] compared an Fe foil after it was oxidized and later electrochemically reduced, with XPS results similar to our results. The Fe 2p spectra and peak positions of our as-deposited $Fe_{80}Ni_{20}$ film match that of the fully oxidized iron

foil with a main peak at 711 eV assigned to the oxidic iron species. In addition, the metallic peak around 707 eV was also observed by Hu et al. [34] post reduction of the iron foil. Overall, these results confirmed the presence of oxidic and metallic iron.

The Ni 2p spectra (Fig. 2.1c) reveal that samples electrodeposited contain metallic and oxidic components. The peaks at around 852.8 eV and 870.1 eV correspond to the Ni $2p_{3/2}$ and Ni $2p_{1/2}$ of metallic (Ni^0) nickel, respectively [31,36-38]. Peaks at 856.2 eV and 874.3 eV correspond to Ni $2p_{3/2}$ and Ni $2p_{1/2}$ of the oxidic nickel with their respective satellites at 861.9 eV and 880 eV (broad peaks) [36-38]. The $Fe_{100}Ni_0$ spectrum demonstrates the absence of Ni in samples electrodeposited (Fig. 2.1c). Ratios Fe_0Ni_{100}, $Fe_{20}Ni_{80}$, and $Fe_{50}Ni_{50}$ contain both metallic and oxidic nickel as-deposited. As observed in the Fe 2p spectra, the as-deposited $Fe_{80}Ni_{20}$ sample is the only sample that shows no significant metallic nickel components. The Ni 2p spectra of $Fe_{80}Ni_{20}$ closely resembles that of Ni films deposited and studied by Louie et al. [35] in analyses performed on as-deposited films and post oxidation. We suggest that the oxidic nickel could be $Ni(OH)_2$ and a type of NiOOH, and suspect none or small amounts of NiO due to the absence of the splitting of the Ni $2p_{3/2}$. However, additional work, as done by Biesinger et al., [37,38] would be required to identify the oxidic nickel through the implementation of an analysis of the Ni LMM Auger spectra. After argon ion sputter cleaning, metallic nickel features for all compositions become noticeable (Fig. S2.3). The Ni 2p spectra post argon ion sputtering resemble those of NiFe nanocarbon hydrides that were fully reduced through pyrolysis [24]. These results confirm the oxidation of the surface but demonstrate that a metallic Ni sub-surface was deposited. Overall, these results confirmed the presence of oxidic and metallic nickel.

The O 1s spectra (Fig. 2.1d) for the different Fe_xNi_{100-x} compounds show the presence of two species. The peak at a lower binding energy of 530.2 eV corresponds to metal-oxygen species

(i.e., M-O), while the peak at 531.6 eV is assigned to metal hydroxide species (i.e., M-OH) [32]. The ratio of M-O and M-OH is different depending on the composition, as observed in Fig. 2.1d. Fe_0Ni_{100} has higher M-OH content, and $Fe_{100}Ni_0$ has higher M-O content. As shown by Shi et al., [39] the oxidation kinetics for Fe-Ni alloys depends on the composition. From the O 1s spectra, we can note that M-OH and M-O shift 0.3 eV and 0.5 eV, respectively. O 1s peaks for Fe_0Ni_{100} are found at lower binding energies, and peaks for $Fe_{100}Ni_0$ are found at higher binding energies, correlating to what has been published in literature for different Fe and Ni standards [32]. After argon ion sputtering, a reduction of the M-OH on all samples was observed, suggesting that M-OH is found on the uppermost layer. Such results agree with studies on the oxidation of Fe-Ni alloys, which showed that different layers of oxides can be formed [39]. These results provide insight as to what the surface oxidation most likely resembles after the outer most surface is reduced. In support of the Fe and Ni results, the O 1s spectra demonstrate the presence of multiple oxidic metal components. The inherent oxidation of the samples is expected due to the use of an aqueous bath during synthesis and the consequent exposure of the samples to atmospheric conditions.

As mentioned, different Ni and Fe components are found on the surface of the films. Bi-metallic M-OH and M-O change with composition but are found to contribute to the surface chemistry of both pure metal films. Such differences can be attributed to the mixed surface species formed depending on the presence of Fe or Ni at the surface. The O 1s spectra demonstrate how, based on the composition of the surface, the metal-oxygen speciation is altered. A significant difference in the Fe 2p and Ni 2p peak positions is not apparent throughout our Fe_xNi_{100-x} films, but the change in metallic and oxidic components with composition could suggest bi-metallic interactions. Similar to our study, Hong et al. [40] studied Ni and Co films that were

simultaneously electrochemically deposited. A shift in peak positions of the Ni 2p was minimal; however, Hong et al. [40] also observed a difference in the proportion of the oxidic and metallic species based on the composition. Such differences led Hong et al. [40] to suggest an electronic interaction between the Ni and Co components. Therefore, we attribute the difference in proportions of oxidic and metallic species though out the Fe_xNi_{100-x} films to be due electronic interactions between the Fe and Ni components.

2.3.3 Hydrogen Evolution Reaction Performance

The HER activity for the different as-deposited Fe_xNi_{100-x} ratios and control samples (Au, Pt) were examined under alkaline conditions using an H-cell three-electrode system. All surfaces were initially cycled in the alkaline electrolyte for ten cycles to stabilize the surfaces and obtain consistent cyclic voltammograms (CVs), Fig. S2.4c. The CVs were performed from 0.2 V vs RHE to -0.5 V vs RHE. The initial cycle deviates from the subsequent cycles, which can be attributed to the reduction of the different oxidic species present on the surface, Fig. S2.4a. The stabilized CVs of the Fe containing surfaces closely resemble those previously reported for Fe in alkaline solutions [26,41,42]. Within the potential window of interest, Fe goes through a quasi-reversible reduction oxidation process involving Fe^0 and Fe^{2+}. The cathodic peak of the stabilized CV appears to have two components, Fig. S2.4. It has been demonstrated that the reduction of iron oxides/oxyhydroxides and Fe^{2+} in alkaline solutions on an iron sheet and sputtered film happen at close potentials [41]. Thus, the smaller shoulder of the cathodic peak can be attributed to the reduction of Fe oxides/hydroxides that have not been reduced in previous cycles. On the other hand, nickel is fully reduced after the first cycle, Fig. S2.4b. It has been previously shown that Ni will oxidize at higher potentials in alkaline conditions [26,43-45] not reached in our experiments. Thus, we conclude that nickel in the deposited films under the

conditions of interest are found as Ni^0. As previously mentioned, the main purpose of performing the CVs was to stabilize the surface. Nonetheless, these results help to support the analysis previously reported on the surface chemistry.

The results of Fig. 2.2a show a comparison of the linear sweep voltammograms (LSV), where the IR-corrected voltage in the RHE scale is plotted against the geometric surface area normalized current; the inset of Fig. 2.2a shows a comparison of the measured overpotentials taken at -10 mA cm^{-2}. In order to ensure that the LSV was performed in a kinetically limited region, the LSV was performed at different stir rates, Fig S2.6. The LSV results overlap at different stirring rates showing the lack of mass transport limitations and confirming that the data were obtained in a kinetically limited region. The geometric surface area used for the normalization of the current was 1 cm^2 for the different Fe_xNi_{100-x} synthesized samples and Au and 0.159 cm^2 for the Pt wire. When evaluating the geometric area normalized HER activity (i.e., current density measured at -0.5 V vs. RHE), the synthesized materials followed the order: $Fe_{80}Ni_{20} \approx Fe_0Ni_{100} \approx Fe_{50}Ni_{50} > Fe_{100}Ni_0 > Fe_{20}Ni_{80}$ (Table S2.6). A widely used parameter to compare different catalysts is the determined overpotential needed to reach a current density of -10 mA cm^{-2}. The inset graph in Fig. 2.2a shows that the overpotential needed to reach a current density of -10 mA cm^{-2} does not follow a trend with respect to Fe_xNi_{100-x} composition. However, $Fe_{50}Ni_{50}$ has the lowest overpotential (-390 mV), while $Fe_{100}Ni_0$ has the largest overpotential (-443 mV) needed to drive a current density of -10 mA cm^{-2}.

Solmaz and Kardas studied Fe-Ni electrodeposited films and concluded that bi-metallic films were more active electrocatalytically when compared to mono-metallic films and further identified a specific composition as the optimal cathode for HER [26]. The highest HER electroactivity was obtained on films from a precursor aqueous plating bath with a concentration

ratio of $4Ni^{2+}$:$6Fe^{2+}$, when evaluated in 1M KOH at room temperature [26]. In a later study, Fe-Ni alloy films were evaluated in 25 wt% KOH at 80 °C [46]. Flis-Kabulska and Flis determined that the HER activity increased with increase of Fe content up to 90 wt% Fe, where the highest activity was reached [46]. Such studies agree to an extent with our results as we found that in our case a bi-metallic film of $Fe_{50}Ni_{50}$ composition was found to have the best HER performance (i.e., as measured by both current density and overpotential) when normalized by geometric surface area. However, we observe that bi-metallic surfaces do not outperform monometallic surfaces in all cases.

It is important to highlight that the studies performed by Solmaz and Kardas and by Flis-Kabulska and Flis focused on evaluating different Fe-Ni compositions for their extended HER activity to determine Fe-Ni sample stability. However, these studies lack an evaluation of active surface area. As noted previously in our SEM results, there is a morphological difference that occurs as the composition changes. Such a morphological difference is also evident in the SEM and AFM results presented in the study of the Fe-Ni films by Solmaz and Kardas [26]. However, the authors do not discuss this aspect in detail and the role of the surface morphology is left out of the evaluation of catalyst activity. To address this gap and further our understanding of these details, additional electrochemical analyses were performed to understand the effect of these morphology changes as the Fe-Ni catalyst composition changes and the overall impact on HER activity.

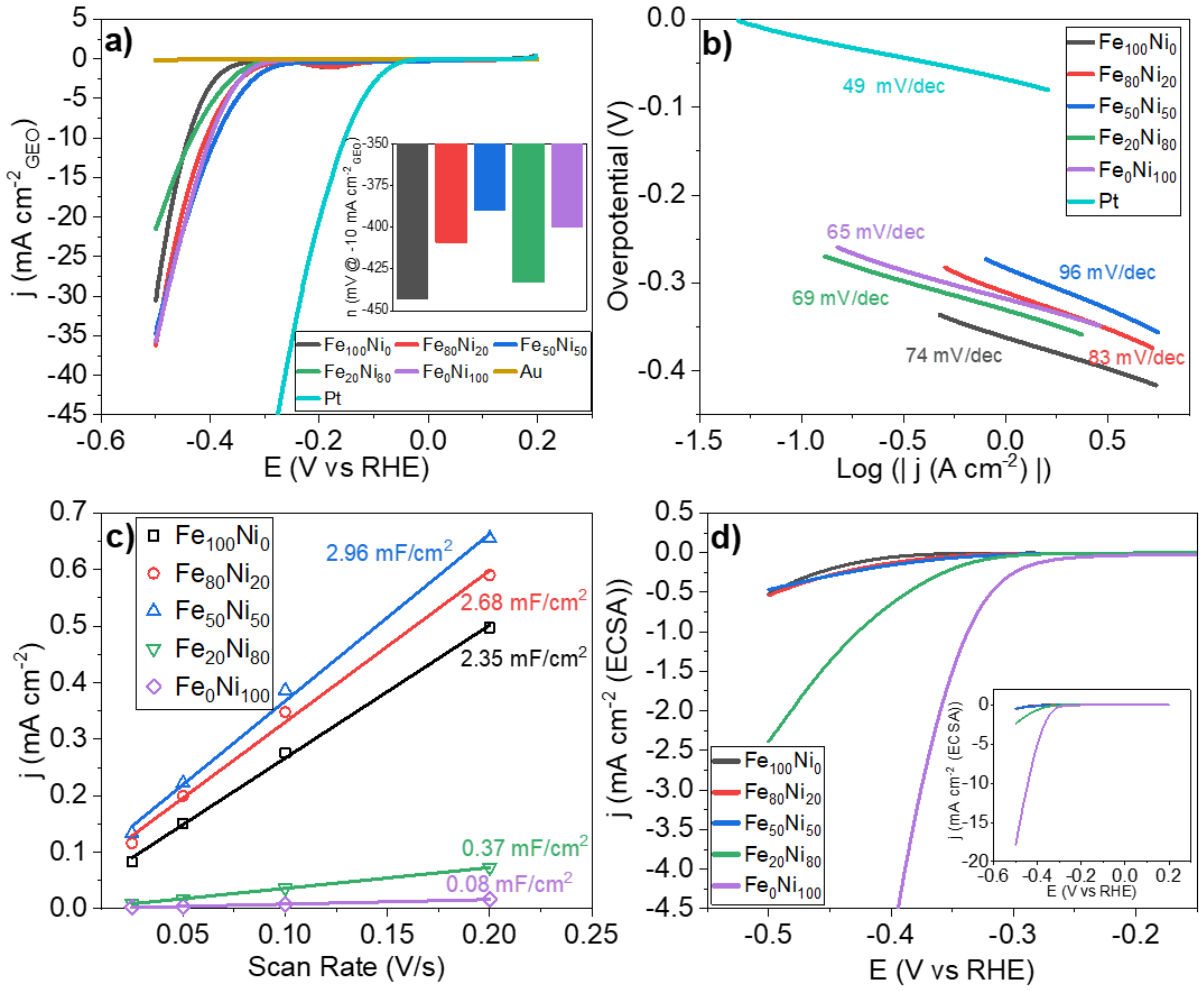

Fig. 2.2. a) LSV of different Fe_xNi_{100-x}, Au, and Pt in 1M NaOH (pH=12) normalized by geometric surface area. b) Tafel plots of Fe_xNi_{100-x} and Pt. c) calculated double-layer capacitance (C_{dl}) used to estimate the electrochemically active surface area of the different Fe_xNi_{100-x} samples. d) LSV of different Fe_xNi_{100-x} normalized the estimated ECSA in 1M NaOH (pH=12).

First, based on the polarization curves from Fig. 2.2a, the Tafel plots of the different catalysts were determined to evaluate the reaction kinetics, Fig. 2.2b. Pt shows the lowest Tafel slope (49 mV dec^{-1}), a value that correlates with those previously reported for Pt/C in 1 M NaOH (40 mV dec^{-1}) [13]. Generally, through our literature search, the HER Tafel slopes of different Fe and Ni based transition metal catalysts in alkaline electrolyte are found in the 60-120 mV dec^{-1} range [13,14,23,24,46,47]. The experimentally-determined Tafel slope values of the different Fe_xNi_{100-x} samples are in the range of 65-96 mV dec^{-1} , in accordance with other results published. The

slopes separate the samples into two groups. The first group includes $Fe_{100}Ni_0$, $Fe_{80}Ni_{20}$, and $Fe_{50}Ni_{50}$ with higher slopes, while the compositions of $Fe_{20}Ni_{80}$ and Fe_0Ni_{100} have lower slopes. Our result reveals favorable HER kinetics for samples with higher Ni content as $Fe_{20}Ni_{80}$ and Fe_0Ni_{100}. The obtained Tafel slopes suggest that overall, the samples follow the Volmer-Heyrovsky mechanism for HER [48,49]. Additionally, the Tafel slope values that we obtain suggest that the electrochemical hydrogen desorption step through the Heyrovsky reaction ($H_2O + e^- + H^* \rightarrow H_2 + HO^-$) [47], is likely the rate-determining step.

To elucidate the effect of composition on HER without any contribution due to differences in surface area, the electrochemically active surface area was determined. The electrochemically active surface area was estimated from the double layer capacitance obtained through the CV method. As shown in Fig. S2.5(a-e), CVs of a 0.1 V window were performed within a non-Faradaic region at different scan rates. The charging current at the different scan rates was plotted (Fig. 2.2c) to obtain the double layer capacitance from the slope. From Fig. 2.2c, we can observe a difference in orders of magnitude in the double layer capacitance (C_{dl}) between the films depending on the composition. Once again, the different Fe_xNi_{100-x} catalysts are separated into two groups, where $Fe_{100}Ni_0$, $Fe_{80}Ni_{20}$, and $Fe_{50}Ni_{50}$ compositions have high C_{dl} values and $Fe_{20}Ni_{80}$ and Fe_0Ni_{100} compositions have low C_{dl} values. The ECSA was estimated using the specific capacitance (0.04 mF cm^{-2}) commonly used for 1 M NaOH [27,30]. Nonetheless, as Wei et al. [50] states, there is a need for additional work in this area to determine the specific capacitance of different materials and the development of a database in order to improve the accuracy of ECSA determination. Results are summarized in Fig. 2.4a. The ECSA values estimated for $Fe_{100}Ni_0$, $Fe_{80}Ni_{20}$, and $Fe_{50}Ni_{50}$ are an order of magnitude higher than that of $Fe_{20}Ni_{80}$ and Fe_0Ni_{100}. In agreement with SEM imaging, the samples with higher Fe have a higher electroactive surface

area and thus more exposed sites. As noted previously, the Tafel slopes and the C_{dl} suggest an effect due to composition. The same compositional effect is not observed on the polarization curves presented in Fig. 2.2a. The C_{dl} results illustrate that the geometric surface area normalization polarization curves can be misleading and, in this case, would most certainly lead to incorrect conclusions about Fe_xNi_{100-x} catalyst activity, as the difference in electrochemically active surface area could be contributing to HER activity.

As the surface topology can influence catalyst performance, the LSV data were normalized by the ECSA to determine the intrinsic HER activity for each catalyst (Fig. 2.2d). Normalization of the current by the ECSA (Fig. 2.2d) caused the order in HER activity to change from what was observed when the current was normalized by the geometric surface area (Fig. 2.2a). When normalized by the ECSA, only the pure nickel sample reached a current density of -10 mA/cm^2 at an overpotential of -444 mV vs. RHE, as seen in the inset of Fig. 2.2d. Therefore, the ECSA normalized specific current density at (-0.5 V vs. RHE) as shown in Fig. 2.2d was used to compare the samples. The HER activity followed the order: $Fe_0Ni_{100} > Fe_{20}Ni_{80} > Fe_{80}Ni_{20} \approx Fe_{100}Ni_0 \approx Fe_{50}Ni_{50}$, Fig. 2.2d. As expected, pure nickel is more active than pure iron. Thus, our results show that the intrinsic HER activity of bi-metallic Fe-Ni is lower than pure Ni and comparable to pure Fe, and an increase in the intrinsic HER activity is only observed when Ni is the predominant component. To the best of our knowledge, the work by Zhang et al. [24] is the only other work published that studied the effect of Fe-Ni catalyst composition in alkaline media in a similar manner. Zhang et al. [24] similarly demonstrated with nanoparticles that Fe doping negatively affected the HER activity of the $Ni_{1-x}Fe_x$/NC (nanocarbon), as the HER activity decreased with an increase in Fe content. Even though the physical morphology of the two catalyst suites is different since the catalysts were nanoparticulate and included nanocarbon, the

findings of Zhang et al. [24] for nanoparticle catalysts agree with our results on films. When the electrochemical activity of Fe_xNi_{100-x} electrocatalysts is normalized to consider differences in the electrochemically active surface area, which previous studies of Fe-Ni films in base have lacked, the intrinsic activity of Ni is higher than that of Fe and bi-metallic Fe_xNi_{100-x} catalysts.

To further study the electrochemical area and the catalyst specific activity of the different Fe_xNi_{100-x}, EIS was performed at -300 mV overpotential. The impedance spectra of all Fe_xNi_{100-x} samples are presented in a Nyquist plot, Fig. 2.3. The Nyquist plot reveals one semi-circle for all samples, indicating that the EIS spectra can be well-described by a one-time constant model such as the Randles circuit. Consequently, the impedance spectra indicate that the HER is primarily controlled by a charge transfer process, as previously reported for coatings and films in acid and alkaline media [25,26]. To further investigate, the EIS data were modeled using the electrical equivalent circuit diagram shown in Fig. 2.3; a tabular listing of results is summarized in Table S2.7. The charge transfer resistance (R_{CT}) can be evaluated visually by comparing the size of the semi-circles; however, modeling the data provides an accurate and quantitative method to compare such a parameter. R_{CT} describes the rate-determining charge transfer step, and therefore, R_{CT} is inversely proportional to the current density [19]. It is widely accepted that lower charge transfer resistance is indicative of more efficient electron transfer, thus leading to a higher HER electrocatalytic activity [13,15,19,23,24,26]. Therefore, many studies compare the R_{CT} to compare the activity of different catalysts. When comparing our results based on the R_{CT}, we observe that the Fe_0Ni_{100} film has the lowest charge transfer resistance, thus suggesting the highest electrocatalytic HER activity. Overall, the R_{CT} decreases as the Fe content decreases for the Fe_xNi_{100-x} films, except for $Fe_{20}Ni_{80}$. Additionally, the C_{dl} was obtained from the fit of the Nyquist plots and used to determine the ECSA-EIS. The ECSA calculated through EIS

demonstrates that the electrochemically active surface area changes as the composition of the deposited sample varies, Fig. 2.4a. In general, the ECSA determined through EIS was lower than that estimated through the CV method. Such small variation can be attributed to the reduction of surface area from gas bubbles forming on the surface due to the potential at which the EIS measurements were performed [19]; an additional factor that may affect EIS vs CV results is the assumed specific capacitance used in ECSA calculations. These results collectively support our conclusion that the HER activity differences between samples are due to differences in electrochemically active surface area.

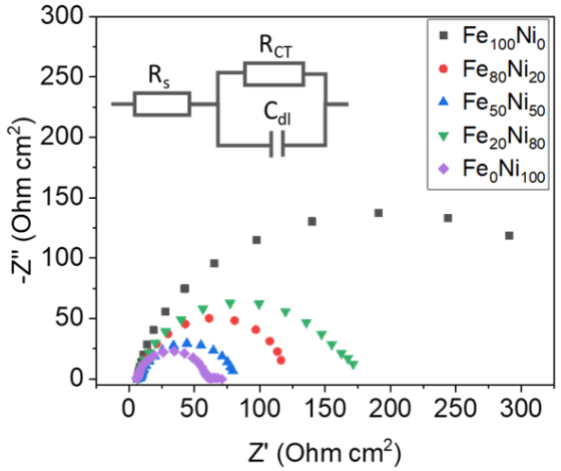

Fig. 2.3. Nyquist plot of EIS obtained at -300 mV in alkaline electrolyte.

The impedance results were further implemented to evaluate the catalytic activity in relation to the composition and active surface area of the different Fe_xNi_{100-x} films. The approach taken here quantitatively distinguishes the effect of composition from the effect of electrochemically active surface area on the HER activity. The intrinsic activity of each sample can be determined from the EIS data by τ, a parameter defined as $\tau = R_{CT} \times C_{dl}$, representing the area-independent activity. Such a parameter has been implemented by Muller et al. [19] and allowed the authors to elucidate that the HER enhancement of Fe-based alloys when doped with metalloids (B and Si)

is due to an increase in surface area whereas doping with Co results in an intrinsic effect. The τ parameter has also been used to study other transition metals such as Co and Co-vanadium (V) on Ni-based alloys [51] and molybdenum (Mo) on Ni-based alloys [52]. The parameter τ is inversely proportional to the specific activity since the charge transfer resistance (R_{CT}) is inversely proportional and the double-layer capacitance (C_{dl}) is directly proportional to the activity and active surface area, respectively [19]. All results are summarized in Table S2.7 and graphically illustrated in Fig. 2.4b. Since τ is inversely proportional to the specific activity, 1/τ was plotted to compare the intrinsic activity of each composition obtained through the EIS and ECSA normalized current density. The comparison of ECSA-normalized current and 1/τ in Fig. 2.4b demonstrates that the specific activity of the samples increases as Ni content increases, thus supporting the results obtained from the current density normalized by ECSA rather than the current density normalized by geometric surface area.

The results presented throughout this study collectively indicate that the intrinsic catalytic activity in alkaline media of mono-metallic Ni films is greater than that of mono-metallic Fe or bi-metallic Fe_xNi_{100-x} films. In addition, when Fe is added to Ni films, the main factor influencing the HER activity is the increase of surface area. The major benefit of Fe doping in Ni-based catalysts remains the increase the long term stability [19,21,24,46], and as shown herein, a possible method of enhancing the HER activity is through the increase of active surface area.

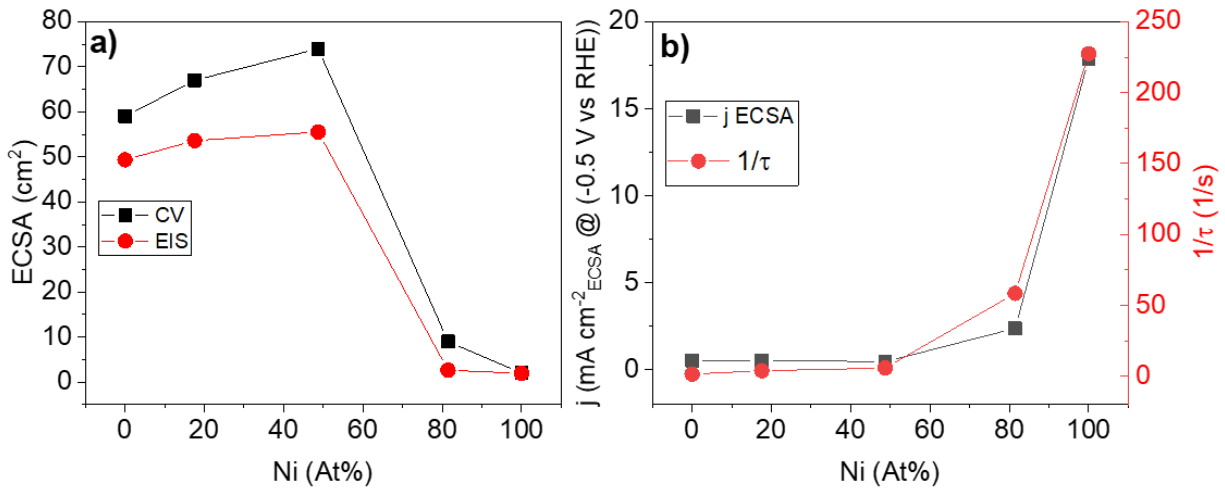

Fig. 2.4. a) Electrochemically active surface area for different Fe_xNi_{100-x} ratios obtained through the CV method and the EIS method. b) Specific current density and the specific activity $1/\tau$ parameter plotted for different compositions of Fe_xNi_{100-x} films, as determined through XPS.

2.4 Conclusions

In summary, Fe_xNi_{100-x} films have been synthesized through an electrodeposition method. The synthesis method was proven to provide composition tunability and reproducible synthesized films. The surface oxide and hydroxide species formed on the as-deposited surface are altered due to the composition. The HER electrochemical activity was studied based on the composition and electrochemically active surface area of the synthesized films. A bimetallic $Fe_{50}Ni_{50}$ film was found to be the most active as it required the lowest overpotential of -390 mV to reach a current density of -10 mA cm^{-2} when normalized by geometric surface area. The ECSA was determined by the CV method and the EIS method, demonstrating that the ECSA was dependent on the sample composition and that in some cases, the difference in active surface area between films was above an order of magnitude. Intrinsic catalytic activity was obtained by normalizing each sample by the electrochemically active surface area and confirmed by obtaining an area-independent parameter, τ, through EIS. Such results demonstrated that mono-metallic Ni films have a greater intrinsic activity than that of mono-metallic Fe and even bi-metallic Fe_xNi_{100-x}

films. We have found that the HER activity of Fe-Ni films is greatly influenced by the changes in active surface area, which are dependent on the composition. Thus, we conclude that the HER activity of different Fe_xNi_{100-x} films in alkaline electrolyte can be attributed to the number of active sites rather than a synergistic effect of the components on intrinsic activity.

References

1 Marcy, C. *U.S. renewable electricity generation has doubled since 2008*, <https://www.eia.gov/todayinenergy/detail.php?id=38752> (2019).

2 Lewis, N. S. & Nocera, D. G. Powering the planet: Chemical challenges in solar energy utilization. *Proceedings of the National Academy of Sciences* **103**, 15729-15735 (2006).

3 Gray, H. B. Powering the planet with solar fuel. *Nature chemistry* **1**, 7-7 (2009).

4 Buttler, A. & Spliethoff, H. Current status of water electrolysis for energy storage, grid balancing and sector coupling via power-to-gas and power-to-liquids: A review. *Renewable and Sustainable Energy Reviews* **82**, 2440-2454 (2018).

5 Wang, G., Mitsos, A. & Marquardt, W. Conceptual design of ammonia-based energy storage system: System design and time-invariant performance. *AIChE Journal* **63**, 1620-1637 (2017).

6 Crabtree, G. W., Dresselhaus, M. S. & Buchanan, M. V. The hydrogen economy. *Physics today* **57**, 39-44 (2004).

7 Holladay, J. D., Hu, J., King, D. L. & Wang, Y. An overview of hydrogen production technologies. *Catalysis today* **139**, 244-260 (2009).

8 Li, X., Hao, X., Abudula, A. & Guan, G. Nanostructured catalysts for electrochemical water splitting: current state and prospects. *Journal of Materials Chemistry A* **4**, 11973-12000 (2016).

9 Zeng, K. & Zhang, D. Recent progress in alkaline water electrolysis for hydrogen production and applications. *Progress in Energy and Combustion Science* **36**, 307-326, doi:http://dx.doi.org/10.1016/j.pecs.2009.11.002 (2010).

10 Gong, M., Wang, D.-Y., Chen, C.-C., Hwang, B.-J. & Dai, H. A mini review on nickel-based electrocatalysts for alkaline hydrogen evolution reaction. *Nano Research* **9**, 28-46 (2016).

11 Ahn, S. H. *et al.* Electrodeposited Ni dendrites with high activity and durability for hydrogen evolution reaction in alkaline water electrolysis. *Journal of Materials Chemistry* **22**, 15153-15159 (2012).

12 Csernica, P. M. *et al.* Electrochemical hydrogen evolution at ordered Mo7Ni7. *ACS Catalysis* **7**, 3375-3383 (2017).

13 Yin, X. *et al.* 3D hierarchical network NiCo2S4 nanoflakes grown on Ni foam as efficient bifunctional electrocatalysts for both hydrogen and oxygen evolution reaction in alkaline solution. *International Journal of Hydrogen Energy* **42**, 25267-25276 (2017).

14 Ganesan, P., Sivanantham, A. & Shanmugam, S. Inexpensive electrochemical synthesis of nickel iron sulphides on nickel foam: super active and ultra-durable electrocatalysts for alkaline electrolyte membrane water electrolysis. *Journal of Materials Chemistry A* **4**, 16394-16402 (2016).

15 Wang, S., Xu, L. & Lu, W. Synergistic effect: hierarchical Ni3S2@ Co (OH) 2 heterostructure as efficient bifunctional electrocatalyst for overall water splitting. *Applied Surface Science* **457**, 156-163 (2018).

16 Yang, Y. *et al.* MoS2–Ni3S2 heteronanorods as efficient and stable bifunctional electrocatalysts for overall water splitting. *Acs Catalysis* **7**, 2357-2366 (2017).

17 Xing, Z., Yang, X., Asiri, A. M. & Sun, X. Three-dimensional structures of MoS2@ Ni core/shell nanosheets array toward synergetic electrocatalytic water splitting. *ACS applied materials & interfaces* **8**, 14521-14526 (2016).

18 Hu, C.-C. & Wu, Y.-R. Bipolar performance of the electroplated iron–nickel deposits for water electrolysis. *Materials chemistry and physics* **82**, 588-596 (2003).

19 Müller, C. I. *et al.* The activity of nanocrystalline Fe-based alloys as electrode materials for the hydrogen evolution reaction. *Journal of Power Sources* **304**, 196-206 (2016).

20 Herraiz-Cardona, I., Ortega, E., Antón, J. G. & Pérez-Herranz, V. Assessment of the roughness factor effect and the intrinsic catalytic activity for hydrogen evolution reaction on Ni-based electrodeposits. *International journal of hydrogen energy* **36**, 9428-9438 (2011).

21 Mauer, A. E., Kirk, D. W. & Thorpe, S. J. The role of iron in the prevention of nickel electrode deactivation in alkaline electrolysis. *Electrochimica acta* **52**, 3505-3509 (2007).

22 Fan, A. *et al.* Engineering FeNi alloy nanoparticles via synergistic ultralow Pt doping and nanocarbon capsulation for efficient hydrogen evolution. *Journal of Materials Chemistry A* **7**, 24347-24355 (2019).

23 Yan, Q. *et al.* Self-supported FeNi-P nanosheets with thin amorphous layers for efficient electrocatalytic water splitting. *ACS Sustainable Chemistry & Engineering* **6**, 9640-9648 (2018).

24 Zhang, X. *et al.* Facile synthesis of nickel–iron/nanocarbon hybrids as advanced electrocatalysts for efficient water splitting. *ACS Catalysis* **6**, 580-588 (2016).

25 Navarro-Flores, E., Chong, Z. & Omanovic, S. Characterization of Ni, NiMo, NiW and NiFe electroactive coatings as electrocatalysts for hydrogen evolution in an acidic medium. *Journal of Molecular Catalysis A: Chemical* **226**, 179-197 (2005).

26 Solmaz, R. & Kardaş, G. Electrochemical deposition and characterization of NiFe coatings as electrocatalytic materials for alkaline water electrolysis. *Electrochimica Acta* **54**, 3726-3734 (2009).

27 McCrory, C. C. L. *et al.* Benchmarking hydrogen evolving reaction and oxygen evolving reaction electrocatalysts for solar water splitting devices. *J. Am. Chem. Soc.* **137**, 4347-4357, doi:10.1021/ja510442p (2015).

28 Suffredini, H. B., Cerne, J. L., Crnkovic, F. C., Machado, S. A. S. & Avaca, L. A. Recent developments in electrode materials for water electrolysis. *International Journal of Hydrogen Energy* **25**, 415-423 (2000).

29 Sauerbrey, G. Verwendung von schwingquarzen zur wägung dünner schichten und zur mikrowägung. *Zeitschrift für Physik* **155**, 206-222 (1959).

30 McCrory, C. C., Jung, S., Peters, J. C. & Jaramillo, T. F. Benchmarking heterogeneous electrocatalysts for the oxygen evolution reaction. *Journal of the American Chemical Society* **135**, 16977-16987 (2013).

31 Moulder, J. F., Strickle, W. F., Sobol, P. E. & Bomben, K. D. Handbook of X-ray photoelectron spectroscopy. *Perkin-Elmer Corporation* **40**, 221 (1992).

32 Biesinger, M. C. *et al.* Resolving surface chemical states in XPS analysis of first row transition metals, oxides and hydroxides: Cr, Mn, Fe, Co and Ni. *Applied Surface Science* **257**, 2717-2730, doi:https://doi.org/10.1016/j.apsusc.2010.10.051 (2011).

33 Temesghen, W. & Sherwood, P. Analytical utility of valence band X-ray photoelectron spectroscopy of iron and its oxides, with spectral interpretation by cluster and band structure calculations. *Analytical and bioanalytical chemistry* **373**, 601-608 (2002).

34 Hu, L. *et al.* Ambient Electrochemical Ammonia Synthesis with High Selectivity on Fe/Fe Oxide Catalyst. *ACS Catalysis* **8**, 9312-9319, doi:10.1021/acscatal.8b02585 (2018).

35 Louie, M. W. & Bell, A. T. An investigation of thin-film Ni-Fe oxide catalysts for the electrochemical evolution of oxygen. *J. Am. Chem. Soc.* **135**, 12329-12337 (2013).

36 Grosvenor, A. P., Biesinger, M. C., Smart, R. S. & McIntyre, N. S. New interpretations of XPS spectra of nickel metal and oxides. *Surface Science* **600**, 1771-1779, doi:10.1016/j.susc.2006.01.041 (2006).

37 Biesinger, M. C., Lau, L. W. M., Gerson, A. R. & Smart, R. S. C. The role of the Auger parameter in XPS studies of nickel metal, halides and oxides. *Physical Chemistry Chemical Physics* **14**, 2434-2442 (2012).

38 Biesinger, M. C., Payne, B. P., Lau, L. W., Gerson, A. & Smart, R. S. C. X-ray photoelectron spectroscopic chemical state quantification of mixed nickel metal, oxide and hydroxide systems. *Surface and Interface Analysis* **41**, 324-332 (2009).

39 Shi, Z. *et al.* Oxidation of Fe-Ni alloys in air at 700 C, 800 C and 950 C. *High Temperature Materials and Processes* **31**, 89-96 (2012).

40 Hong, S. H. *et al.* Fabrication and evaluation of nickel cobalt alloy electrocatalysts for alkaline water splitting. *Applied surface science* **307**, 146-152 (2014).

41 Duschek, K., Uhlemann, M., Schlörb, H., Nielsch, K. & Leistner, K. Electrochemical and in situ magnetic study of iron/iron oxide films oxidized and reduced in KOH solution for magneto-ionic switching. *Electrochemistry Communications* **72**, 153-156 (2016).

42 Guzman, R. S. S., Vilche, J. R. & Arvia, A. J. The potentiodynamic behaviour of iron in alkaline solutions. *Electrochimica Acta* **24**, 395-403 (1979).

43 Alsabet, M., Grdeń, M. & Jerkiewicz, G. Electrochemical growth of surface oxides on nickel. Part 3: Formation of β-NiOOH in relation to the polarization potential, polarization time, and temperature. *Electrocatalysis* **6**, 60-71 (2015).

44 Li, C. *et al.* Acid promoted Ni/NiO monolithic electrode for overall water splitting in alkaline medium. *Science China Materials* **60**, 918-928 (2017).

45 Hall, D. S., Bock, C. & MacDougall, B. R. An oxalate method for measuring the surface area of nickel electrodes. *Journal of The Electrochemical Society* **161**, H787-H795 (2014).

46 Flis-Kabulska, I. & Flis, J. Electroactivity of Ni–Fe cathodes in alkaline water electrolysis and effect of corrosion. *Corrosion Science* **112**, 255-263 (2016).

47 Ma, L. *et al.* Self-assembled ultrathin NiCo2S4 nanoflakes grown on Ni foam as high-performance flexible electrodes for hydrogen evolution reaction in alkaline solution. *Nano Energy* **24**, 139-147 (2016).

48 Wang, X., Xu, C., Jaroniec, M., Zheng, Y. & Qiao, S.-Z. Anomalous hydrogen evolution behavior in high-pH environment induced by locally generated hydronium ions. *Nature communications* **10**, 1-8 (2019).

49 Shinagawa, T., Garcia-Esparza, A. T. & Takanabe, K. Insight on Tafel slopes from a microkinetic analysis of aqueous electrocatalysis for energy conversion. *Scientific Reports* **5**, 13801, doi:10.1038/srep13801 (2015).

50 Wei, C. *et al.* Approaches for measuring the surface areas of metal oxide electrocatalysts for determining their intrinsic electrocatalytic activity. *Chemical Society Reviews* **48**, 2518-2534 (2019).

51 Kaninski, M. P. M., Nikolic, V. M., Tasic, G. S. & Rakocevic, Z. L. Electrocatalytic activation of Ni electrode for hydrogen production by electrodeposition of Co and V species. *International Journal of Hydrogen Energy* **34**, 703-709 (2009).

52 Birry, L. & Lasia, A. Studies of the Hydrogen evolution reaction on raney nickel—molybdenum electrodes. *Journal of applied electrochemistry* **34**, 735-749 (2004).

3. Chapter 3. Electrochemical activation of silicon: Enhancing hydrogen production from FeNi electrocatalysts

Authors: Sergio I. Perez Bakovic, Prashant Acharya, and Lauren F. Greenlee

Abstract

A two-sided electrode composed of $Fe_xNi_{100-x}O_y$ and Si was implemented to produce hydrogen. The hydrogen evolution reaction is facilitated by the $Fe_xNi_{100-x}O_y$ electrocatalyst. The high pH of the alkaline electrolyte and the reducing potential of the electrode result in the activation of the Si side, allowing spontaneous production of H_2. Results demonstrate that the $Fe_xNi_{100-x}O_y$ composition and the electrolyte composition influence the performance of the $Fe_xNi_{100-x}O_y$/Si system. The activation and subsequent production of H_2 by the Si was demonstrated to be favored in 0.1 M KOH and NaOH electrolytes over LiOH, both with applied voltage and at open circuit voltage. At the same time, it was shown that the $Fe_{80}Ni_{20}$/Si composition maintained a current of -10 mA at a lower potential (~50 mV), compared to the $Fe_{20}Ni_{80}$/Si composition. Herein, we demonstrate that the two-sided $Fe_xNi_{100-x}O_y$/Si electrode can be used to boost the production of hydrogen leading to a maximum of 140% H_2 faradaic efficiency.

Keywords: silicon, iron, nickel, hydrogen evolution reaction, alkaline electrolyte.

3.1 Introduction

Hydrogen can be produced through the assisted photo-electrochemical (PEC) or electrochemical (EC) water-splitting process.[1-3] Hydrogen production through electrochemical water splitting is powered by electrical energy input. The minimum theoretical voltage required to drive water electrolysis is 1.23 V at room temperature.[2] Electrocatalysts are implemented to reduce the overpotential, which is the additional voltage that must be applied above the theoretical minimum to obtain a current density,[2] thus achieving higher reaction rates with lower energy

requirements. Pt is the most active catalyst for the hydrogen evolution reaction (HER), the cathodic half-reaction of water electrolysis.[2] Over the years, extensive work has been performed to find an alternative catalyst to lower the production cost of electrolyzers, and Earth-abundant first row transition metal-based catalysts such as Ni, Fe, and Co are among those that have been shown to be effective HER catalysts in alkaline electrolyte.[2]

An alternative method to produce hydrogen is through PEC water splitting. PEC systems are powered by light energy.[2] Silicon (Si), is the most widely used photon absorber for PEC due to the abundance of Si and mature technological infrastructure, but also due to its stability in low pH conditions.[3] Si is a versatile semiconductor and can be used as a photoanode (n-type) or a photocathode (p-type) based on the dopant.[3] Si is an attractive material to develop PEC water splitting devices using a metal-insulator-semiconductor (MIS) photoelectrode architecture.[4] However, Si-based photo-electrodes are unstable in alkaline solution.[2,4,5] Therefore, a challenge that silicon-based PEC electrodes must overcome is the corrosion of the oxide layer under electrochemical conditions (pH and potentials).[4,6] This corrosion behavior, however, can be used advantageously in an alternative approach to hydrogen production through the self-oxidation of the electrode material. The on-demand production of hydrogen without light, heat, or electricity has been demonstrated through the spontaneous reaction of silicon with water.[7,8] Silicon oxidizes through the reaction with water, producing hydrogen (H_2), Eq 1.

$$Si + 2H_2O \rightarrow SiO_2 + 2H_2 \qquad \Delta G_{rxn,Standard\ State} = -376.37\ kJ\ mol^{-} \qquad (1)$$

$$SiO_2\ (s) + 2H_2O\ (l) \leftrightarrow Si(OH)_4 \qquad \Delta G_{rxn,Standard\ State} = -7.93\ kJ\ mol^{-} \qquad (2)$$

H_2 production through spontaneous Si oxidation suffers from a slow production rate. This challenge has been overcome by engineering nano-Si materials. Erogbogdo et al.[8] demonstrated

that Si nanoparticles dispersed in aqueous alkaline (KOH) solution resulted in 1000x faster hydrogen production rates compared to bulk Si. Recently, Ning et al.[7] fabricated silicon nanowires through metal-assisted anodic etching on a Si wafer support (p-type, boron-doped), allowing the large specific surface area to allow the increased production of H_2 in deionized water.

As shown in Eq. 2, some of the SiO_2 will dissolve as $Si(OH)_4$, but the SiO_2 that remains on the surface will inhibit the contact of water to the Si and stop the reaction over time.[7] A resulting native oxide layer forms that prevents activation; however, this native oxide can be disrupted through corrosive reactions with hydroxyl ions (OH^-). The alkaline corrosion of passivated Si wafers has been demonstrated to undergo two reactions.[9] The initial step is oxide etching, whereby the native silicon dioxide layer is removed through dissolution of silicon dioxide in sodium hydroxide, Eq. 3. It has been demonstrated that the time for oxide etching increases as the concentration of NaOH decreases.[9] Once the native oxide is removed, the second step is Si etching, where the production of H_2 occurs as Si reacts with NaOH and H_2O, following Eq. 4.[9] The etching rate of Si was observed to increase as the NaOH concentration decreased, reaching a maximum at 3% NaOH. Huang and Tao attribute the etching rate dependence on the balance between NaOH and H_2O as both are reactants during the Si etching step.[9]

$$SiO_2 + 2\,OH^- \leftrightarrow SiO_3^{2-} + H_2O \qquad (3)$$

$$Si + 2\,OH^- + H_2O \leftrightarrow SiO_3^{2-} + 2H_2 \qquad (4)$$

The etching of silicon has been demonstrated to be dependent on dopants,[10] the silicon orientation,[11] etchants,[9,12,13] and additives.[12,14] The vast majority of this earlier literature has focused on silicon etching for the application of micro-fabrication. Therefore, most studies have

evaluated the corrosion of silicon through topological studies or weight loss measurements. More recently, the application of using silicon to produce hydrogen was demonstrated in 2 wt% NaOH,[15] and 1:8 molar ratio of Si/KOH.[8] As the application shifts to implement the self-oxidizing reaction of silicon for hydrogen production, the measurement of hydrogen is essential. Further, since different etchants, such as sodium hydroxide (NaOH) and potassium hydroxide (KOH), have been implemented to disrupt the native silicon oxide layer and enable subsequent hydrogen production, the role of the alkali cation is important to understand. Seidel et al.[11] studied the corrosion of silicon in alkaline solutions (LiOH, NaOH, and KOH) and suggested that the role of the cations was negligible. However, more recently, Lai et al.[12] studied the corrosion of porous silicon and demonstrated that the corrosion time in KOH was shorter than that in NaOH. However, neither of these two studies evaluated hydrogen production during the corrosion experiments. To the best of our knowledge, a study that evaluates both the role of the electrolyte composition and the measurement of hydrogen production during the activation of Si has not been performed.

Even though this approach to H_2 production from Si ultimately consumes the Si electrode, the reaction system may also enhance H_2 production efficiency without additional energy input, particularly when coupled with other low-cost electrocatalyst materials, where the benefits of H_2 production may outweigh the cost of Si replacement. Fe- and Ni-based oxides are among the most studied electrochemical catalysts due to their high electrocatalytic activity and lower cost, compared to highly active noble metals.[16,17] Herein, we developed an electrocatalyst composed of abundant materials Si, Fe, Ni to produce hydrogen. A simple two-sided electrode was used, where one side was composed of a $Fe_xNi_{100-x}O_y$ film and another side was composed of Si. The $Fe_xNi_{100-x}O_y$ was implemented as the electrocatalyst, while the Si was used as a substrate and as

a method to enhance hydrogen production. The activation of the silicon towards the production of hydrogen was evaluated in LiOH, NaOH, and KOH electrolytes. The chemical activation and electrochemical activation of silicon were demonstrated to occur only in NaOH and KOH. This is, to the best of our knowledge, the first demonstration of a system that joins an electrocatalyst and a self-oxidizer to improve hydrogen production.

3.2 Experimental Section

3.2.1 Materials

Gold-coated p-type silicon wafers with a titanium adhesion layer (100 nm Au, 5 nm Ti) were purchased from Platypus Technologies. High purity lithium hydroxide monohydrate (99.95%, $LiOH \cdot H_2O$), sodium hydroxide (99.99%, NaOH), and potassium hydroxide (99.99%, KOH) were purchased from Sigma-Aldrich. Ultrapure water (18.2 $M\Omega \cdot H_2O$) from a Milli-Q system was used.

3.2.2 Electrochemical Evaluation

All electrochemical experiments were performed in a custom gas-tight H-cell made by Adams and Chittenden Scientific Glass Coop. To ensure all ports and connections were gas-tight, Dow Corning high vacuum grease was used. A three-electrode cell configuration was used (Fig S3.1). The counter electrode (CE) was a graphite rod, Ag/AgCl (3 M NaCl) was the reference electrode, and for the working electrode (WE), the electrode was interchanged. The H-cell was separated using a Celgard 3401 (25 μM thickness) membrane. The $Fe_xNi_{100-x}O_y$ films were electrochemically deposited onto Au/Si wafers following the procedure outlined in our previous work.[18] The electrodes were electrodeposited at -1.5 V vs. Ag/AgCl in a plating bath composed of boric acid with different ratios of iron and nickel sulfate salts for a total of 30 s. The electrodes used in all electrochemical experiments had 1 cm^2 exposed on each side to the electrolyte. The

linear sweep voltammetry (LVS) was performed in the potential window of 0.2 V to -0.6 V vs. RHE at 10 mV s^{-1} scan rate. Furthermore, chronopotentiometry (CP) experiments were performed by applying a cathodic current of -10 mA. The CP were performed in 10 min intervals with a total of 1 h.Open circuit potential (OCP) experiments were performed in the same gas tight H-cell allowing to monitor the voltage without the energy input. The OCP experiment was performed for a total of 5 h. The electrolyte solution was mixed every 10 min for the initial 1 h and every 20 min past the 1 h prior to taking samples from the headspace. The concentration of the LiOH, NaOH, and KOH were 0.1M for all the experiments performed.

3.2.3 Hydrogen Quantification

All H_2 gas quantification experiments were performed using an H-cell connected to a 490 Micro GC system (Agilent Technologies, Inc., United States) equipped with a thermal conductivity detector (TCD). The pump injection mode was used to collect samples every 10 min from the headspace of the cathode. Ar was used as the carrier gas, the injector temperature and column temperature were set to 75 °C, and the injection time was set to 100 ms. The electrode was vigorously mixed at 1500 rpm prior to each measurement to ensure all gas bubbles are forced to the head space.

3.2.4 Characterization

X-ray photoelectron spectroscopy (XPS) was performed in a VersaProbe 5000 station from Physical Electronics equipped with a monochromated Al Kα X-ray source. All XPS spectra were calibrated by the C 1s peak (284.4 eV). Survey scans were performed from 0 eV to 1400 eV with step of 0.5 eV to identify the surface composition. Detailed scans were further taken at 0.1 eV step size for the Si 2p region from 94 eV to 114 eV.

3.3 Results and Discussion

3.3.1 Electrochemical Characterization

An initial evaluation of the HER electrochemical activity of the $Fe_xNi_{100-x}O_y$/Si was performed. Bimetallic films with a composition of $Fe_{20}Ni_{80}$/Si and $Fe_{80}Ni_{20}$/Si were evaluated by linear sweep voltammetry (LSV) in LiOH, NaOH, and KOH alkaline solutions, all with a concentration of 0.1 M. Additionally, Au/Si wafers were also evaluated as a control. The LSV results are shown in Fig. 3.1. The LSVs were collected from 0.2 V to -0.6 V vs. RHE. The geometric area in contact with the electrolyte was 1 cm^2 and was used as the geometric surface area to normalize the current measured during the LSVs. The LSV results demonstrate that the $Fe_{80}Ni_{20}$/Si film is more active, resulting in a larger produced current density. The potential required to reach a current density of -10 mA cm^{-2} is 30 mV lower when $Fe_{80}Ni_{20}$/Si was the electrode, compared to $Fe_{20}Ni_{80}$/Si. These results were expected as our previous study demonstrated that when $Fe_xNi_{100-x}O_y$ films are normalized by the geometric surface area, the HER activity of $Fe_{80}Ni_{20}$ is higher than that of $Fe_{20}Ni_{80}$ in a NaOH alkaline solution. Interestingly, when evaluating the influence of the electrolyte solution (i.e., LiOH, NaOH, and KOH), the LSV results show no significant difference in HER current density. The peaks observed for the $Fe_{80}Ni_{20}$ composition in Fig. 3.1b result from iron reduction and result in slight variations in peak current as a function of electrolyte composition.

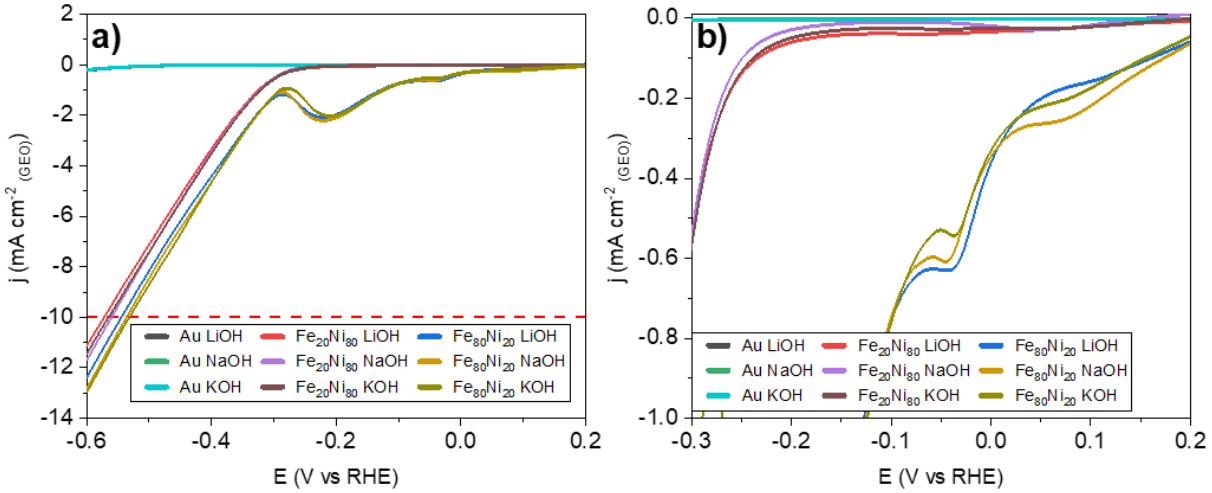

Fig. 3.1. Linear sweep voltammograms (LSVs) of the three electrodes evaluated (i.e., Au/Si, $Fe_{20}Ni_{80}$/Si, and $Fe_{80}Ni_{20}$/Si) in three different electrolyte solutions (i.e., LiOH, NaOH, and KOH) of 0.1 M concentration for (a) the underpotential and Faradaic HER voltage regions and (b) the underpotential HER voltage region.

The activation and self-oxidizing reaction at the Si side was then evaluated. The Au/Si substrates used to produce the $Fe_xNi_{100-x}O_y$/Si electrodes were immersed in the different electrolytes (i.e., LiOH, NaOH, KOH) in an H-cell, and H_2 gas production was recorded for five hours. Simultaneously, the open circuit potential (OCP) was monitored to study the free corrosion potential and evaluate the surface oxide stability as a function of electrolyte composition. The OCP experiments also allow monitoring of the timescale for corrosion initiation and thus activation of Si.

The stability and corrosion of silicon have been previously studied by monitoring the free corrosion potential, which provides a diagnostic for the stability of the surface oxides and allows corrosion monitoring over time. Electrochemical methods such as OCP monitoring are alternative methods to the most common weight loss measurements used in silicon corrosion studies. Large potential variations indicate the instability of surface oxide, demonstrating the active corrosion which drives the OCP to low values. OCP monitoring has been demonstrated to

be an advantageous method to monitor the corrosion of Si in neutral media (0.01 M PBS) and confined geometries simulating physiological conditions and studying crevice corrosion.[19] The OCPs in confined areas were more negative and had larger changes through time which allowed a demonstration of their higher corrosion rates compared to bulk conditions.[19] OCP monitoring was implemented by Lai et al.[13] studying the corrosion of macroporous silicon in NaOH solutions. The corrosion of Si was evaluated in 0.1, 0.2, 0.5, and 1.0 M NaOH solutions. The initial OCP in 0.1 M and 0.2 M were , around -1.12 V vs. Ag/AgCl. However, during the course of the 800 s of monitoring the OCP, a large change was observed only in 0.2 M NaOH. The large change occurred in 0.2 M as the OCP went from -1.12 V vs. Ag/AgCl to -1.36 V vs. Ag/AgCl. The large shift of OCP to lower potentials was attributed to the dissolution of the silicon dioxide layer.[13] Such change was not evident at a lower concentration of 0.1 M within 800 s. In the case of the higher concentrations at 0.5 M and 1.0 M, the initial potentials were -1.16 and -1.32 V vs. Ag/AgCl, respectively. A sudden shift to a lower potential of -1.44 vs. Ag/AgCl occurred in the initial 50 s, under both concentrations. Overall, the results demonstrate that the increase in NaOH concentration causes the potential to shift negatively due to the increased corrosion of silicon.[13]

In the present study, the OCP results for a set of Au/Si wafters in the different electrolytes (i.e., LiOH, NaOH, and KOH) are shown in Fig. 3.2a. The high anodic potential observed at the initial OCP in all electrolytes demonstrated the presence of stable Si-oxide species. The initial OCPs of LiOH, NaOH, and KOH were: 0.80 V, 0.75 V, and 0.67 V vs. RHE, respectively. The initial OCPs follow in the order LiOH < NaOH < KOH, going to higher negative potentials as the strength of the base increases. During the 5 h measurement time, LiOH showed no significant shifts in OCP. On the other hand, when the electrolyte was NaOH or KOH, large shifts in the OCP were observed. The large change in OCP occurs at around 120 min in NaOH and

approximately 80 min in KOH. Therefore, the time it takes for the silicon oxide to be corroded increases KOH < NaOH < LiOH and can be attributed to the decrease in the size of the alkali metal cation. The large difference in potential is attributed to the etching of the silicon oxide layer, and this change can be used to identify how fast the silicon oxide layer is etched.

At the same time, the change in OCP can provide a non-quantitative method to evaluate the extent of silicon dioxide and silicon corrosion. The differences in potential between the initial OCP and the final OCP over 5 h are -0.15 V, -0.91 V, and -0.36 V for the LiOH, NaOH, and KOH solutions, respectively. A large potential variation indicates higher active corrosion, which drives the OCP to lower negative voltage. The potential after 5 hours stabilized around 0.65 V for LiOH, -0.16 V for NaOH, and 0.31 V for KOH all vs. RHE. Interestingly, the OCP monitoring also showed that after 5 h, the voltage stabilized at a lower potential in NaOH compared to KOH. Therefore, these results suggest that the corrosion increased following LiOH < KOH < NaOH.

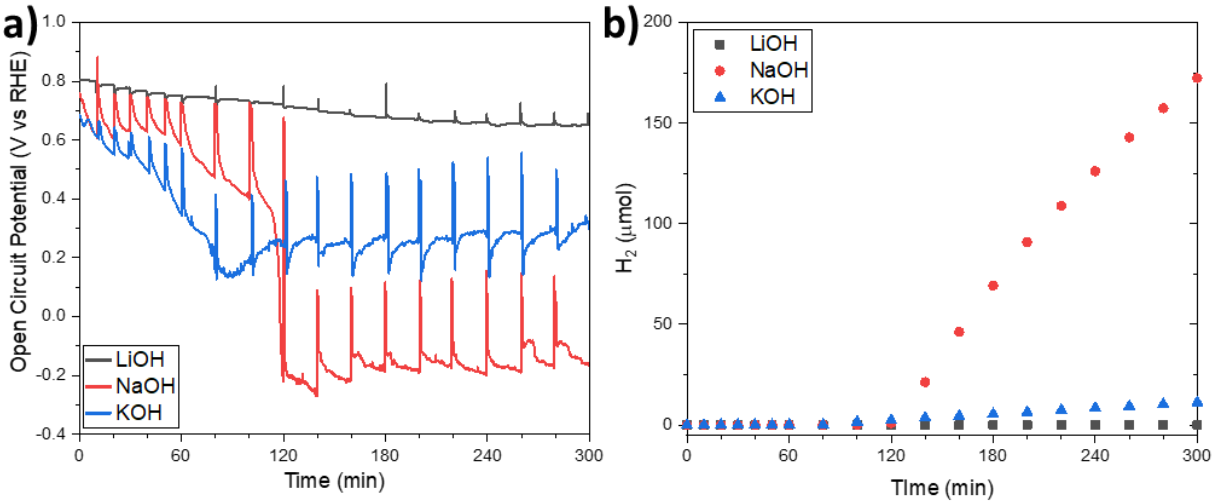

Fig. 3.2. a) Free corrosion potential evaluation of Au/Si in 0.1M LiOH, NaOH, and KOH. b) H_2 quantification during OCP measurements.

3.3.2 Hydrogen Quantification

To evaluate the activation of the self-oxidizing reaction, H_2 production was also measured. H_2 quantification was performed simultaneously with the OCP experiments, and results are shown in Fig. 3.2b. Digital images collected throughout the experiment are shown in Fig. S3.2-S3.4 and visually demonstrate that the bubbles observed on the Si substrate are H_2 bubbles.

The H_2 production results monitored by the GC measurements (Fig. 3.2b) agree with the visual observations (Fig. S3.2-S3.4). In NaOH electrolyte, H_2 was initially detected at 100 min and visually observed at 120 min (Fig. S3.2). When tested in KOH, the H_2 was produced earlier as the initial H_2 was detected at 80 min and visually observed at 100 min (Fig. S3.3). No H_2 was detected for the experiments performed in LiOH. The H_2 measurement results agree with the OCP monitoring results and can be used in conjunction to have a clear understanding and distinguish between the different stages of silicon corrosion through time and compare the electrolytes (LiOH, NaOH, and KOH). The large shift in OCP and the start of production of H_2 demonstrate the transition of the silicon etching step. The silicon corrosion transitions from silicon oxide etching (Eq. 3) to silicon etching (Eq. 4).

As mentioned previously, the change in OCP and the final OCP value provide an idea of the extent of corrosion; however, this approach does not provide a quantitative method to compare the amount of silicon corroded. Nonetheless, the OCP results suggested that the extent of silicon corrosion followed LiOH < KOH < NaOH. Indirectly, the quantification of H_2 can be used as a method to determine the silicon etching. The total hydrogen produced after 300 min was 172 µmol, 11 µmol, and 0 µmol when NaOH, KOH, and LiOH were the electrolyte. The H_2 quantification results show that the largest amount of H_2 was detected when NaOH was the electrolyte, followed by KOH, whereas no H_2 was detected when LiOH was the electrolyte.

Unexpectedly, the extent of corrosion and silicon activation to produce hydrogen does not increase as the strength of the base increases.

The only study that has previously been able to demonstrate the transition between the silicon oxide etching and silicon etching steps was performed in different NaOH concentrations.[9] The silicon dioxide etching time was found to decrease as the concentration of NaOH increases. Huang and Tao attributed the decrease in time to be due to the concentration of NaOH.[9] A comparison between different alkaline solutions (KOH and NaOH) at the same concentration was performed by Lai et al.[12] Weight loss measurements were used to demonstrate that silicon corroded faster in KOH over NaOH solutions of the same concentration. Lai et al. attributed the faster corrosion to be due to the base strength, in contrast to our results.[12] Fulong et al. evaluated the corrosion and micro-protuberances through atomic force microscopy (AFM) and found little difference in the surface shape of islands formed in KOH and NaOH solutions.[14] Therefore, Fulong et al. concluded that K^+ and Na^+ cations do not affect the etching rate and shapes of micro-island formations.[14] Seidel et al. evaluated the corrosion of KOH, NaOH, and LiOH in 10% - 60%, 24%, and 10 wt% concentrations.[11] Even though a comparison between the same concentration was not made for all solutions, it was stated that no significant difference in etching behavior could be found when comparing LiOH, NaOH, and KOH.[11] The role of the cations K^+, Na^+, and Li^+ was neglected from their analysis. However, Seidel et al. states that cations may influence the potential distribution within the inner Helmholtz layer and associates this effect to be dependent on the size and specific solvation of the cation.[11]

Overall, the results show that silicon dioxide etching and silicon etching are dependent on the base composition. The results show that the time it took to etch the silicon dioxide layer decreased as the strength of the base increased (LiOH < NaOH < KOH). However, the overall

extent of corrosion of silicon increased following LiOH < KOH < NaOH. This result demonstrates that the electrolyte composition, and specifically the alkali cation type, influences the stability of the surface Si-oxide species and causes varying degrees of active corrosion of the Au/Si electrodes. The free corrosion potential evaluation complemented with the H_2 quantification results demonstrated that the silicon dioxide etching is required to allow the silicon etching/self-oxidation to proceed.

3.3.3 Si Surface Speciation After Open Circuit Voltage

The surfaces of the Si side of the electrodes were then evaluated using x-ray photoelectron spectroscopy (XPS). Au/Si wafers exposed to the alkaline solutions for 5 hours during the free corrosion experiments were compared to a pristine, as-received Au/Si wafer. The resulting Si 2p spectra in Fig. 3.3 show two distinct peaks. The peak at 99.6 eV is attributed to Si^0, and the peak at a higher binding energy of 103.6 eV is attributed to Si^{4+}.[7,20] The as-received Au/Si wafer demonstrates the presence of a SiO_2 chemical species on the surface. However, the Si^{4+}/Si^0 peak ratio decreases when the electrodes are subjected to the alkaline solution for 5 hours. Further, the Si^{4+}/Si^0 peak ratio aligns with the corrosion and H_2 production results as a function of electrolyte composition, where the ratio is the smallest for NaOH and increases from NaOH to KOH and LiOH. The XPS results demonstrate the loss of the SiO_2 on the surface through the corrosion in the alkaline solutions, leading to the exposure of the Si^0, thus causing activation of the Au/Si. Similarly, Ning et al.[7] demonstrated the presence of the active Si^0 on the surface of unreacted silicon nanowires after electrochemical etching in 9.8 M HF. At the same time, Ning et al. showed the formation of the silicon dioxide Si^{4+} on the surface, which inhibited further reaction of Si with water and stopped the hydrogen production.

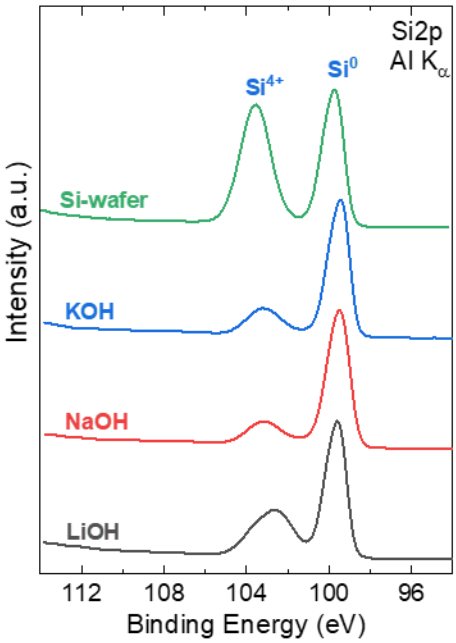

Fig. 3.3: XPS of the Si backside evaluated in LiOH, NaOH, and KOH of Au/Si after 5 h OCP and compared to a pristine, as-received Au/Si wafer.

3.3.4 H_2 Production Under Applied Current Conditions

To evaluate the application of the $Fe_xNi_{100-x}O_y$/Si two-sided electrodes for H_2 production, chronopotentiometry (CP) was performed. The current was held at -10 mA at repeating intervals of 10 min for a total of 1 h. Fig. S3.5 shows the voltage results from the CP. The CP results agree with those initially obtained from the LSV. The CP results demonstrate once more that $Fe_{80}Ni_{20}$/Si requires a lower voltage than $Fe_{20}Ni_{80}$/Si at -10 mA.

To further investigate the application of the two-sided electrodes, hydrogen production was determined between the CP intervals. During the CP and hydrogen quantification experiments, two sets of samples were tested. The first consisted of a $Fe_xNi_{100-x}O_y$ electrocatalyst that was electrodeposited onto an Au/Si wafer but had the Si side covered to prevent any contact of the Si with the electrolyte. The other set of samples consisted of the two-sided electrode $Fe_xNi_{100-x}O_y$/Si where the Si side was allowed to be in contact with the electrolyte. The H_2 measured for the

$Fe_{20}Ni_{80}$ and $Fe_{80}Ni_{20}$ compositions with the Si covered are found in Fig. S3.6 and Fig. S3.7, respectively. As the current density applied over time was held constant at -10 mA, the amount of hydrogen production by the $Fe_{20}Ni_{80}$ and $Fe_{80}Ni_{20}$ compositions with the Si covered in the different electrolytes are all close to 186 μmol. The amount of hydrogen produce matches the theoretical hydrogen as shown in the FE results in Fig. 3.4 (open symbols). Therefore, the results demonstrate that when the Si is covered, all of the charge is used in the production of hydrogen. On the other hand, the H_2 measured for the $Fe_{20}Ni_{80}$/Si and $Fe_{80}Ni_{20}$/Si compositions with the Si exposed are found in Fig. S3.8 and Fig. S3.9, respectively. It is essential to highlight that the electrolyte solution was mixed vigorously to ensure all the H_2 bubbles were removed from the electrode and forced to the headspace before the H_2 was measured to provide an accurate H_2 determination. Pictures of the cathode during the 10 min intervals were obtained. Images from when $Fe_{80}Ni_{20}$/Si and $Fe_{20}Ni_{80}$/Si compositions were evaluated in LiOH, NaOH, and KOH are shown in Fig. S3.10 and Fig. S3.11, which correspond to the experimental results presented in Fig. S3.8 and S3.9 and the calculated Faradaic efficiency (FE) values in Fig. 3.4. The FE values were calculated by estimating the theoretical H_2 produced using the total charge passed assuming 100% Faradaic efficiency compared to the measured H_2.

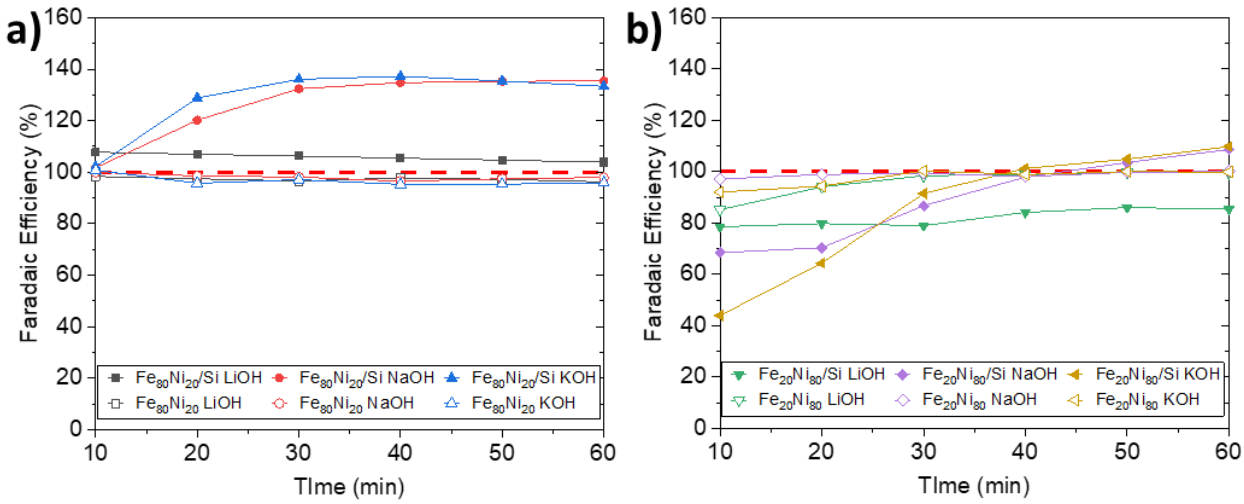

Fig. 3.4. Faradaic efficiency for HER evaluated in 0.1M LiOH, NaOH, and KOH electrolyte solutions for a) $Fe_{80}Ni_{20}$/S and $Fe_{80}Ni_{20}$ b) $Fe_{20}Ni_{80}$/Si and $Fe_{20}Ni_{80}$.

The FE values of $Fe_{80}Ni_{20}$ and $Fe_{80}Ni_{20}$/Si are plotted in Fig. 3.4a and that of $Fe_{20}Ni_{80}$ and $Fe_{20}Ni_{80}$/Si in Fig. 3.4b. When the Si side was prevented to be in contact with the alkaline electrolyte solutions, both $Fe_{80}Ni_{20}$ and $Fe_{20}Ni_{80}$ electrodes had a FE close to 100%. However, when the two-sided $Fe_{80}Ni_{20}$/Si and $Fe_{20}Ni_{80}$/Si were evaluated, a higher amount of H_2 was detected than the theoretically expected from the total charge passed. The FEs of all $Fe_{80}Ni_{20}$/Si experiments were above 100%. In the case of $Fe_{20}Ni_{80}$/Si, the FE was above 100% only when NaOH and KOH were the electrolytes and only after 50 min.

When comparing the effect of the electrolyte composition, the FE remained relatively stable in LiOH, for both electrodes. However, when the other electrolytes (i.e., NaOH and KOH) were used, an increase in the FE was observed. Such increase occurs at 20 min for the $Fe_{80}Ni_{20}$/Si and 30 min when $Fe_{20}Ni_{80}$/Si was the electrode. The rise in FE is attributed to the activation of the Si, which allows the self-oxidizing reaction to occur and thus produce more H_2 than expected. These results agree with the previous hydrogen measurements during the free corrosion potential evaluation. The OCP evaluation demonstrated that the Si is activated in KOH and NaOH but not

under LiOH. Similarly, Si is activated in KOH and NaOH under a cathodic current, resulting in significant differences in FE and ultimately FE values above 100%. The total hydrogen produced by $Fe_{80}Ni_{20}$/Si in KOH and NaOH was 248 μmol and 252 μmol, respectively, after 1 h as shown in Fig S3.9. The total hydrogen produced by $Fe_{20}Ni_{80}$/Si in KOH and NaOH was 204 μmol and 202 μmol, respectively. In both electrodes, the amount of hydrogen produced was similar between KOH and NaOH. These results are different to those observed when the Si activity was evaluated at OCP in KOH and NaOH, as more hydrogen was produced by NaOH compared to KOH. This can be attributed to a difference in the mechanism of activation.

The activation of the Si occurred within 1 hour when a cathodic current was applied. The time when the Si is activated can be estimated to be between the points where a large difference in FE is observed. In the case of $Fe_{80}Ni_{20}$/Si this can be attributed to occur between the 10 and 20 min whereas in the case of $Fe_{20}Ni_{80}$/Si between 20 and 30 min. The visual evaluation of the Si agrees with this conclusion, as shown in Fig. S3.10 and S3.11. A large increase in the number of visible bubbles is noted between 10 min and 20 min on the Si side of the $Fe_{80}Ni_{20}$/Si electrode evaluated in NaOH and KOH, Fig. S3.10. However, when the electrode was $Fe_{20}Ni_{80}$/Si, the number of visible bubbles significantly increased between 20 min and 30 min, Fig. S3.11. During the OCP evaluation, it was demonstrated that the Si was activated after around 80-100 min. Thus, these results show that the application of a reductive current accelerates the removal of the oxide layer, allowing Si to be activated faster. During OCP the activation of silicon is controlled by the etching of the silicon dioxide through the chemical reaction. However, under a reductive current, the dominant etching mechanism becomes the electrochemical reduction mechanism. The electrochemical etching mechanism can be demonstrated by the low FE observed during early times in Fig. 3.4b. The low FE in $Fe_{20}Ni_{80}$/Si demonstrates that the total charge applied is used in

an electrochemical reduction reaction other than the HER (i.e., reduction of silicon dioxide). This method has been proposed for the application of high-purity silicon for silicon semiconductors,[21] as well as to prepare water-reactive silicon for the application of producing hydrogen.[22]

3.3.5 Si Surface Speciation after Chronoamperometry

The electrodes were evaluated using XPS after the CP experiments to evaluate if the Si was activated. The XPS results of the Si 2p spectra are shown in Fig. 3.5. As mentioned previously, the peak at lower binding energies (~99 eV) is attributed to Si^0, and the peak at higher binding energies (~103 eV) to Si^{4+}.[7] The XPS spectra of the $Fe_{80}Ni_{20}$/Si and $Fe_{20}Ni_{80}$/Si tested for 1 hour in NaOH and KOH demonstrate that the Si backside is mainly composed of Si^0. On the other hand, when the electrodes were evaluated in LiOH, SiO_2 remained on the surface, as demonstrated by the Si^{4+} peak. The XPS results support the hydrogen quantification results as they show that the Si was activated in KOH and NaOH but not in the case of LiOH. The application of the $Fe_xNi_{100-x}O_y$/Si takes advantage of the alkaline electrolyte and the reductive current to allow the activation of Si and prevent the self-limiting oxidation reaction.

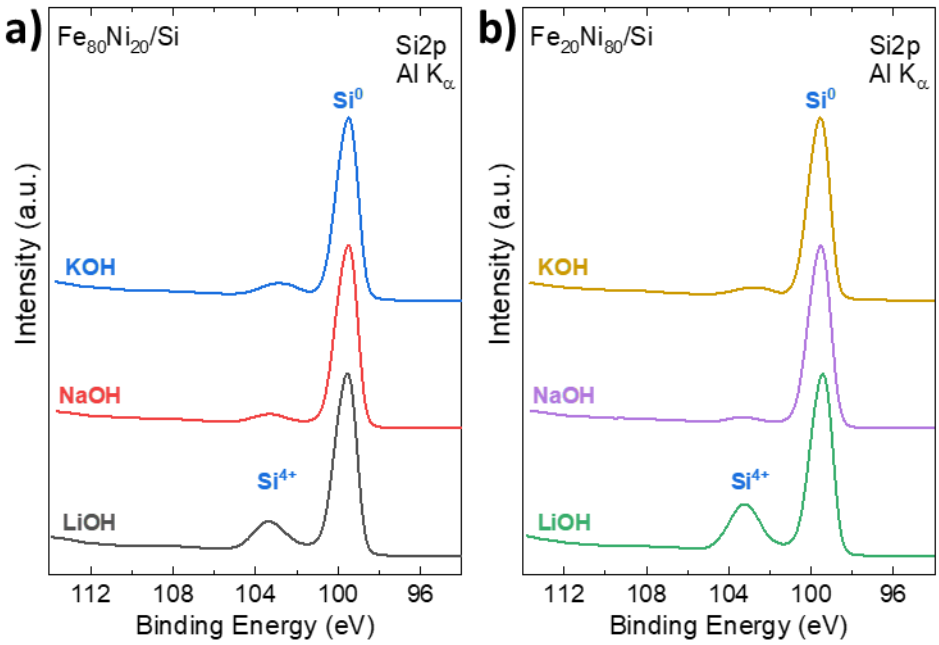

Fig. 3.5: XPS of the Si backside evaluated in LiOH, NaOH, and KOH of a) $Fe_{80}Ni_{20}$/Si and b) $Fe_{20}Ni_{80}$/Si post 1 h of potential hold at @-10 mA.

The comparison of the different two-sided electrodes tested shows that the design of the two-sided electrode can be tuned to improve the overall hydrogen production as well as the cell potential. When comparing the $Fe_{80}Ni_{20}$/Si and $Fe_{20}Ni_{80}$/Si under the 1 h CP experiments, a maximum of 140% FE was obtained by $Fe_{80}Ni_{20}$/Si. At the same time, the cathode potential for $Fe_{80}Ni_{20}$/Si was around 50 mV lower than that of the $Fe_{20}Ni_{80}$/Si during the CP experiments. These results demonstrate the advantage of combining an electrochemical catalyst with a self-oxidizing material.

3.4 Conclusions

Herein, we demonstrate that two-sided electrodes composed of $Fe_xNi_{100-x}O_y$/Si can be used to produce H_2. The electrocatalytic activity of $Fe_xNi_{100-x}O_y$ films were implemented to allow the HER to proceed on one side of the electrode. At the same time, the activation of Si was achieved under the reductive electrochemical and the alkaline conditions, allowing the self-oxidizing

reaction of Si to produce H_2. The simple design of a planar $Fe_xNi_{100-x}O_y$ electrodeposited on a Si wafer allowed a $Fe_{80}Ni_{20}$/Si electrode that was held at -10 mA for 1 h to obtain faradaic efficiencies up to 140%. This work provides the design of a simple two-sided electrode composed of abundant materials such as Si, Fe, and Ni to allow the production of H_2.

References

1 Dingenen, F. & Verbruggen, S. W. Tapping hydrogen fuel from the ocean: A review on photocatalytic, photoelectrochemical and electrolytic splitting of seawater. *Renewable and Sustainable Energy Reviews* **142**, 110866 (2021).

2 Roger, I., Shipman, M. A. & Symes, M. D. Earth-abundant catalysts for electrochemical and photoelectrochemical water splitting. *Nature Reviews Chemistry* **1**, 1-13 (2017).

3 Zhang, D., Shi, J., Zi, W., Wang, P. & Liu, S. Recent Advances in Photoelectrochemical Applications of Silicon Materials for Solar-to-Chemicals Conversion. *ChemSusChem* **10**, 4324-4341 (2017).

4 Maier, T. L. *et al.* Lateral silicon oxide/gold interfaces enhance the rate of electrochemical hydrogen evolution reaction in alkaline media. *The Journal of chemical physics* **152**, 154705 (2020).

5 Morales-Guio, C. G. *et al.* Solar hydrogen production by amorphous silicon photocathodes coated with a magnetron sputter deposited Mo2C catalyst. *Journal of the American Chemical Society* **137**, 7035-7038 (2015).

6 Esposito, D. V., Levin, I., Moffat, T. P. & Talin, A. A. H 2 evolution at Si-based metal–insulator–semiconductor photoelectrodes enhanced by inversion channel charge collection and H spillover. *Nature Materials* **12**, 562-568 (2013).

7 Ning, R. *et al.* On-demand production of hydrogen by reacting porous silicon nanowires with water. *Nano Research*, 1-6 (2020).

8 Erogbogbo, F. *et al.* On-demand hydrogen generation using nanosilicon: splitting water without light, heat, or electricity. *Nano letters* **13**, 451-456 (2013).

9 Huang, W.-H. & Tao, M. 1-4 (IEEE).

10 Seidel, H., Csepregi, L., Heuberger, A. & Baumgärtel, H. Anisotropic etching of crystalline silicon in alkaline solutions: II. Influence of dopants. *Journal of the Electrochemical Society* **137**, 3626 (1990).

11 Seidel, H., Csepregi, L., Heuberger, A. & Baumgärtel, H. Anisotropic etching of crystalline silicon in alkaline solutions: I. Orientation dependence and behavior of passivation layers. *Journal of the electrochemical society* **137**, 3612 (1990).

12 Lai, C. *et al.* Study on corrosion of porous silicon in KOH and NaOH solution. *Corrosion engineering, science and technology* **49**, 386-389 (2014).

13 Lai, C. *et al.* Study on corrosion of macroporous silicon in sodium hydroxide solution by electrochemical methods and scanning electron microscopy. *International Journal of Corrosion* **2015** (2015).

14 Fulong, Y. *et al.* Micro-fabrication of crystalline silicon by controlled alkali etching. *Journal of materials processing technology* **149**, 567-572 (2004).

15 Brack, P. *et al.* Activation of silicon towards hydrogen generation by pelletisation. *Journal of Alloys and Compounds* **704**, 146-151 (2017).

16 Gong, M., Wang, D.-Y., Chen, C.-C., Hwang, B.-J. & Dai, H. A mini review on nickel-based electrocatalysts for alkaline hydrogen evolution reaction. *Nano Res* **9**, 28-46 (2016).

17 Li, D., Liu, H. & Feng, L. A review on advanced FeNi-based catalysts for water splitting reaction. *Energy & Fuels* **34**, 13491-13522 (2020).

18 Bakovic, S. I. P. *et al.* Electrochemically active surface area controls HER activity for FexNi100− x films in alkaline electrolyte. *Journal of Catalysis* **394**, 104-112 (2021).

19 Ilic, E., Pardo, A., Hauert, R., Schmutz, P. & Mischler, S. Silicon corrosion in neutral media: the influence of confined geometries and crevice corrosion in simulated physiological solutions. *Journal of The Electrochemical Society* **166**, C125 (2019).

20 Kobayashi, Y., Matsuda, S., Imamura, K. & Kobayashi, H. Hydrogen generation by reaction of Si nanopowder with neutral water. *Journal of Nanoparticle Research* **19**, 176 (2017).

21 Nohira, T., Yasuda, K. & Ito, Y. Pinpoint and bulk electrochemical reduction of insulating silicon dioxide to silicon. *Nature materials* **2**, 397-401 (2003).

22 Yang, X., Nohira, T. & Sohn, I. Electrochemical Preparation of Water-Reactive Silicon with Potential Applications in Hydrogen Generation. *Journal of the Electrochemical Society* **167**, 022510 (2020).

4. Chapter 4. Hydrogen evolution reaction (HER) under buffered neutral conditions: Evaluation of $Fe_xNi_{100-x}O_y$ electrodes in sodium phosphate electrolyte

Authors: Sergio I. Perez Bakovic, Prashant Acharya, and Lauren F. Greenlee

Abstract

$Fe_xNi_{100-x}O_y$ films were evaluated as electrocatalysts for the hydrogen evolution reaction (HER) in neutral buffered conditions. The electrochemical activity was compared through linear sweep voltammetry (LSV) and chronoamperometry (CA) experiments performed in sodium phosphate electrolyte at neutral pH. The electrochemical experiments were corroborated by the quantification of hydrogen produced determined through gas chromatography (GC). Additionally, a comparison of the surface chemistry of the electrocatalyst films was performed through x-ray photoelectron spectroscopy (XPS). The electrochemical activity of the electrocatalyst films followed the trend of $Fe_{80}Ni_{20}$ > $Fe_{100}Ni_0$ > $Fe_{50}Ni_{50}$ > $Fe_{20}Ni_{80}$ > Fe_0Ni_{100} for the $Fe_xNi_{100-x}O_y$ compositional suite of films. The hydrogen produced by $Fe_{80}Ni_{20}$ was three times the total amount produced by Fe_0Ni_{100} when the electrodes were held at -0.7 V vs. RHE. However, a loss of 11% of the FE accompanied the higher electrochemical activity of the $Fe_{80}Ni_{20}$ electrode. Post-electrochemistry surface chemistry analysis demonstrated that there is a direct interaction of the electrolyte components (i.e., phosphate (PO_4^{3-}) and sodium (Na^+)) with the high iron content electrodes. At the same time, a change in the chemical state of iron demonstrates the reduction of the electrode during the electrochemical experiment. The hydrogen quantification and surface characterization demonstrate the presence of additional side reactions that lead to losses in FE and add evidence of the direct interaction of the electrode with the electrolyte components. Electrolyte-electrode interactions, including deposition of both cation and anion species, appear to be dependent on the composition of the $Fe_xNi_{100-x}O_y$ electrode.

4.1 Introduction

The conversion and storage of renewable energy sources is considered essential to establish a sustainable economy. Electrocatalytic reduction reactions of water,[1] carbon dioxide (CO_2),[2] and nitrogen (N_2)[3] have attracted attention as sustainable methods to create alternative fuels and chemicals of added value, including hydrogen, methane, and ammonia. In the past years, a significant amount of work has been focused on the innovation and development of catalysts, concentrating on enhancing the rate, selectivity, and efficiency of production of the desired compound.[4-6]

The hydrogen evolution reaction (HER) is the half redox reaction that occurs during water electrolysis at the cathode where hydrogen (H_2) gas is produced. H_2 is an attractive energy carrier due to its high gravimetric energy density (143 MJ kg^{-1}).[7] Historically, HER studies have been performed in acidic or alkali electrolytes; however, few studies have been performed in neutral electrolyte conditions.[8,9] Interest in neutral pH conditions has attracted attention as the milder conditions provide safety advantages,[10] prevent the corrosion of materials,[11] and potentially allow the use of seawater overall,[8] reducing the cost of H_2 production.[12] A recent review published in 2020 by Zhou et al. summarizes the recent advancements as well as current understandings of HER in neutral electrolyte reaction mechanism.[13]

The mechanism of the HER under neutral conditions is still under debate. However, HER in neutral conditions is more complicated than traditional acid or alkaline conditions as it is believed that both H_2O molecules and dissociated H_3O^+ ions participate.[13] Therefore, the HER in neutral electrolytes is considered to follow a two-step reduction process.[14-17] At low cathodic overpotential, H_3O^+ ions are the dominant reactant. As the overpotential increases and the

consumption of H_3O^+ at the surface occurs, the HER reaction becomes diffusion controlled. The switch between H_3O^+ and H_2O as the main HER reactant occurs at even higher overpotentials. As the H_3O^+ and OH^- ions are the direct reactants of water electrolysis, the buffering capacity of the electrolyte is essential to maintain the local pH. The most commonly used buffers are phosphate, borate, and (bi)carbonate buffer solutions.[13,15] Katsounaros et al.[17] demonstrated that a phosphate buffer concentration of 10^{-2} M is required to prevent changes of pH at the surface for current densities up to 1 mA cm^{-2}. Later, Shinagawa et al.[16] studied the effect of sodium phosphate (NaH_2PO_4) concentrations in the range of 0.2 to 4.2 M at a pH of 5. Shinagawa et al. found that the HER activity in phosphate buffer reaches a maximum at 1.8 M.[16] The microkinetic models show that that the overall HER overpotential is primarily controlled by the concentration-based contribution to the overpotential, contributing more than 50% of the required overpotential at -10 mA cm^{-2} under neutral buffer conditions tested.[16] As mentioned by Shinagawa and Takanabe, two possibilities for the electrochemical HER improvement in phosphate buffered conditions are 1) the close proximity of the phosphate ions to the electrode surface or 2) direct decomposition of the phosphate anion on the surface, which allows phosphate molecules to act as proton sources.[15] The identity of the electrolyte anion and cation of buffer solutions has also been critical to improving the HER and suppressing the oxygen reduction reaction (ORR).[18] These results show that through the engineering of the electrolyte, the HER can be improved and that the roles of the electrolyte anion and cation in controlling the HER are important to understand.

More recently, studies have implicated cations and anions in roles ranging from mediating nitrogen reduction[19,20] to acting as a source of protons[21] for reduction reactions. Cations have been shown to enhance or suppress electrochemical reduction reactions, depending on their

interaction with the electrode and the reduction reaction reactants. Modifying the electrolyte composition has been used to achieve electroreduction of CO_2[22-25] and N_2[19,20] and prevent the HER reaction. An extensive amount of literature comes from the CO_2 electroreduction research community, as it has been demonstrated that cations and anions affect the electrochemical reactions of CO_2.[21,26] Cations have also been shown to influence the selectivity towards different products.[24,26,27] By performing experiments at low voltages to minimize the influence of electrolyte polarization, Resasco et al.[26] were able to experimentally demonstrate that the alkali metal cation size affects the intrinsic rate of formation of the different CO_2 reduction products. An increase in the total current density was observed as the cation size increased. Resasco et al. suggest that such a trend is due to the cation concentration as density functional theory (DFT) calculations showed that larger hydrated cations are more energetically favored to be at the outer Helmholtz plane compared to smaller hydrated cations, thus suggesting that the concentration of cations at the outer Helmholtz plane should increase as the cation size increases. At the same time, with the help of DFT and the partial current densities for the different products, the influence of the cations on the extent of formation of the different products was attributed to the electrostatic interaction between the solvated cations located at the outer Helmholtz plane and the adsorbed species and intermediates. This work demonstrates that cations can indirectly influence the electrochemical reactions occurring at the catalytic surface. Overall, the work of Lazouski et al.[19,20] and Resasco et al.[21,26] suggests that through the correct experimental conditions, alkali metal cations may be exploited to influence reduction reactions in electrocatalysis.

On the other hand, the anion identity and concentration have also been shown to influence electrochemical reduction reactions. Following their previous cation work, Resasco et al.[21] then

studied the effects of the type of anion and anion concentration on the electrochemical reduction of CO_2. The electrochemical production of CO, $HCOO^-$, C_2H_4, and CH_3CH_2OH are not affected by the anion identity and concentration. In contrast, the electrochemical production of H_2 and CH_4 are strongly influenced by the anion identity and concentration. Resasco et al.[21] attribute the effect of the anion to the rate-limiting step of each product. This study allowed Resasco et al.[21] to propose that buffering anions such as phosphate, borate, and bicarbonate may act as a source of hydrogen in addition to the water solvent. Resasco et al. demonstrated the effects of cations and anions on the different CO_2 reduction reaction (CO2RR) products and HER on Cu.[21,26] The location of the cations was suggested to be in the outer Helmholtz plane, leading to changes in the total current densities and affecting the partial current of different products. However, an investigation to be able to support or refute the possible chemical interaction between the electrode and the electrolyte components was not performed, leaving a gap in the understanding as to how cations and anions play a role in the electrocatalyst interface, beyond size-based accumulation in the electrical double layer.

Interestingly, the chemical deposition of cations onto electrodes has been identified as a challenge for seawater electrolysis as cations present in seawater (i.e., Na^+, Ca^{2+}, and Mg^{2+}) may deposit under reductive potentials.[8] The deposition of cations poses a problem for hydrogen production as the active catalyst sites are blocked, leading to the loss in the catalytic active surface area and even, eventually, catalyst deactivation.[8,13,15] The electrodeposition of seawater components was visually noted by Lu et al. on a synthesized Mn-NiO-Ni/Ni-F (nickel foam) electrocatalyst, where a white deposit was obtained after 14 h of chronoamperometry at -0.14 V vs. RHE.[8] The chemical composition of the electrode surface post seawater electrolysis was analyzed through x-ray photoelectron spectroscopy (XPS). XPS analysis confirmed that the

white deposit consisted of Na, Ca, and Mg species. A second and third chronoamperometry test were performed sequentially on the same electrode, and the current decreased each time, thus demonstrating the loss of activity. In addition, the Faradaic efficiency of H_2 decreased from 100% at 1 h to 70% after 7 h. This result demonstrates that 30% of the total charge was attributed to other side reactions other than the production of H_2 at the cathode after cation deposition. The deposit was shown to be removed by immersing the electrode in dilute acid (0.5 M HCl), as demonstrated through XPS. A comparison of the Ni 2p spectra of the electrode post-electrocatalysis and after acid cleaning was performed by Lu et al.,[8] from which no significant differences were identified. However, the lack of comparison with the Ni 2p XPS spectra prior to electrochemistry, evaluation of the chemical state of Mn, the other main component of the electrode, and determination of the chemical state of the deposited layer composed of Na, Ca, and Mg leave open questions as to how the cathodes interact with the electrolyte species and how the surface chemistry of the electrode is or is not altered.

Apart from the study on seawater by Lu et al.,[8] we find few studies in the electroreduction catalysis literature that have identified cations deposited on the electrode post-electrochemistry; studies to investigate whether and how cations incorporate chemically into or onto the electrode surface, including whether there is an influence of electrocatalyst composition, have not been widely performed.[28,29] As noted in prior literature, the compositional properties of the electrode are factors to consider when evaluating the effect of cations and anions, but the focus of most research has been to make correlations between metal composition and reduction reaction activity/selectivity.

The electrolyte (i.e., solvent, cation, anion) and the electrode define the liquid/solid interface and both must be considered when studying the catalytic properties.[30] Prior research shows that the

availability of proton sources from buffer electrolytes (i.e., phosphate) at the surface determines the HER current. In this study, we focus on sodium phosphate as the buffer electrolyte in neutral pH conditions, and we demonstrate a compositional dependence of the $Fe_xNi_{100-x}O_y$ electrocatalyst on electrolyte species chemical deposition during electrocatalytic HER studies. To the best of our knowledge, no experimental evidence of the direct interaction on the surface has been demonstrated previously, and as such, our study provides some of the first definitive chemical evidence for the chemisorption of electrolyte species on transition metal oxides during electroreduction. Here, we show through a post-electrochemistry surface chemistry analysis, evidence of direct interaction of the electrolyte component (i.e., phosphate (PO_4^{3-})) and sodium (Na^+)) with the electrocatalyst surface. At the same time, the HER electrochemical activity and production were evaluated. High nickel electrodes achieved the highest FE. However, the hydrogen production was increased three times with only a loss of 11% in FE when $Fe_{80}Ni_{20}$ was used.

4.2 Experimental Section

4.2.1 Chemicals

Iron(II) sulfate heptahydrate ($FeSO_4 \cdot 7H_2O$) (≥99.0%), nickel(II) sulfate hexahydrate ($NiSO_4 \cdot 6H_2O$) (≥99.99%), boric acid (H_3BO_3) (≥99.5%), sodium phosphate dibasic heptahydrate ($Na_2HPO_4 \cdot 7H_2O$) (≥98.0%), and sodium phosphate monobasic monohydrate ($NaH_2PO_4 \cdot H_2O$) (≥99.0%) all were purchased from Sigma-Aldrich. Ultrapure water (18.2 MΩ·cm) was obtained from a Milli-Q system. Substrate gold-coated silicon wafers (100 nm gold, 5 nm titanium) were purchased from Platypus Technologies.

4.2.2 Synthesis

Films of different Fe_xNi_{100-x} compositions were synthesized through electrochemical deposition. The composition of the films was controlled by modifying the ratio of Fe and Ni of the deposition bath of a total metal content of 0.1M. The electrodeposition was performed in a single compartment cell where the counter electrode was a graphite rod and the reference electrode was Ag/AgCl (3 M NaCl). The deposition was performed by holding the potential at -1.5 V vs. Ag/AgCl (3 M NaCl) for 30 seconds. The Fe_xNi_{100-x} films were deposited onto a silicon wafer coated with gold. Additional information about the synthesis method can be found on our previous work[31] as the same procedure was followed.

4.2.3 Electrochemical Measurements

The as-synthesized Fe_xNi_{100-x} films were assessed by XPS to determine the chemical composition prior to electrocatalysis experiments. Films were consequently used as electrocatalysts. The electrochemical experiment was performed in a three-electrode electrochemical cell, where the Fe_xNi_{100-x} films were used as the working electrodes, a graphite rod as the counter electrode, and Ag/AgCl (3M NaCl) as the reference electrode. An H-cell was used, and a Celgard 3401 membrane was used as a separator. Through the implementation of a chronoamperometry (CA) the potential at the working electrode was set to (-0.7 vs. RHE) for a total time of 1h. Prior to the CA, the electrolyte was de-aerated by bubbling argon (Ar) gas into the electrolyte for 30 min. During the CA, Ar gas was bubbled into the electrolyte, and the electrolyte was agitated at 400 rpm. As mentioned previously, the electrochemical experiments were performed in 0.1 M phosphate-buffered solution with a pH of 7.2. It is important to specify that the electrolyte was prepared by mixing 0.1 M sodium phosphate dibasic heptahydrate ($Na_2HPO_4 \cdot 7H_2O$) and 0.1 M sodium phosphate monobasic monohydrate ($NaH_2PO_4 \cdot H_2O$) thus

allowing the pH to be set at 7.2 without the addition of additional acid or base but leading to a higher concentration of Na around 0.17 M.

4.2.4 H_2 Determination

A gas tight H-cell was used during the electrochemical experiments. All the cell connections were sealed using Dow Corning high vacuum grease to ensure the cell was gas tight. At the same time prior to the electrochemical experiment the cell was purged with argon gas. The H_2 was directly collected using the automated pump of the 490 Micro GC system (Agilent Technologies, Inc., United states) detected with a thermal conductivity detector (TCD). The carrier gas used was Ar, the injector temperature and the column were both set to 75 °C. Prior to measuring the hydrogen, the electrolyte solution was mixed vigorously at the maximum speed of the magnetic stirrer plate of 1500 rpm to ensure the hydrogen is forced to the head space. The hydrogen was measured from both the cathode and anode side.

4.3 Results and Discussion

4.3.1 Electrochemical Characterization

The HER performance of $Fe_xNi_{100-x}O_y$ films was tested in 0.1 M neutral buffered conditions of sodium phosphate electrolyte set at a pH of 7.2. The $Fe_xNi_{100-x}O_y$ films were electrochemically deposited onto Au/Si substrates using the same procedure implemented in our previous work.[31] After the electrodes were electrodeposited, the Si substrate was covered to prevent contact with the electrolyte solution (Fig. S4.1). Chronoamperometry (CA) was performed at -0.7 V vs. RHE for 1 h in a sodium phosphate buffer solution (pH 7.2) using an H-cell. The measured current was normalized by the geometric surface area of 1 cm^2 for all samples, as shown in Fig. 4.1a.

Among the different compositions tested, the catalytic activity decreases following $Fe_{80}Ni_{20}$ > $Fe_{100}Ni_0$ > $Fe_{50}Ni_{50}$ > $Fe_{20}Ni_{80}$ > Fe_0Ni_{100}. The measured current for $Fe_{50}Ni_{50}$, $Fe_{20}Ni_{80}$, and

Fe_0Ni_{100} compositions showed a slight decrease over 1 h in neutral electrolyte. The increase in overpotential, which would cause a decrease in measured current, has been demonstrated in alkaline electrolyte for Ni, where the formation of a hydride layer under cathodic polarization is formed.[32] The deposition of Fe has been used to minimize the deactivation of Ni by preventing the formation of nickel hydride in alkaline solutions.[33] On the other hand, $Fe_{80}Ni_{20}$ and $Fe_{100}Ni_0$ electrodes resulted in an increase of current of around 2 mA cm^{-2}, demonstrating a possible increase of the electrochemical activity. However, the increase in current might also be attributed to other Faradaic processes occurring at the electrode surface.

A comparison between Fe and Ni electrodes in neutral electrolyte conditions is not found in the literature to the best of our knowledge. This could be attributed to the instability of transition metals in neutral conditions. Fe-based electrodes are unstable at pH 7.2 after no cathodic potential is applied, as observed from the loss of the post-CA electrodes in Fig. S4.1. For analysis, the electrodes had to be quickly removed from the electrolyte post-CA to prevent all the high iron content electrodes from being dissolved in the electrolyte. However, if the electrodes are kept under cathodic potential, electrode stability is maintained. Most neutral electrolyte catalytic studies have been centered on the development of transition-metal phosphides, sulfides, nitrides, and borides.[13] In the study by Zhan et al.,[9] the authors demonstrated that the doping of Fe to form $(Fe_xNi_{1-x})_2P$ improves the HER activity in neutral buffered conditions. Single-crystalline $(Fe_xNi_{1-x})_2P$ nanosheets were tested in acidic, neutral buffered, and alkaline media. The $(Fe_{0.048}Ni_{0.952})_2P$ was demonstrated to be the most active electrocatalyst in alkaline and neutral buffered 1 M phosphate buffer saline (PBS), outperforming Ni_2P.[9] Unlike in our case, where the composition of Fe went from 0 % to 100%, the range of Fe compositions studied by Zhang et al.[9] were between 2.8% to 7.7%. Nonetheless, the doping of Fe was proposed to allow

more charge accumulation around the P active sites, thus enhancing the electron transfer between P and H atoms.

In contrast, the electrochemical activity of the electrodes shown in Fig. 4.1a is different from those obtained when the same electrodes were evaluated in NaOH in our previous study.[31] In an alkaline solution, the electrochemical activity followed $Fe_{80}Ni_{20} \approx Fe_{0}Ni_{100} \approx Fe_{50}Ni_{50} > Fe_{100}Ni_{0} > Fe_{20}Ni_{80}$ when evaluated at -0.5 V vs. RHE and normalized by geometric surface area.[31] The difference in activity observed when the $Fe_xNi_{100-x}O_y$ electrodes were evaluated in alkaline and neutral buffer conditions could be due to the possibility of having both the buffer component (i.e., phosphate ions) as well as H_2O molecules as the reactants.

In addition to the CA evaluation, linear sweep voltammetry (LSV) was performed, and results are shown in Fig. 4.1b. The LSVs were performed in the same sodium phosphate solution of pH 7.2, and the electrolyte was mixed at 400 rpm in an H-cell. As highlighted in the LSV results, two different regions of electrode behavior can be distinguished. The first region can be identified at lower current densities from 0 to around -3.5 mA cm^{-2}, highlighted in blue. The second region can be identified at higher currents starting around -5 mA cm^{-2}, highlighted in red. The two-step reduction process, where the hydronium ion reduction is followed by the water reduction as the reactant switches has been shown in neutral, unbuffered electrolytes.[13,14,17,34] The switching of reactants can be evident from the two reduction features observed.[13,14,17] The first reduction step occurs at lower overpotentials where H_3O^+ is considered to be the dominant reactant. As the current density increases, the concentration of H_3O^+ can no longer sustain the higher reduction rate, and the reduction current reaches a plateau. The second reduction current has been observed to occur at -0.4 V vs. RHE when a Pt disk was evaluated in Na_2SO_4 solution.[14] The second reduction current is attributed to the reduction of water as a reactant.[14]

The change of reactant occurs as the H_3O^+ can no longer support the higher reaction rates and the higher overpotentials allow H_2O to become a reactant.

Similarly, in neutral buffered conditions, the transition of the reduction reactants has been proposed. The transitions are dependent on the buffer concentration and buffer pK_a values. These studies have proposed that buffer species can act as proton donors and suppress changes in the surface pH.[17,34] The plateaus in reaction rate represent the change in surface pH. Therefore, the current density at which the plateaus occur indicates the reaction rate at which the buffer can no longer pin the surface pH. For example, the second reduction current observed for Pt at -0.4 V vs. RHE has been attributed to the region where water becomes the reactant when evaluated at pH 2 in a 0.5 M Na_2SO_4 electrolyte.[14] Such a transition has also been experimentally observed when Pt and stainless steel (316L) were evaluated in phosphate buffer solutions at pH of 7.2.[35,36] Therefore, it has been claimed that the phosphate species act as the reactant but at the same time that the two-step reduction process also occurs in buffered neutral conditions.

Thus, our results would suggest that under the 0.1 M sodium phosphate (pH=7.2), the buffer can act as the dominant reactant up to a current density of around -3.5 mA cm^{-2}. However, later at higher overpotentials, H_2O would transition to be the reactant. These results would suggest that under the CA experiment in Fig. 4.1a, where the potential was held at -0.7 V vs. RHE, the dominant reactant would be expected to be H_2O.

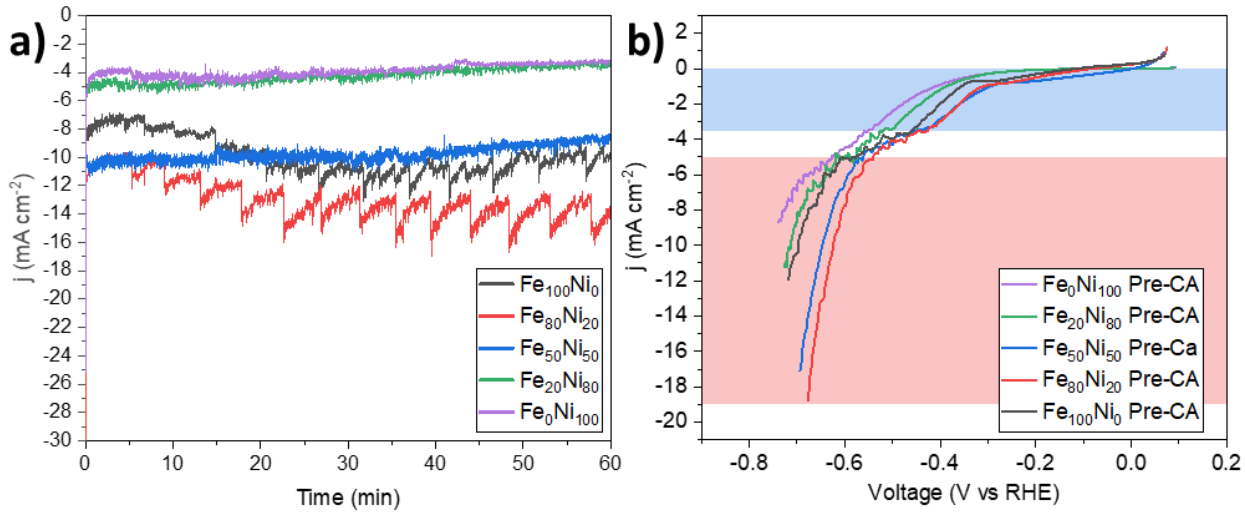

Fig. 4.1. a) Chronoamperometry results of different $Fe_xNi_{100-x}O_y$ performed at -0.7 V vs. RHE in 0.1 M phosphate electrolyte pH of 7.2 at 400 rpm b) Linear voltammetry curves for different $Fe_xNi_{100-x}O_y$ in 0.1 M sodium phosphate electrolyte at pH of 7.2 as the electrolyte was mixed at 400 rpm.

4.3.2 Hydrogen Production and Faradaic Efficiency

The increase in electrochemical activity is ideally translated into higher hydrogen production through the HER. However, the increase in reductive current may also be attributed to additional electron transfer reactions occurring at the electrode and/or electron transfer interactions between the electrode and electrolyte components. The standard reduction potentials for Fe^{2+}/Fe^0 and Ni^{2+}/Ni^0 are -0.44 V vs. SHE and -0.28 vs. SHE, respectively.[37] Under the reductive potentials required for HER (e.g., < 0 V vs. SHE) the reduction of Fe and Ni must be considered, particularly in our case where the potential was held at -0.7 V vs. RHE (-1.12 V vs. SHE) in the neutral buffered solution of pH 7.2. Therefore, the quantification of the hydrogen production is essential to be able to confidently attribute the electrochemical activity to the production of hydrogen.

The hydrogen produced during the CA experiment was determined to evaluate if the difference in electrochemical activity observed during the CA experiments in neutral buffer conditions

translated into increased hydrogen production. As the electrochemical activity is represented by the current, the increase in current can reflect the increase in the reduction reaction at the cathode, but other Faradaic processes, including electrolyte species chemisorption or transition metal reduction, can also contribute to the overall increase. The amount of hydrogen produced after the 1 h CA experiment was thus measured to study the change in current observed. The H_2 was quantified using a gas chromatography (GC) instrument equipped with a thermal conductivity detector (TCD). After the 1 h CA, the electrolyte was mixed vigorously at 1500 rpm to ensure all H_2 bubbles were forced into the headspace. The H_2 was measured in the cathode and anode sides of the cell. The amount of hydrogen in the cathode and anode quantified is reported in Table S4.1. The total amount of hydrogen is shown in Fig 4.2a. The H_2 quantification shows that the amount of H_2 produced followed $Fe_{80}Ni_{20}$ > $Fe_{50}Ni_{50}$ > $Fe_{100}Ni_0$ > $Fe_{20}Ni_{80}$ > Fe_0Ni_{100}. The results show a 3x difference of hydrogen produced between the lowest amount (Fe_0Ni_{100}) and the highest amount ($Fe_{80}Ni_{20}$). The hydrogen quantification shows that the amount of hydrogen produced by $Fe_{50}Ni_{50}$ was greater than that produced by $Fe_{100}Ni_0$. Such a difference in HER activity is not obvious from the CA results shown in Fig. 4.1a, as $Fe_{100}Ni_0$ and $Fe_{50}Ni_{50}$ current densities cross during the 1 h tested.

The total hydrogen measured after 1 h and the theoretical amount expected were used to then calculate the Faradaic efficiency (FE) of each electrode. The theoretical amount of hydrogen produced was estimated by the total charge passed during the reaction assuming 100% HER. The FE results are shown in Fig. 4.2b. The corrosion of the passivating SiO_2 layer has been demonstrated to occur in buffered neutral solutions.[38]As our previous study revealed that the exposure of Si^0 would allow the self-oxidizing reaction of Si to occur, producing H_2 spontaneously, the Si substrate was covered to prevent contact with the electrolyte. The FE of H_2

after the 1 h CA experiment reached close to 100% for Fe_0Ni_{100} and $Fe_{20}Ni_{80}$. However, in the case of the $Fe_{50}Ni_{50}$, $Fe_{80}Ni_{20}$, and $Fe_{100}Ni_0$ the FE was lower. Even though the FE is lower for $Fe_{50}Ni_{50}$, $Fe_{80}Ni_{20}$, and $Fe_{100}Ni_0$ (Fig. 4.2b), it is essential to highlight that the H_2 produced is 2-3 times higher, Fig. 4.2a. Nonetheless, the deviation indicates the presence of side reaction(s) during the CA that consumed up to 11% of the total charge in the case of the $Fe_{80}Ni_{20}$.

Unfortunately, few studies complement their electrochemical evaluation with the determination of hydrogen production. Muñoz et al.[36] has attributed part of the total charge applied to be consumed by an electrochemical reaction apart from the desired HER. A hydrogen faradaic efficiency of 91.4% was obtained when 316L stainless steel was evaluated at -1.1 V vs. SCE in 0.5 M phosphate and 0.1 M KCl electrolyte for 100 min. The amount of current used in the reduction of the oxide surface was determined by performing the same electrochemical experiment. However, the electrolyte did not contain phosphate and only consisted of the supporting electrolyte KCl, allowing the determination of the charge used in the reduction of the metal oxide. This study ultimately demonstrated that the current that was not used to produce hydrogen was redirected and consumed in the reduction of the oxide layer present on the surface of the electrode under the cathodic potential.[36]

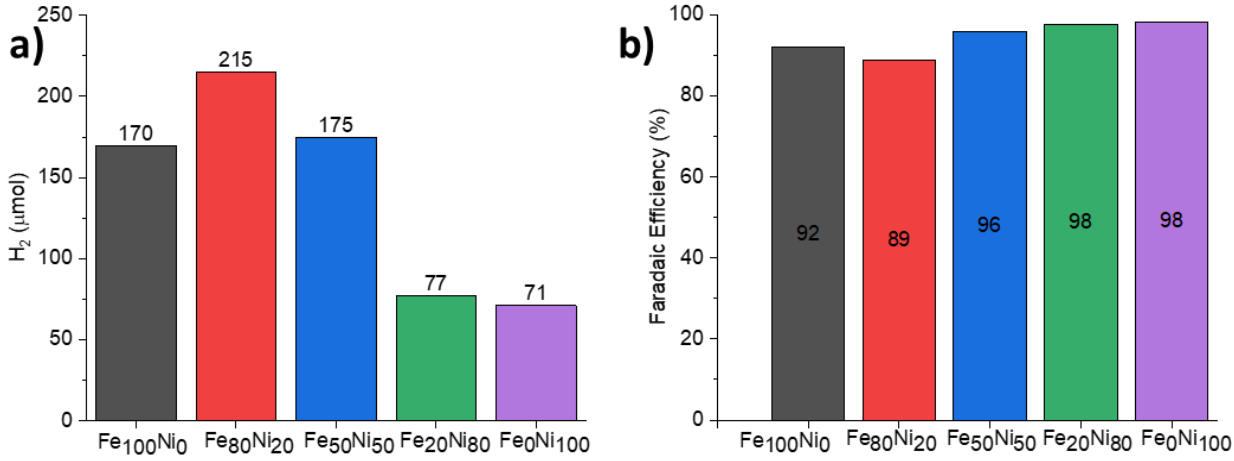

Fig. 4.2. a) H_2 produced and b) HER Faradaic efficiency (FE) calculated for $Fe_xNi_{100-x}O_y$ held at -0.7 V vs RHE in 0.1 M phosphate electrolyte for 1 h.

4.3.3 Post-electrochemistry surface chemistry analysis

To evaluate the reaction consuming the charge and to evaluate the visual changes observed on the films post-CA, the surface chemical composition was studied using XPS. First, a change in the color of the electrode post-chronoamperometry became evident. As shown in Fig S4.1, the difference was appreciable only for $Fe_{100}Ni_0$ and $Fe_{80}Ni_{20}$. Pre- and post-electrocatalysis XPS surveys of all films were compared to determine the chemical composition of the $Fe_xNi_{100-x}O_y$ electrodes, Fig. 4.3. The surface composition of the pre-catalysis films was found to be composed of only Fe, Ni, O, and C, as shown in the XPS survey spectra in Fig. 4.3a. Adventitious carbon is found on all samples; all XPS spectra were calibrated by the C 1s peak at (284.8 eV). After the $Fe_xNi_{100-x}O_y$ films were subject to 1 h potential holds at -0.7 V vs. RHE, the films were rinsed with ultra-pure water, dried with Ar gas, and stored in a vacuum-sealed bag before being tested by XPS. The post-electrocatalysis XPS survey spectra are shown in Fig. 4.3b. The post-catalysis spectra reveal the presence of P on the surface. The presence of P is only detected on $Fe_{50}Ni_{50}$, $Fe_{80}Ni_{20}$, and $Fe_{100}Ni_0$.

Only the presence of the electrolyte anion was demonstrated to be present on the surface of $Fe_xNi_{100-x}O_y$ electrodes post-CA. However, the presence of the anion (phosphate) and cation (Na) has also been observed in comparative experiments where electrodes with the silicon back side exposed were also tested. The electrodes with the silicon exposed are labeled $Fe_xNi_{100-x}O_y$/Si. The electrochemical activity and stability were evaluated by performing a chronoamperometry at -0.7 V vs RHE for 1 h in a sodium phosphate buffer solution at a pH of 7.2. The electrochemical experiments were performed in the same cell configuration however instead of having the H-cell be gas tight, argon gas was purged into the electrolyte as it was mixing at 400 rpm. The CA results are presented in Fig. S4.3. The survey XPS spectra of the post-CA $Fe_xNi_{100-x}O_y$/Si are shown in Fig. S4.6 and reveal the present of P and Na post-CA. As shown in Fig. S4.6, P and Na were present on the surface of $Fe_{100}Ni_0$/Si and $Fe_{80}Ni_{20}$/Si. Similar to the $Fe_xNi_{100-x}O_y$ electrocatalyst surfaces, the electrolyte components were demonstrated by XPS to be present of the electrolyte components on the surface of $Fe_xNi_{100-x}O_y$/Si with higher Fe content.

The presence of electrolyte cations and anions on the surface of electrodes post electrochemical experiment where the electrode potential is held at reductive potentials for the production of hydrogen has been observed in seawater and phosphate buffer solution (PBS).[8,29] Mn doped nickel/nickel oxide electrocatalysts (MnO-NiO-N/Ni-F) has been evaluated as an electrocatalyst in PBS and seawater.[8] When the MnO-NiO-N/Ni-F electrode was held at -0.17 v vs. RHE in a 1 M PBS solution, the presence of Na and P on the electrode surface post catalysts was demonstrated by XPS. Similarly, when the MnO-NiO-N/Ni-F electrode was held at -0.14 V vs. RHE in seawater a white deposit was observed on the surface. The XPS analysis demonstrated the deposit to be composed of Ca, Mg, and Na. Similarly, the presence of Na, Zn, and Ca was demonstrated through XPS to be present on the surface of a reduced iron oxide after it was held

at -0.5 V vs. RHE in 0.1 M phosphate buffer solution (PBS) at a pH of 7.2.[29] Overall, these results demonstrate that under neutral electrolyte conditions and reductive voltages applied for the hydrogen evolution reaction, anions and cations can be deposited on the electrode surface.

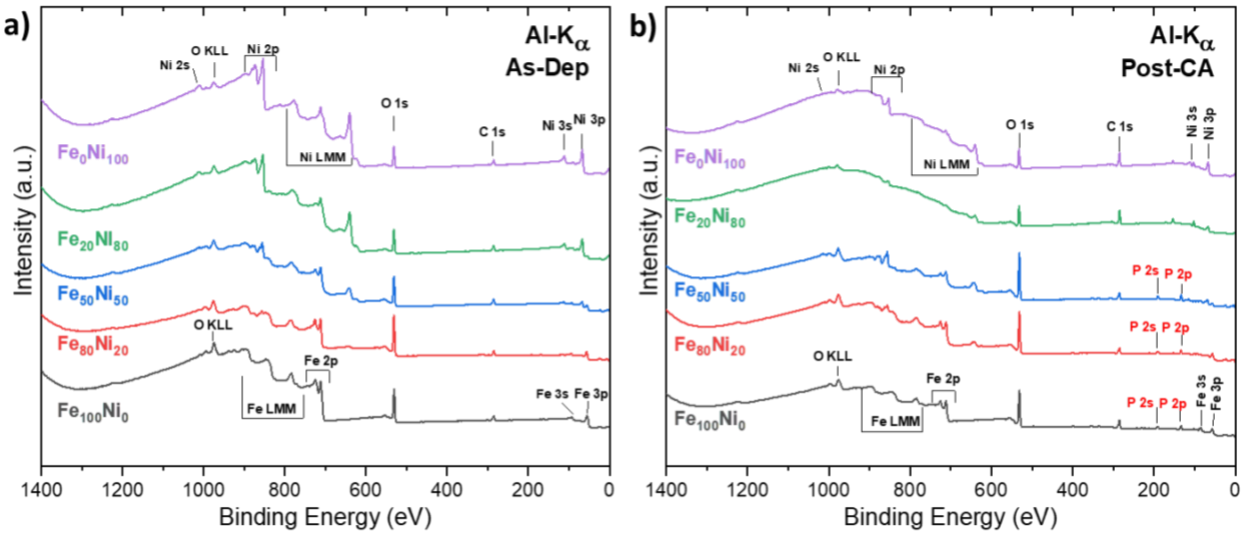

Fig. 4.3. XPS survey spectra of $Fe_xNi_{100-x}O_y$ films a) as-deposited and b) post-CA.

The high-resolution XPS spectra of Fe and Ni can be used to understand the Fe and Ni oxidation state. In the Fe 2p spectra, peaks at 706.8 eV and 720.1 eV binding energies correspond to the Fe $2p_{3/2}$ and Fe $2p_{1/2}$ doublets of metallic Fe (Fe^0).[39,40] On the other hand, peaks around 711 eV and 724 eV with their corresponding satellites at around 715 eV and 729 eV, elucidate the presence of oxidic Fe species (Fe^{2+} and Fe^{3+}).[39,40] Similarly, in the case of Ni 2p, the presence of metallic (Ni^0) nickel is apparent from the peaks at around 852.8 eV and 870 eV, attributed to Ni $2p_{3/2}$ and Ni $2p_{1/2}$.[41-43] Peaks around 856.2 eV and 874.3 eV with their respective broad satellite peaks around 861.9 eV and 880 eV, in the Ni 2p spectrum demonstrate the presence of oxidic Ni (Ni^{2+} and Ni^{3+}) species on the surface.[41-43]

As mentioned previously, a possible cause for the loss in FE can be attributed to the electrochemical reduction of the main components (i.e., Fe and Ni). The Fe 2p and Ni 2p spectra

were normalized to compare the as-deposited vs. post-CA spectra. The Ni 2p spectra demonstrate that all electrodes are composed of metallic Ni^0 as the prominent peaks of 852.8 eV and 870 eV are observed. The Ni 2p spectra show that Ni is fully reduced as-deposited, and no difference is observed from the electrodes post-CA. These results demonstrate that Ni is fully reduced; thus, consequently, during the CA experiment, Ni did not undergo further reduction.

The evaluation of the Fe 2p, on the contrary, shows changes post-CA compared to the as-deposited electrodes. Specifically, changes are observable for the compositions $Fe_{80}Ni_{20}$ and $Fe_{100}Ni_0$. The $Fe_{100}Ni_0$ XPS spectra demonstrate that the as-deposited electrode surface is mainly composed of metallic Fe^0. Further reduction of the surface was not observed from the $Fe_{100}Ni_0$ XPS spectra post-CA compared to the as-deposited. Therefore, it is unclear if, in the case of the $Fe_{100}Ni_0$ if the charge was redirected to the reduction of the surface.

In the case of the $Fe_{80}Ni_{20}$, the surface of the as-deposited electrode is mainly composed of oxidic Fe as demonstrated by the peaks at 711 eV and 724 eV while the small speak at 706.8 eV suggest the presence of metallic Fe^0. The post-CA electrode demonstrates similarly that the surface was composed of oxidic Fe. However, a greater extent of the surface was reduced to metallic Fe^0 as the peak at 706.9 eV increased. The following results demonstrate that the partial composition of oxidic Fe allows further reduction of the electrode during the CA experiment. The comparison of the as-deposited and post-catalysis samples demonstrates that the surface was reduced, as the metallic Fe features are more prevalent post-CA than as-deposited. Therefore, the following results demonstrate that some of the charge that was not directed to hydrogen production could be attributed to the further reduction of the $Fe_{80}Ni_{20}$ electrode during the CA experiment.

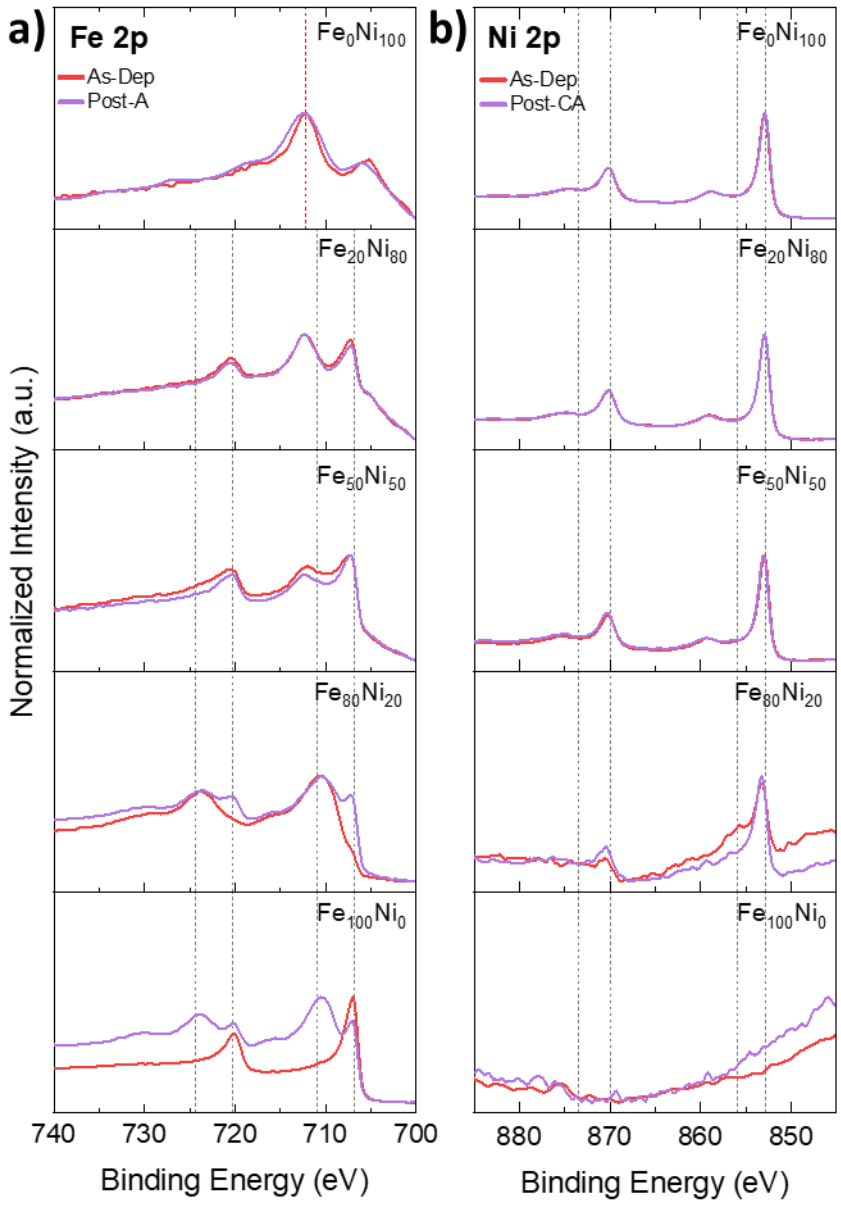

Fig. 4.4. XPS spectra of a) Fe 2p, b) Ni 2p for $Fe_xNi_{100-x}O_y$ films as-deposited vs. post-CA after Ar^+ sputtered for 5 min at 1 KeV.

The reduction of Ni and Fe could be expected as the Pourbaix diagrams for Ni and Fe show that at pH 7.2 the Ni/NiO and Fe^{2+}/Fe^0 couples are close to water reduction potential.[44-46] The electrochemical reduction of Fe in phosphate buffer solutions has been previously demonstrated. Thin films of Fe_2O_3 were studied in phosphate solutions through in situ X-ray absorption near edge spectroscopy to monitor changes in the valency and thickness.[47] The reduction of Fe_2O_3 to

metallic Fe without dissolution was demonstrated to takes place in phosphate buffer of pH 8.4 under cathodic potentials.[47] The electrochemical reduction of an oxidized iron electrode has been previously reported in 0.1 M PBS at pH of 7.2 when the potential was held at -0.5 V vs. RHE to prepare Fe/Fe oxide catalyst for the electrochemical ammonia synthesis.[29] The electrochemical reduction of an oxidized electrode was demonstrated through XPS as the electrodes held at -0.5 V vs. RHE showed both Fe^0 and oxidic Fe components, indicating the partial reduction of the surface layer to metallic Fe.[29] The reduction of oxidic Fe to metallic Fe observed from our XPS results is consistent with these previous studies that observed the reduction of iron in a phosphate buffer solutions. Therefore, a portion of charge applied can be attributed to the use of charge during the reduction of the oxidic metal species of the electrodes leading to lower HER FE.

As the presence of P was identified in $Fe_{50}Ni_{50}$, $Fe_{80}Ni_{20}$, and $Fe_{100}Ni_{0,}$ high-resolution P 2p XPS spectra were obtained. The P 2p spectra were recorded for the different $Fe_xNi_{100-x}O_y$ electrodes as-deposited and post-CA (with and without Ar sputter treatment), as shown in Fig. 4.5. The P 2p spectra of the as-deposited electrodes demonstrated that P is not present in the electrodes as-deposited for all compositions. As initially identified by the survey XPS spectra, the P 2p spectra demonstrate the presence of P post-CA for the $Fe_{50}Ni_{50}$, $Fe_{80}Ni_{20}$, and $Fe_{100}Ni_0$ electrodes.

Evidence of a direct metal phosphide (M-P) interaction was not observed, as the characteristic doublet, P $2p_{1/2}$ and P $2p_{3/2}$ peaks around 130 eV from a metal-phosphide, is not present in the P 2p spectra.[48-51] The P 2p peak around 134 eV observed Fig. 4.5 is attributed to the P-O of phosphorus oxides. A peak at 132.8 eV in Co_xFe_{1-x}-P[52] has been identified as phosphate, and in other work on NiFe phosphate[53] the peak at 133.7 eV was attributed to phosphate (PO_4^{3-}). Similarly, in $Ni_{11}(HPO_3)_8(OH)_6$,[54] the peak at 133.2 eV was attributed to +3 phosphorus from a phosphite (HPO_3^{2-}) and a peak at 135.9 eV was identified as P^{5+}. Identifying the oxidation state

of phosphorus becomes complicated as phosphorus oxides with valence of +5 to +3 can be found within 136 eV to 131 eV.[55] The presence of phosphorus was evident even after 5 min and 10 min of Ar^+ in the case of the $Fe_{100}Ni_0$ and $Fe_{80}Ni_{20}$ electrodes. Thus, these results demonstrate that P is incorporated not simply on the surface during the CA experiment but appears to be incorporated into the electrocatalyst composition to a certain sub-surface depth. Therefore, the reduction or partial reduction of phosphate could be expected and may have contributed to the increase in charge transfer observed through current density measurements.

At the same time, the presence of phosphate on the electrodes post-CA could indicate that that increase in cathodic current observed may be attributed to an increase in the catalytic activity of the electrodes. The electrodeposition of cobalt and iron with phosphorus has been implemented as a synthesis method to develop (Co_xFe_{1-x}-P) electrodes to demonstrate their application as OER and HER bifunctional catalysts.[52] Notably, it has been demonstrated in the literature that phosphates can improve the activity of nonprecious metal catalysts. Among some of these studies, nonprecious metal catalysts such as Co_xFe_{1-x}-P,[52] $Ni_{11}(HPO_3)_8(OH)_6$,[54] NiFe phosphate[53], and $Fe_{2.95}(PO_4)_2(OH)_2$ [56] have shown that the presence of phosphate improved their catalytic activity. Therefore, the increase in activity during the -0.7 V vs. RHE could be attributed to the increase in catalytic activity by the change in the chemical state of the electrode through the incorporation of phosphate from the electrolyte. Our results demonstrate the close proximity of phosphate with the electrode during HER, thus providing additional evidence to the body of literature suggesting that phosphate can act as a proton source and be chemically integrated into the electrocatalyst structure. As mentioned by Zhou et al. HER in neutral conditions has the challenge of low conductivity, high corrosivity, and the poisoning[57] or blockage[8] of the catalyst due to undesired ions.[13] Unlike other studies that showed the

poisoning[57] or blockage[8] of the catalysts, the results found here demonstrate a positive effect depending on the electrode-electrolyte interactions.

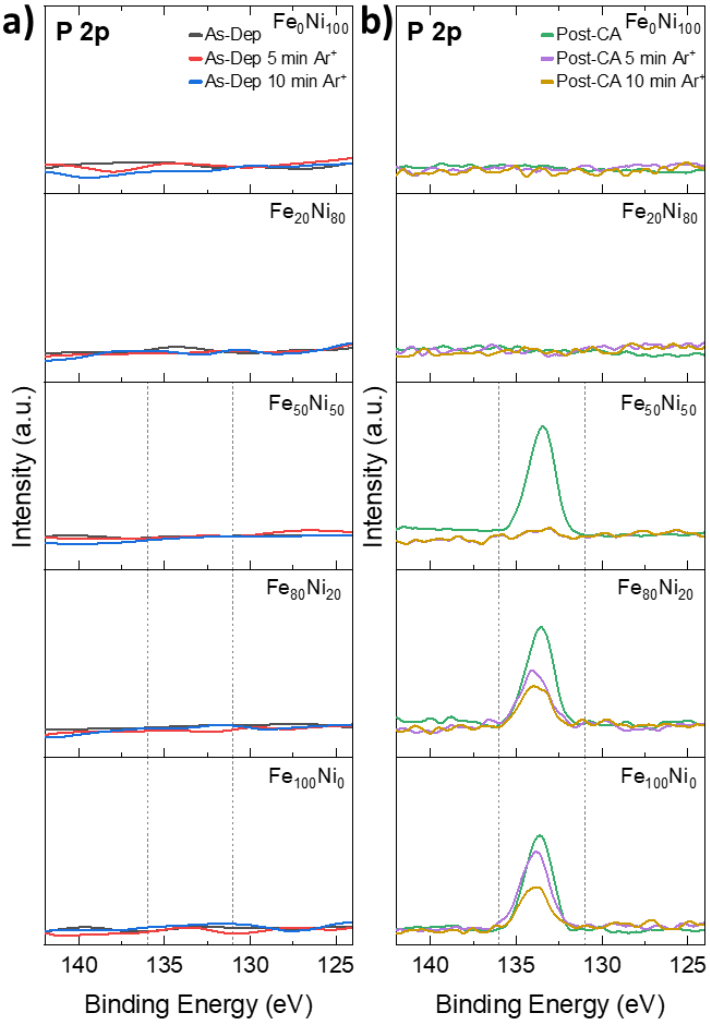

Fig. 4.5. XPS spectra of P 2p for $Fe_xNi_{100-x}O_y$ films a) as-deposited b) post-CA.

It is of importance to highlight that even though the high iron content electrodes ($Fe_{100}Ni_0$ and $Fe_{80}Ni_{20}$) demonstrated greater hydrogen production values of 215 µmol and 170 µmol and demonstrated an increase in catalytic activity through the increase of the cathodic current, the application of this catalysts is hindered by dissolution under no applied potential. The dissolution is evident from the pictures provides of the electrodes post-CA, where it can be clearly observed that the electrode was corroded. The reduced Fe^0 is oxidized to Fe^{2+} and dissolves in the

electrolyte when a cathodic current is not applied. Additional work must be done to prevent the dissolution of Fe as occasional shutdowns intentionally or unintentionally would occur during electrolysis, resulting in the loss of the catalyst.

4.4 Conclusion

Herein, $Fe_xNi_{100-x}O_y$ electrodes were evaluated as electrocatalysts for HER in neutral buffered conditions. The electrochemical activity in neutral sodium phosphate buffer solution at 7.2 pH followed $Fe_{80}Ni_{20}$ > $Fe_{100}Ni_0$ > $Fe_{50}Ni_{50}$ > $Fe_{20}Ni_{80}$ > Fe_0Ni_{100}. The electrochemical activity was validated by determining the hydrogen produced after CA at -0.7 V vs. RHE. The hydrogen produced by $Fe_{80}Ni_{20}$ was 3 times the total amount produced by Fe_0Ni_{100}. However, additional electrochemical reactions including the reduction of the electrode and deposition of electrolyte species reduced the FE of $Fe_{80}Ni_{20}$ by 11%. The direct interaction of the electrode with the electrolyte components (i.e., phosphate) was demonstrated. The following results help to demonstrate that the electrode-electrolyte interaction in neutral sodium phosphate buffer solutions.

References

1 Zhao, G., Rui, K., Dou, S. X. & Sun, W. Heterostructures for electrochemical hydrogen evolution reaction: a review. *Advanced Functional Materials* **28**, 1803291 (2018).

2 Qiao, J., Liu, Y., Hong, F. & Zhang, J. A review of catalysts for the electroreduction of carbon dioxide to produce low-carbon fuels. *Chemical Society Reviews* **43**, 631-675 (2014).

3 Foster, S. L. *et al.* Catalysts for nitrogen reduction to ammonia. *Nature Catalysis* **1**, 490-500, doi:10.1038/s41929-018-0092-7 (2018).

4 Qing, G. *et al.* Recent Advances and Challenges of Electrocatalytic N2 Reduction to Ammonia. *Chemical Reviews* (2020).

5 Yang, W. & Chen, S. Recent progress in electrode fabrication for electrocatalytic hydrogen evolution reaction: A mini review. *Chemical Engineering Journal*, 124726 (2020).

6 Kuhl, K. P. *et al.* Electrocatalytic Conversion of Carbon Dioxide to Methane and Methanol on Transition Metal Surfaces. *Journal of the American Chemical Society* **136**, 14107-14113, doi:10.1021/ja505791r (2014).

7 Mazloomi, K. & Gomes, C. Hydrogen as an energy carrier: Prospects and challenges. *Renewable and Sustainable Energy Reviews* **16**, 3024-3033 (2012).

8 Lu, X. *et al.* A sea-change: manganese doped nickel/nickel oxide electrocatalysts for hydrogen generation from seawater. *Energy & Environmental Science* **11**, 1898-1910, doi:10.1039/C8EE00976G (2018).

9 Zhang, W. *et al.* Single-crystalline (FexNi1-x) 2P nanosheets with dominant {011^{-} 1^{-}} facets: Efficient electrocatalysts for hydrogen evolution reaction at all pH values. *Nano Energy* **56**, 813-822 (2019).

10 Murthy, A. P., Govindarajan, D., Theerthagiri, J., Madhavan, J. & Parasuraman, K. Metal-doped molybdenum nitride films for enhanced hydrogen evolution in near-neutral strongly buffered aerobic media. *Electrochimica Acta* **283**, 1525-1533 (2018).

11 Ďurovič, M., Hnát, J. & Bouzek, K. Electrocatalysts for the hydrogen evolution reaction in alkaline and neutral media. A comparative review. *Journal of Power Sources* **493**, 229708 (2021).

12 Shinagawa, T. & Takanabe, K. New Insight into the Hydrogen Evolution Reaction under Buffered Near-Neutral pH Conditions: Enthalpy and Entropy of Activation. *The Journal of Physical Chemistry C* **120**, 24187-24196, doi:10.1021/acs.jpcc.6b07954 (2016).

13 Zhou, Z. *et al.* Electrocatalytic hydrogen evolution under neutral pH conditions: current understandings, recent advances, and future prospects. *Energy & Environmental Science* **13**, 3185-3206 (2020).

14 Shinagawa, T., Garcia-Esparza, A. T. & Takanabe, K. Mechanistic switching by hydronium ion activity for hydrogen evolution and oxidation over polycrystalline platinum disk and platinum/carbon electrodes. *ChemElectroChem* **1**, 1497-1507 (2014).

15 Shinagawa, T. & Takanabe, K. Towards versatile and sustainable hydrogen production through electrocatalytic water splitting: electrolyte engineering. *ChemSusChem* **10**, 1318 (2017).

16 Shinagawa, T. & Takanabe, K. Electrocatalytic hydrogen evolution under densely buffered neutral pH conditions. *The Journal of Physical Chemistry C* **119**, 20453-20458 (2015).

17 Katsounaros, I. *et al.* The effective surface pH during reactions at the solid–liquid interface. *Electrochemistry communications* **13**, 634-637 (2011).

18 Shinagawa, T. & Takanabe, K. Electrolyte engineering toward efficient hydrogen production electrocatalysis with oxygen-crossover regulation under densely buffered near-neutral pH conditions. *The Journal of Physical Chemistry C* **120**, 1785-1794 (2016).

19 Lazouski, N., Schiffer, Z. J., Williams, K. & Manthiram, K. Understanding continuous lithium-mediated electrochemical nitrogen reduction. *Joule* **3**, 1127-1139 (2019).

20 Lazouski, N., Chung, M., Williams, K., Gala, M. L. & Manthiram, K. Non-aqueous gas diffusion electrodes for rapid ammonia synthesis from nitrogen and water-splitting-derived hydrogen. *Nature Catalysis* **3**, 463-469, doi:10.1038/s41929-020-0455-8 (2020).

21 Resasco, J., Lum, Y., Clark, E., Zeledon, J. Z. & Bell, A. T. Effects of Anion Identity and Concentration on Electrochemical Reduction of CO2. *ChemElectroChem* **5**, 1064-1072, doi:10.1002/celc.201701316 (2018).

22 Liu, X. *et al.* Understanding trends in electrochemical carbon dioxide reduction rates. *Nature communications* **8**, 1-7 (2017).

23 Skulason, E. *et al.* A theoretical evaluation of possible transition metal electro-catalysts for N_2 reduction. *Physical Chemistry Chemical Physics* **14**, 1235-1245, doi:10.1039/c1cp22271f (2012).

24 Singh, M. R., Kwon, Y., Lum, Y., Ager Iii, J. W. & Bell, A. T. Hydrolysis of electrolyte cations enhances the electrochemical reduction of CO2 over Ag and Cu. *Journal of the American chemical society* **138**, 13006-13012 (2016).

25 Singh, A. R. *et al.* Electrochemical Ammonia Synthesis-The Selectivity Challenge. *Acs Catalysis* **7**, 706-709, doi:10.1021/acscatal.6b03035 (2017).

26 Resasco, J. *et al.* Promoter Effects of Alkali Metal Cations on the Electrochemical Reduction of Carbon Dioxide. *Journal of the American Chemical Society* **139**, 11277-11287, doi:10.1021/jacs.7b06765 (2017).

27 Gunathunge, C. M., Ovalle, V. J. & Waegele, M. M. Probing promoting effects of alkali cations on the reduction of CO at the aqueous electrolyte/copper interface. *Physical Chemistry Chemical Physics* **19**, 30166-30172, doi:10.1039/C7CP06087D (2017).

28 Zhang, Y., Gao, L., Hensen, E. J. M. & Hofmann, J. P. Evaluating the Stability of Co2P Electrocatalysts in the Hydrogen Evolution Reaction for Both Acidic and Alkaline Electrolytes. *ACS Energy Letters* **3**, 1360-1365, doi:10.1021/acsenergylett.8b00514 (2018).

29 Hu, L. *et al.* Ambient electrochemical ammonia synthesis with high selectivity on Fe/Fe oxide catalyst. *ACS Catal* **8**, 9312-9319 (2018).

30 Waegele, M. M., Gunathunge, C. M., Li, J. & Li, X. How cations affect the electric double layer and the rates and selectivity of electrocatalytic processes. *The Journal of chemical physics* **151**, 160902 (2019).

31 Bakovic, S. I. P. *et al.* Electrochemically active surface area controls HER activity for FexNi100− x films in alkaline electrolyte. *Journal of Catalysis* **394**, 104-112 (2021).

32 Soares, D. M., Teschke, O. & Torriani, I. Hydride effect on the kinetics of the hydrogen evolution reaction on nickel cathodes in alkaline media. *Journal of The Electrochemical Society* **139**, 98 (1992).

33 Mauer, A. E., Kirk, D. W. & Thorpe, S. J. The role of iron in the prevention of nickel electrode deactivation in alkaline electrolysis. *Electrochim. Acta* **52**, 3505-3509 (2007).

34 Auinger, M. *et al.* Near-surface ion distribution and buffer effects during electrochemical reactions. *Physical Chemistry Chemical Physics* **13**, 16384-16394 (2011).

35 Da Silva, S., Basséguy, R. & Bergel, A. Electrochemical deprotonation of phosphate on stainless steel. *Electrochimica Acta* **49**, 4553-4561 (2004).

36 Munoz, L. D. S., Bergel, A., Féron, D. & Basséguy, R. Hydrogen production by electrolysis of a phosphate solution on a stainless steel cathode. *International Journal of Hydrogen Energy* **35**, 8561-8568 (2010).

37 Bard, A. J. & Faulkner, L. R. Fundamentals and applications. *Electrochemical methods* **2**, 580-632 (2001).

38 Ilic, E., Pardo, A., Hauert, R., Schmutz, P. & Mischler, S. Silicon corrosion in neutral media: the influence of confined geometries and crevice corrosion in simulated physiological solutions. *Journal of The Electrochemical Society* **166**, C125 (2019).

39 Biesinger, M. C. *et al.* Resolving surface chemical states in XPS analysis of first row transition metals, oxides and hydroxides: Cr, Mn, Fe, Co and Ni. *Applied Surface Science* **257**, 2717-2730, doi:https://doi.org/10.1016/j.apsusc.2010.10.051 (2011).

40 Temesghen, W. & Sherwood, P. Analytical utility of valence band X-ray photoelectron spectroscopy of iron and its oxides, with spectral interpretation by cluster and band structure calculations. *Analytical and bioanalytical chemistry* **373**, 601-608 (2002).

41 Grosvenor, A. P., Biesinger, M. C., Smart, R. S. C. & McIntyre, N. S. New interpretations of XPS spectra of nickel metal and oxides. *Surface Science* **600**, 1771-1779 (2006).

42 Biesinger, M. C., Lau, L. W. M., Gerson, A. R. & Smart, R. S. C. The role of the Auger parameter in XPS studies of nickel metal, halides and oxides. *Physical Chemistry Chemical Physics* **14**, 2434-2442 (2012).

43 Biesinger, M. C., Payne, B. P., Lau, L. W. M., Gerson, A. & Smart, R. S. C. X-ray photoelectron spectroscopic chemical state quantification of mixed nickel metal, oxide and hydroxide systems. *Surface and Interface Analysis: An International Journal devoted to the development and application of techniques for the analysis of surfaces, interfaces and thin films* **41**, 324-332 (2009).

44 Huang, L. F., Hutchison, M. J., Santucci Jr, R. J., Scully, J. R. & Rondinelli, J. M. Improved electrochemical phase diagrams from theory and experiment: the Ni–water system and its complex compounds. *The Journal of Physical Chemistry C* **121**, 9782-9789 (2017).

45 Huang, L.-F. & Rondinelli, J. M. Reliable electrochemical phase diagrams of magnetic transition metals and related compounds from high-throughput ab initio calculations. *npj Materials Degradation* **3**, 1-13 (2019).

46 Beverskog, B. & Puigdomenech, I. Revised pourbaix diagrams for iron at 25–300 C. *Corrosion Science* **38**, 2121-2135 (1996).

47 Virtanen, S., Schmuki, P., Büchler, M. & Isaacs, H. S. Electrochemical Behavior of Fe in Phosphate Solutions Studied by In Situ X-Ray Absorption Near Edge Structure. *Journal of the Electrochemical Society* **146**, 4087 (1999).

48 Yao, S. *et al.* From an Fe 2 P 3 complex to FeP nanoparticles as efficient electrocatalysts for water-splitting. *Chemical science* **9**, 8590-8597 (2018).

49 Zhang, B., Zhang, J., Tang, X., Lui, Y. H. & Hu, S. An investigation of Fe incorporation on the activity and stability of homogeneous (FexNi1-x) 2P solid solutions as electrocatalysts for alkaline hydrogen evolution. *Electrochimica Acta* **294**, 297-303 (2019).

50 Zhang, B. *et al.* Hierarchical FeNiP@ ultrathin carbon nanoflakes as alkaline oxygen evolution and acidic hydrogen evolution catalyst for efficient water electrolysis and organic decomposition. *ACS applied materials & interfaces* **10**, 8739-8748 (2018).

51 Qian, M., Cui, S., Jiang, D., Zhang, L. & Du, P. Highly Efficient and Stable Water-Oxidation Electrocatalysis with a Very Low Overpotential using FeNiP Substitutional-Solid-Solution Nanoplate Arrays. *Advanced materials* **29**, 1704075 (2017).

52 Yoon, S., Kim, J., Lim, J.-H. & Yoo, B. Cobalt iron-phosphorus synthesized by electrodeposition as highly active and stable bifunctional catalyst for full water splitting. *Journal of The Electrochemical Society* **165**, H271 (2018).

53 Li, X., Zha, Q. & Ni, Y. Ni–Fe Phosphate/Ni Foam Electrode: Facile Hydrothermal Synthesis and Ultralong Oxygen Evolution Reaction Durability. *ACS Sustainable Chemistry & Engineering* **7**, 18332-18340 (2019).

54 Menezes, P. W. *et al.* A structurally versatile nickel phosphite acting as a robust bifunctional electrocatalyst for overall water splitting. *Energy & Environmental Science* **11**, 1287-1298 (2018).

55 Shimizu, M., Tsushima, Y. & Arai, S. Electrochemical Na-insertion/extraction property of Ni-coated black phosphorus prepared by an electroless deposition method. *ACS Omega* **2**, 4306-4315 (2017).

56 Khalate, S. A. *et al.* Hydrothermally synthesized Iron Phosphate Hydroxide thin film electrocatalyst for electrochemical water splitting. *Electrochimica Acta* **319**, 118-128 (2019).

57 Wu, X. *et al.* Engineering multifunctional collaborative catalytic interface enabling efficient hydrogen evolution in all pH range and seawater. *Advanced Energy Materials* **9**, 1901333 (2019).

5. Chapter 5. Conclusions and Future Research Directions

5.1 Conclusions

Iron-nickel oxide based electrodes were developed as a platform to study the electrochemical hydrogen evolution reaction of transition metal-based catalysts. A variety of electrochemical methods including linear sweep voltammetry, chronoamperometry, chronopotentiometry, cyclic voltammetry, open circuit potential, and electrochemical impedance spectroscopy provided an understanding of electrochemical activity of different electrode-electrolytes studied. X-ray photoelectron spectroscopy and hydrogen production monitoring provided additional complementary information to further understand the electrode-electrolyte interactions and the overall hydrogen evolution reaction.

5.2 Future Research Directions

The work presented herein opens the path for further studies in a variety of research areas. The work done in the development of bimetallic electrodes can be further expanded to either incorporate additional transition metals such as cobalt and/or the incorporation of non-transition metals such as phosphorous to evaluate their electrochemical activity and stability in different electrode-electrolyte conditions.[1] The work on the use of the $Fe_xNi_{100-x}O_y$/Si serves to demonstrate how hydrogen production can be boosted through the electrode design and the dependence on the electrolyte. This provides the opportunity to design catalysts[2] and systems[3] for the generation of hydrogen.[4] Life cycle assessment and techno economic studies must be performed in conjunction with the design of these combined self-consuming and electrocatalyst systems to produce hydrogen. The characterization of electrodes post-electrocatalysis sheds light on the interactions between the electrolyte components and electrode. Thus, this research provides the initial understanding for the application of more advanced characterization

techniques such as in-situ ambient-pressure XPS.[5] The HER studies performed in neutral buffered conditions provide additional evidence to the community to build upon to further understand the reaction in neutral buffered conditions and understand the electrode-electrolyte interactions. The HER studies performed in neutral buffered condition provide the basis to further study on the enhancement and suppression of HER through the design of neutral buffered electrolytes.[6]

References

1 Lu, Z.-p. & Sepunaru, L. Electrodeposition of iron phosphide film for hydrogen evolution reaction. *Electrochimica Acta* **363**, 137167 (2020).

2 He, Y. *et al.* Discovery and Facile Synthesis of a New Silicon Based Family as Efficient Hydrogen Evolution Reaction Catalysts: A Computational and Experimental Investigation of Metal Monosilicides. *Small* **17**, 2006153 (2021).

3 Erogbogbo, F. *et al.* On-demand hydrogen generation using nanosilicon: splitting water without light, heat, or electricity. *Nano letters* **13**, 451-456 (2013).

4 Zhu, L. *et al.* A rhodium/silicon co-electrocatalyst design concept to surpass platinum hydrogen evolution activity at high overpotentials. *Nature communications* **7**, 1-7 (2016).

5 Stoerzinger, K. A., Hong, W. T., Crumlin, E. J., Bluhm, H. & Shao-Horn, Y. Insights into electrochemical reactions from ambient pressure photoelectron spectroscopy. *Accounts of chemical research* **48**, 2976-2983 (2015).

6 Zhou, Z. *et al.* Electrocatalytic hydrogen evolution under neutral pH conditions: current understandings, recent advances, and future prospects. *Energy & Environmental Science* **13**, 3185-3206 (2020).

Appendices

Appendix 1. Supplementary information for Electrochemically Active Surface Area Controls HER Activity for Fe_xNi_{100-x} Films in Alkaline Electrolyte

Table S2.1. Electrodeposition solution composition.

Film Ratio (Fe_xNi_{100-x})	Mass (g) $FeSO_4$ $7H_2O$	Mass (g) $NiSO_4$ $6H_2O$	Mass (g) H_3BO_3
$Fe_{100}Ni_0$	4.1703	0	0.92745
$Fe_{80}Ni_{20}$	3.47525	0.657125	0.92745
$Fe_{50}Ni_{50}$	2.08515	1.971375	0.92745
$Fe_{20}Ni_{80}$	0.69505	3.285625	0.92745
Fe_0Ni_{100}	0	3.94275	0.92745

Table S2.2. Mass electrodeposited obtained by QCM-D.

Film	QCM-D Mass ($\mu g/cm^2$)
$Fe_{100}Ni_0$	67 (±3)
$Fe_{80}Ni_{20}$	31 (±1)
$Fe_{50}Ni_{50}$	64 (±3)
$Fe_{20}Ni_{80}$	56 (±1)
Fe_0Ni_{100}	54 (±4)

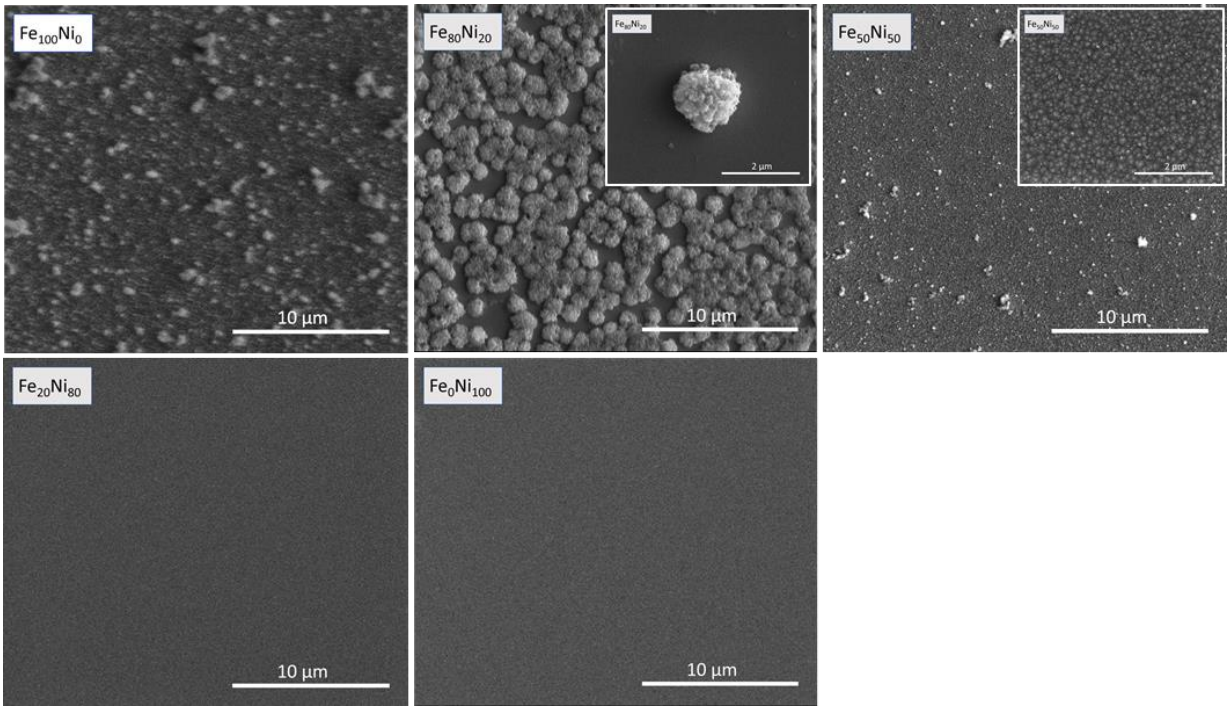

Fig. S2.1. Top-down SEM images of different Fe_xNi_{100-x} electrodeposited surfaces.

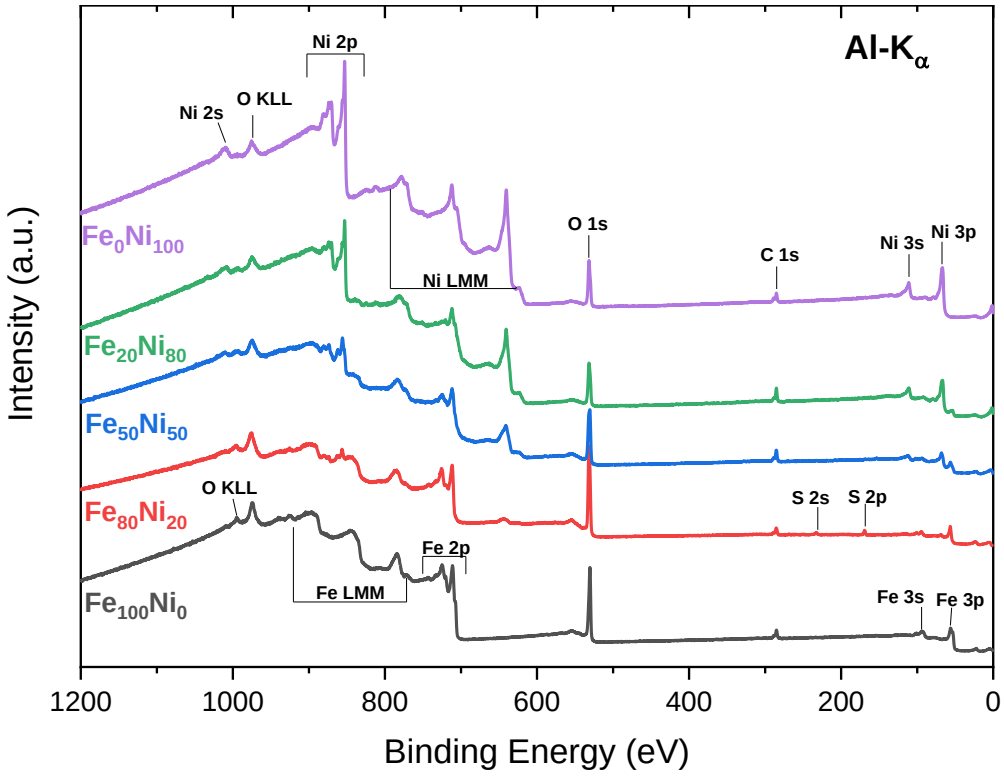

Fig. S2.2. XPS survey spectrum for all Fe_xNi_{100-x} ratios synthesized.

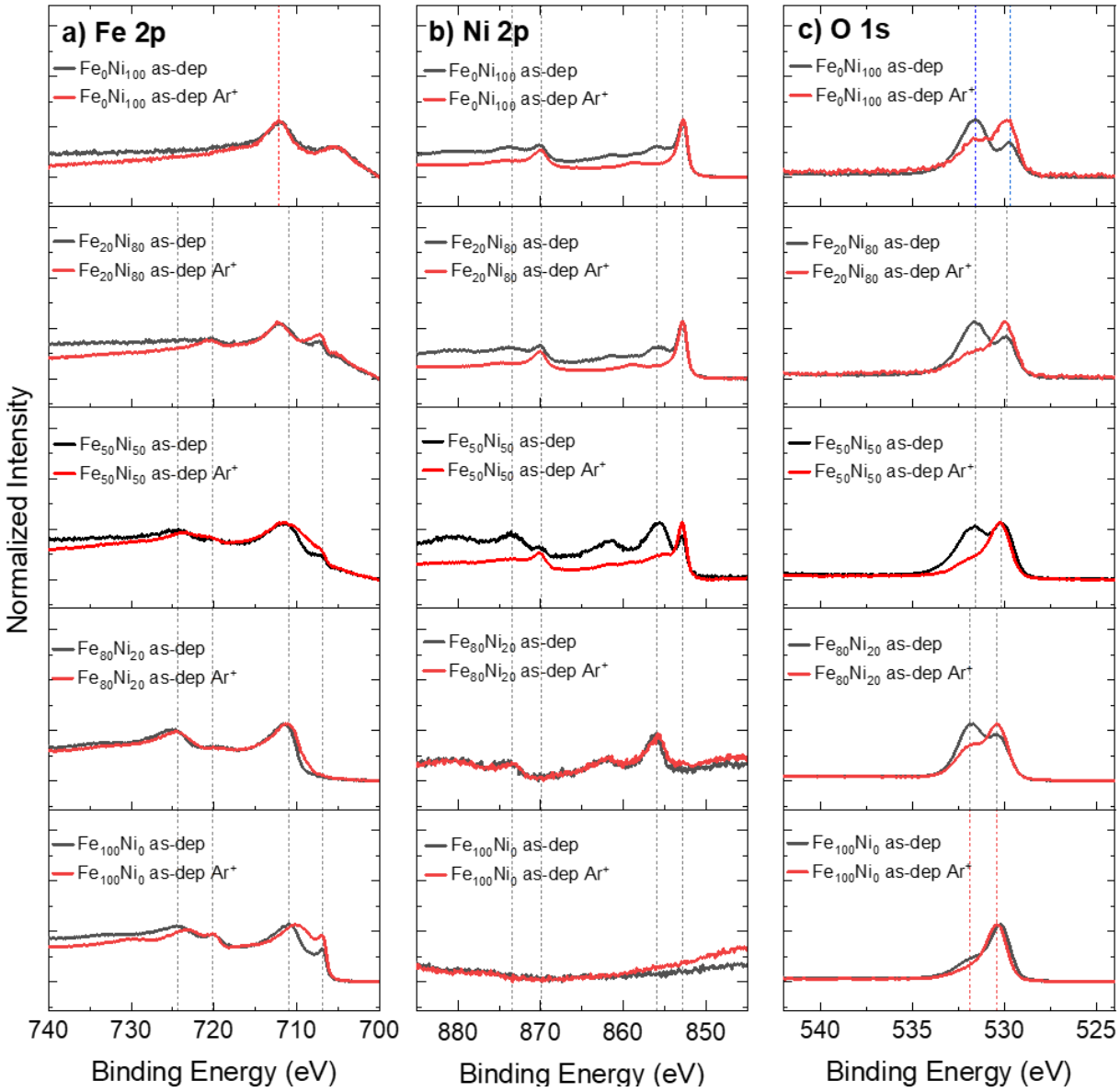

Fig. S2.3. XPS spectra of as-deposited vs. Argon sputtered samples a) Fe 2p b) Ni 2p c) O 1s.

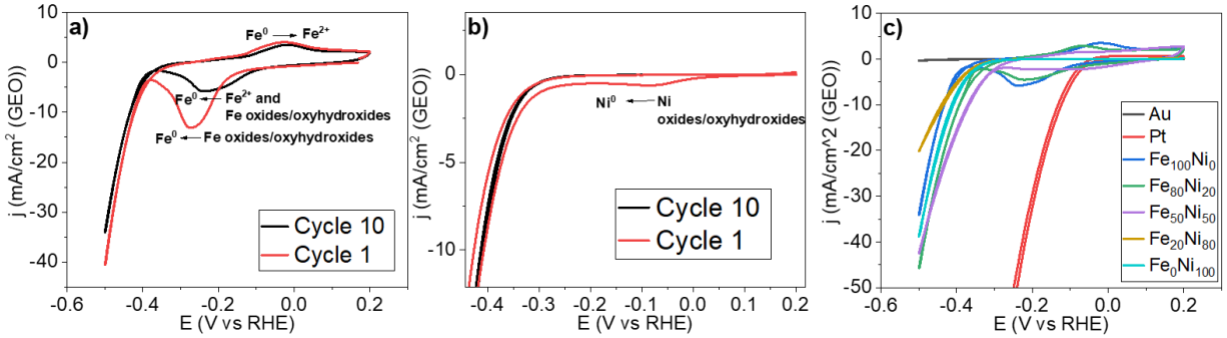

Fig. S2.4. Cyclic voltammograms performed at 50 mV/sec in 1M NaOH (pH=12), a) $Fe_{100}Ni_0$ CV number 1 and 10, b) Fe_0Ni_{100} CV number 1 and 10, and c) stabilized surfaces after 10 cycles.

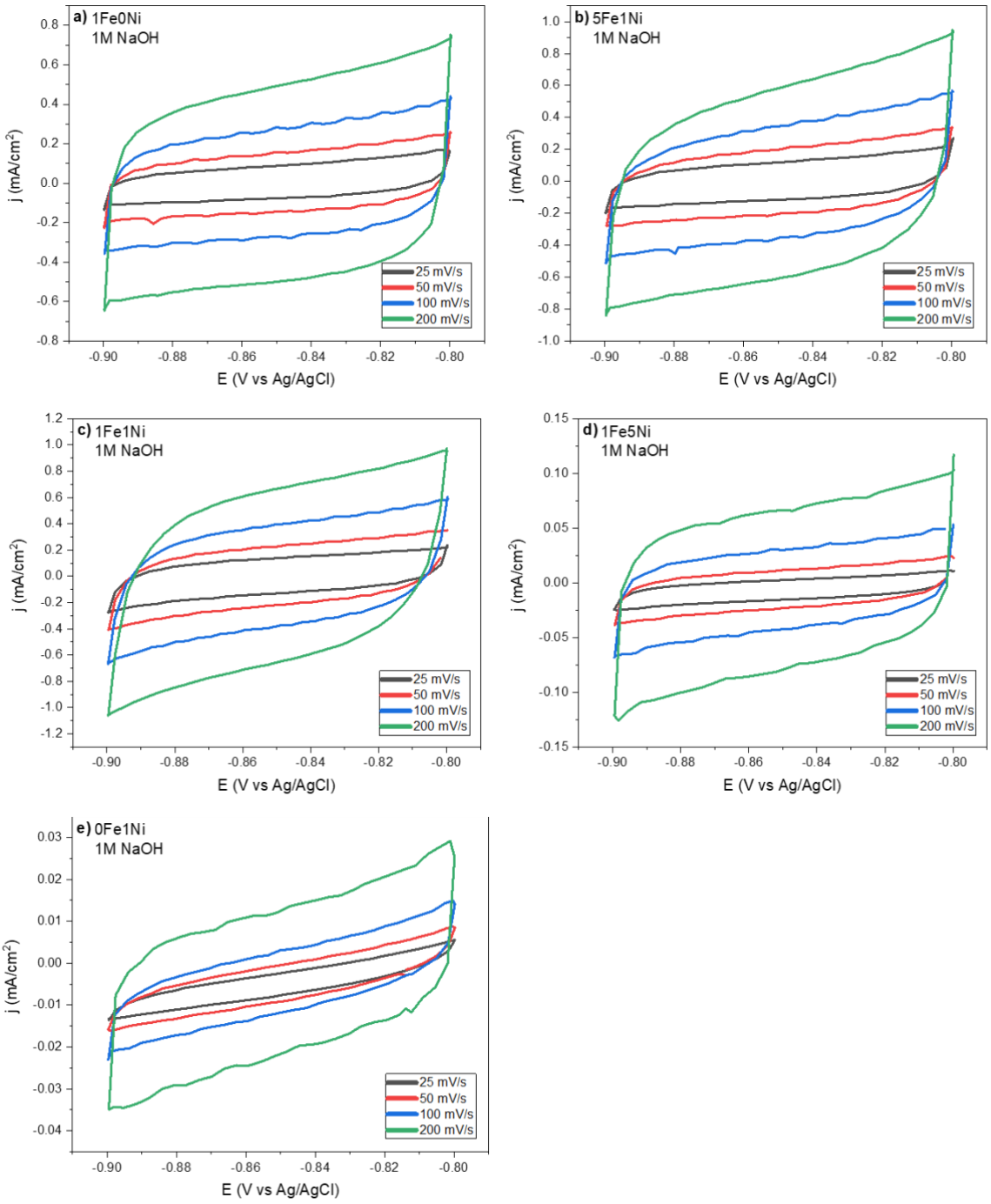

Fig. S2.5. Cyclic voltammograms of a) 1Fe0Ni b) 5Fe1Ni c)1Fe1Ni d) 1Fe5Ni e) 0Fe1Ni used to determine the electrochemical double-layer capacitance (C_{dl}) and estimate the electrochemically active surface area (ECSA). CV were performed on between -1.05 V and -0.95 V vs Ag/AgCl at different scan rates.

Table S2.5. Estimated electrochemically active surface area for different Fe_xNi_{100-x} catalysts in alkaline media (1M NaOH at pH 12).

Catalyst	Estimated ECSA (cm^2) (0.04 mF/cm^2)
$Fe_{100}Ni_0$	59
$Fe_{80}Ni_{20}$	67
$Fe_{50}Ni_{50}$	74
$Fe_{20}Ni_{80}$	9
Fe_0Ni_{100}	2

Table S2.6. Electrochemical current density (GEO and ECSA) normalized evaluation.

Catalyst	j(mA/cm^2) GEO @ (-0.5 V vs HRE)	j(mA/cm^2) ECSA @ (-0.5 V vs HRE)
$Fe_{100}Ni_0$	-30.51	-0.52
$Fe_{80}Ni_{20}$	-36.13	-0.54
$Fe_{50}Ni_{50}$	-34.70	-0.47
$Fe_{20}Ni_{80}$	-21.48	-2.38
Fe_0Ni_{100}	-35.69	-17.84

Table S2.7. Electrochemical impedance parameters obtained from fitting Nyquist plot data with the equivalent circuit.

Catalyst	C_{dl} ($F\ cm^{-2}$)	R_{CT} (Ohm cm^{-2})	τ (s)
$Fe_{100}Ni_0$	1.97E-03	332.4	6.56E-01
$Fe_{80}Ni_{20}$	2.15E-03	118.5	2.54E-01
$Fe_{50}Ni_{50}$	2.22E-03	77.3	1.72E-01
$Fe_{20}Ni_{80}$	1.06E-04	161.3	1.71E-02
Fe_0Ni_{100}	7.84E-05	56.1	4.39E-03

Appendix 2. Supplementary information for Electrochemical activation of silicon: Enhancing hydrogen production from FeNi electrocatalysts

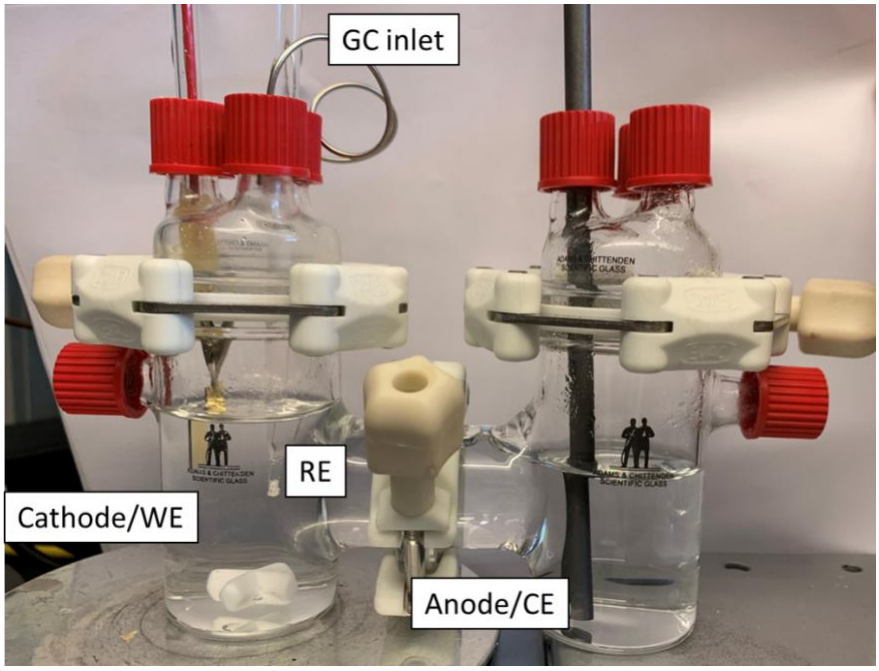

Fig. S3.1: Three-electrode gas tight H-cell used in all the experiments.

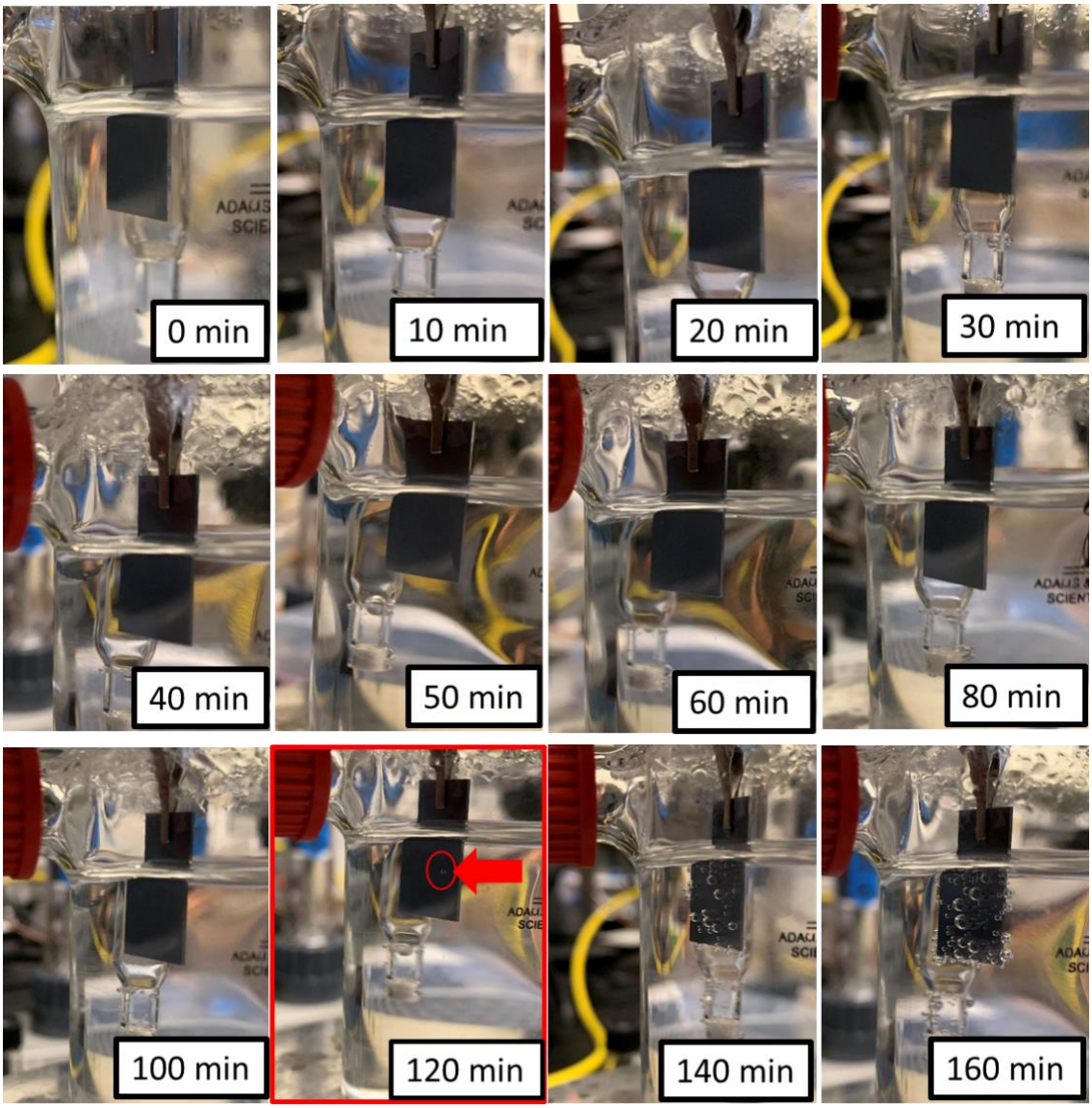

Fig. S3.2: Pictures were taken of the Au/Si showing the Si side in NaOH. The activation of Si and production of bubbles is observed where an Au/Si wafer was immersed in 0.1M NaOH solution in a gas-tight three-electrode H-cell at room temperature. The H_2 production is observed to start at 120 min.

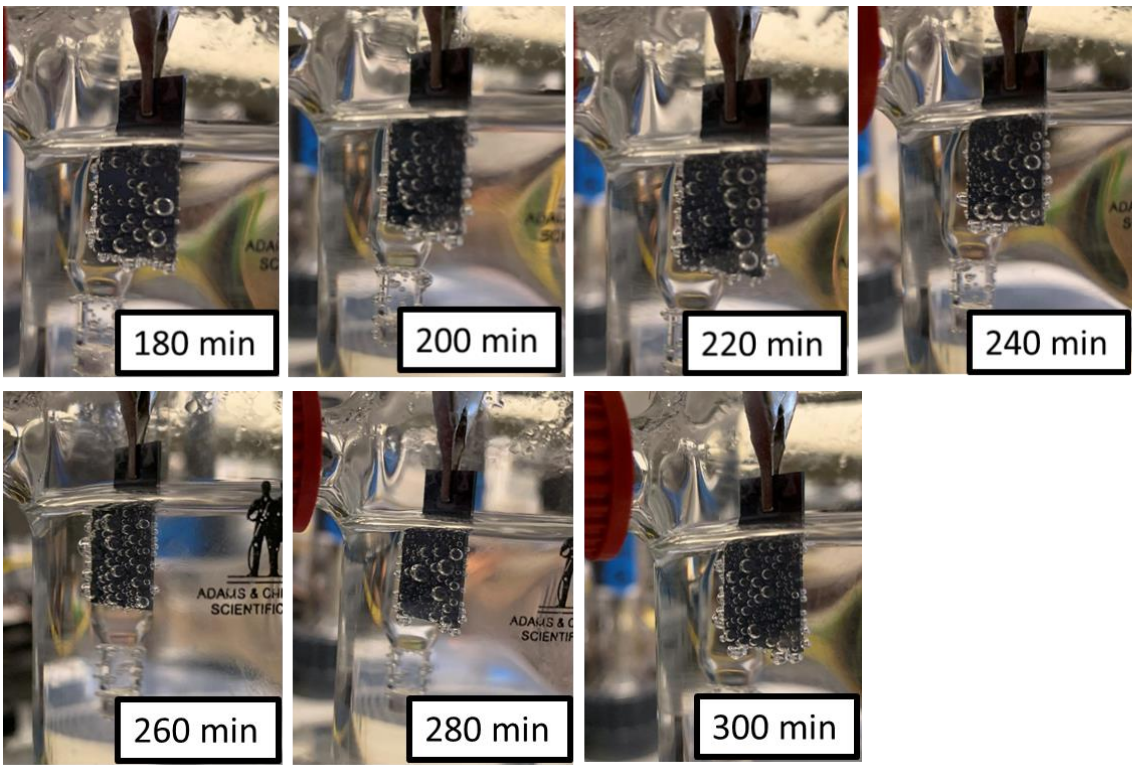

Fig. S3.2: Cont.

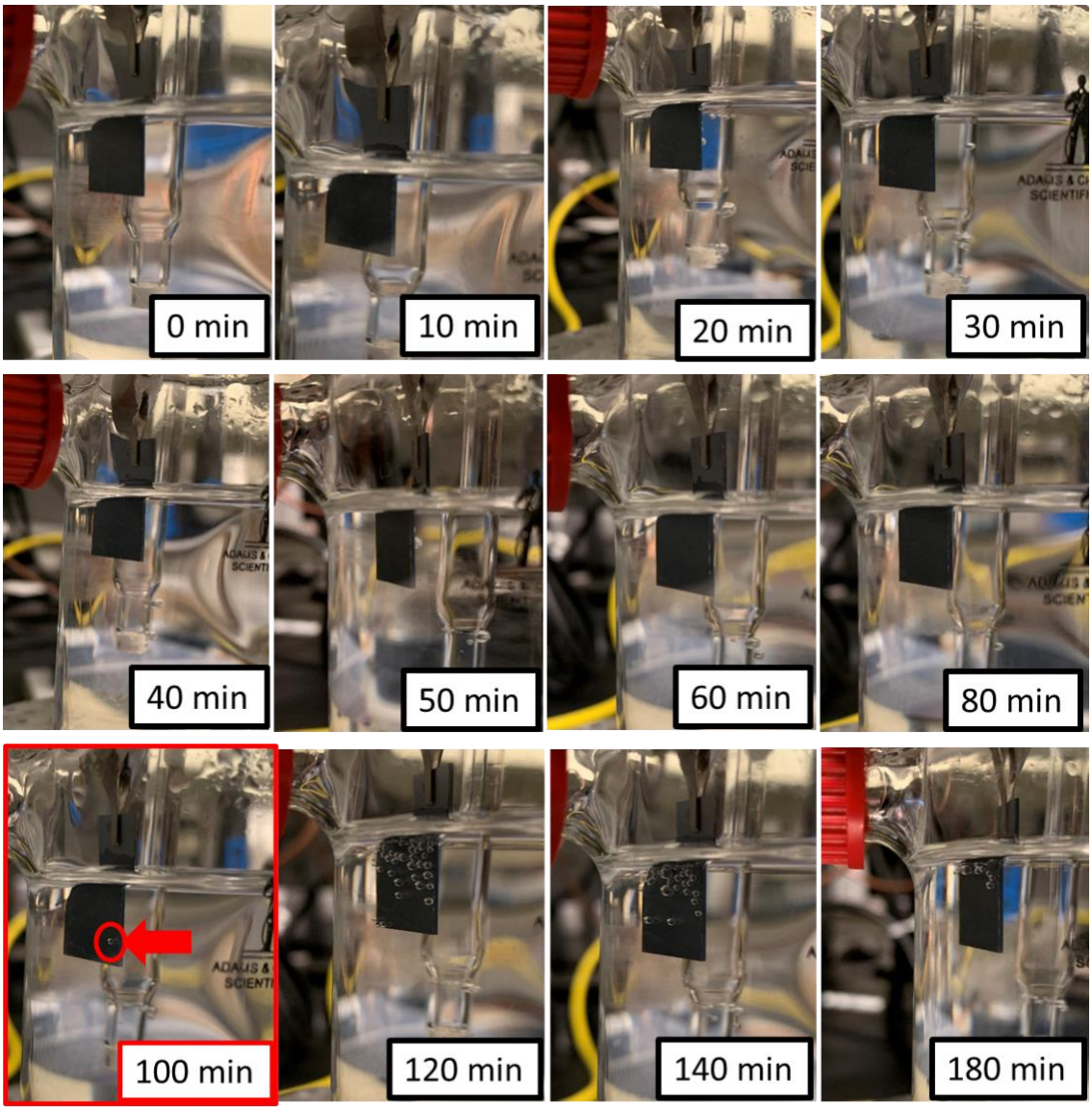

Fig. S3.3: Pictures were taken of the Au/Si showing the Si side in KOH. The activation of Si and production of bubbles is observed where an Au/Si wafer was immersed in 0.1M KOH solution in a gas-tight three-electrode H-cell at room temperature. The H_2 production is observed to start at 100 min.

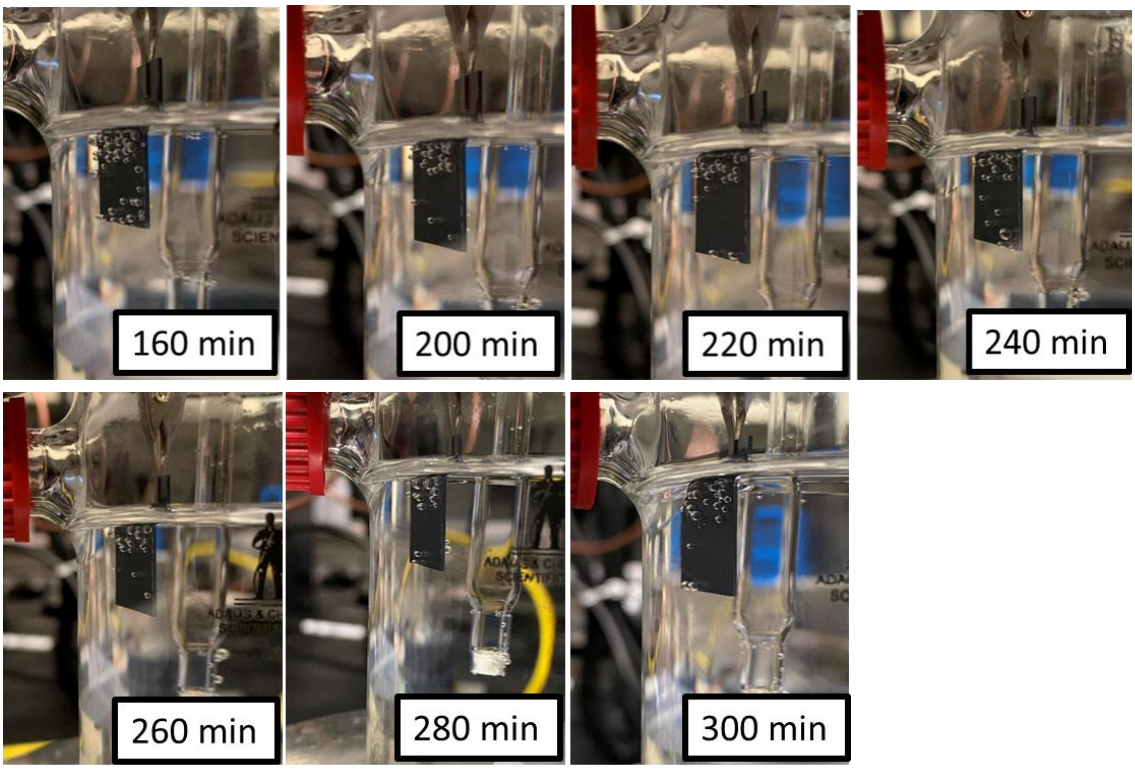

Fig. S3.3: Cont.

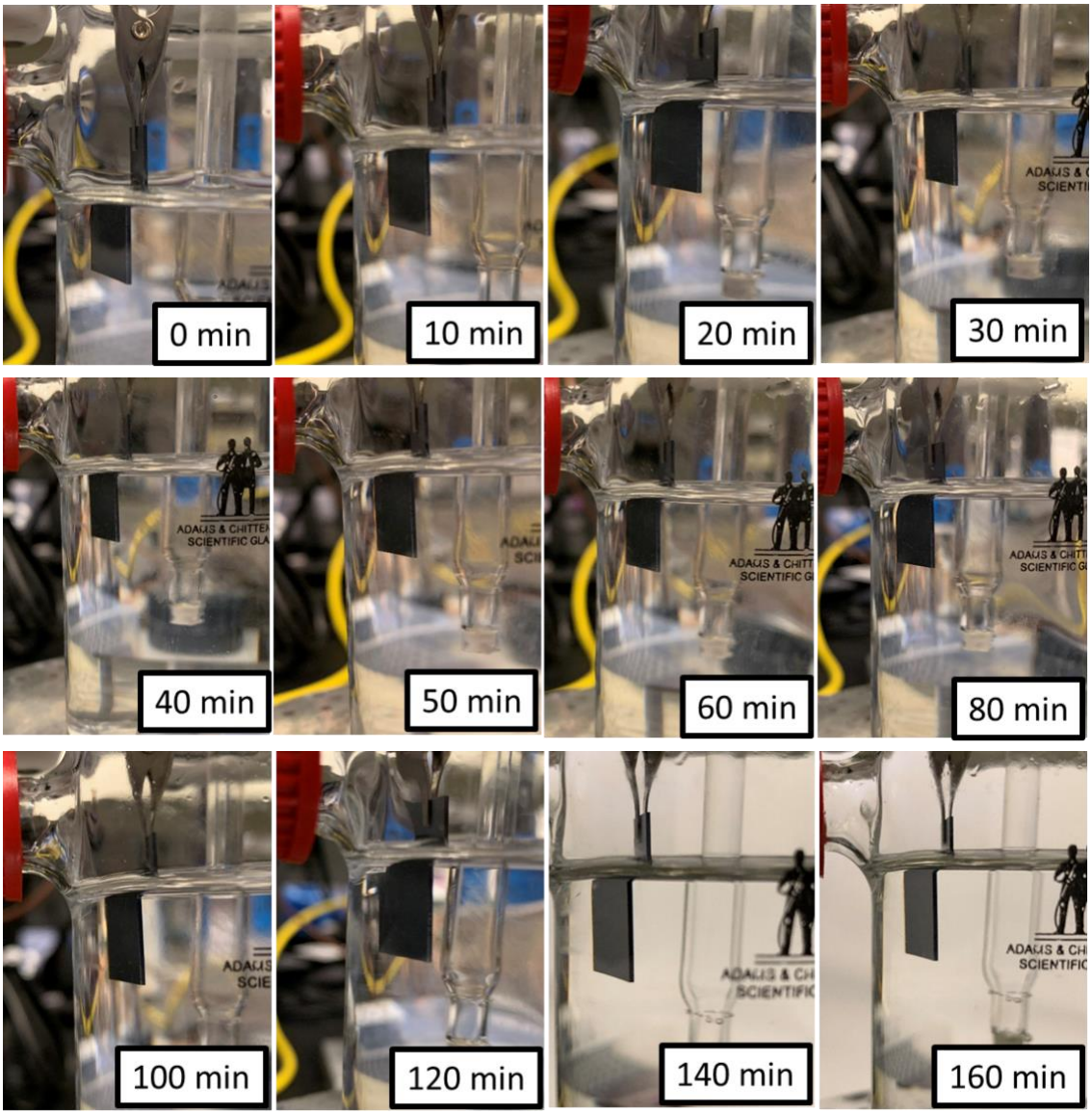

Fig. S3.4: Pictures were taken of the Au/Si showing the Si side in LiOH. The activation of Si and production of bubbles is observed where an Au/Si wafer was immersed in 0.1M LiOH solution in a gas-tight three-electrode H-cell at room temperature. The H_2 production is observed to start at 300 min.

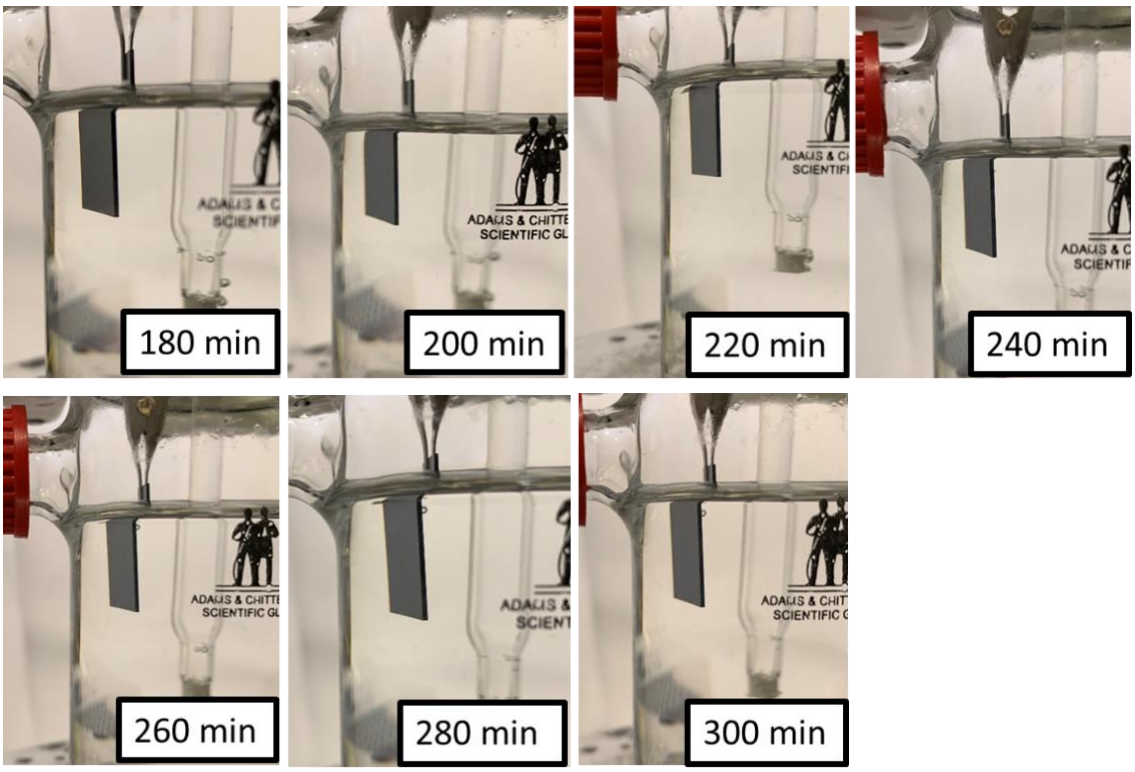

Fig. S3.4: Cont.

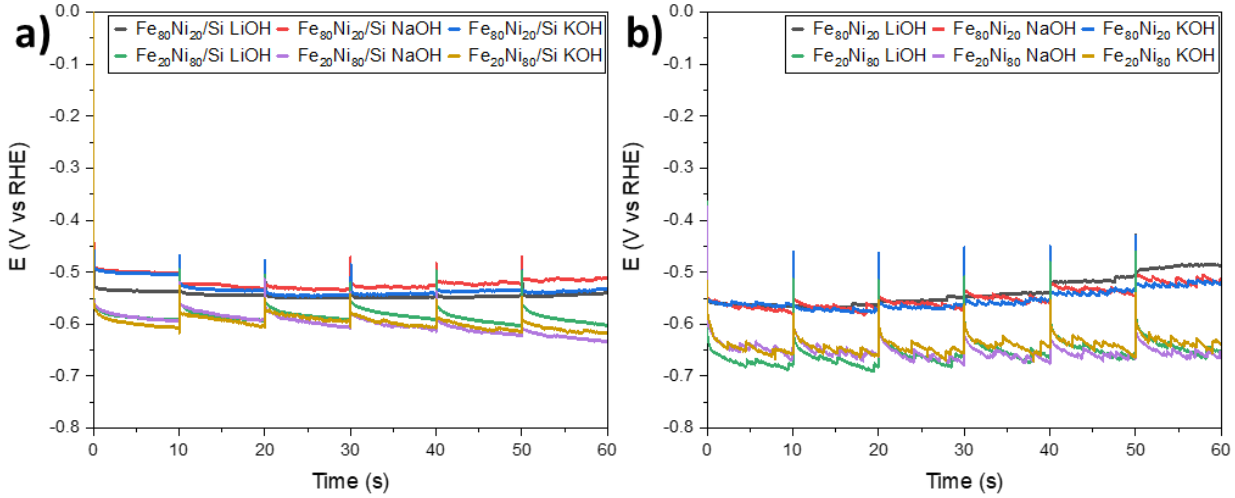

Fig. S3.5: Chronopotentiometry (CP) held at -10 mA for a) $Fe_{20}Ni_{80}$/Si and $Fe_{80}Ni_{20}$/Si and b) $Fe_{20}Ni_{80}$ and $Fe_{80}Ni_{20}$ evaluated in 0.1M LiOH, NaOH, and KOH electrolyte solutions.

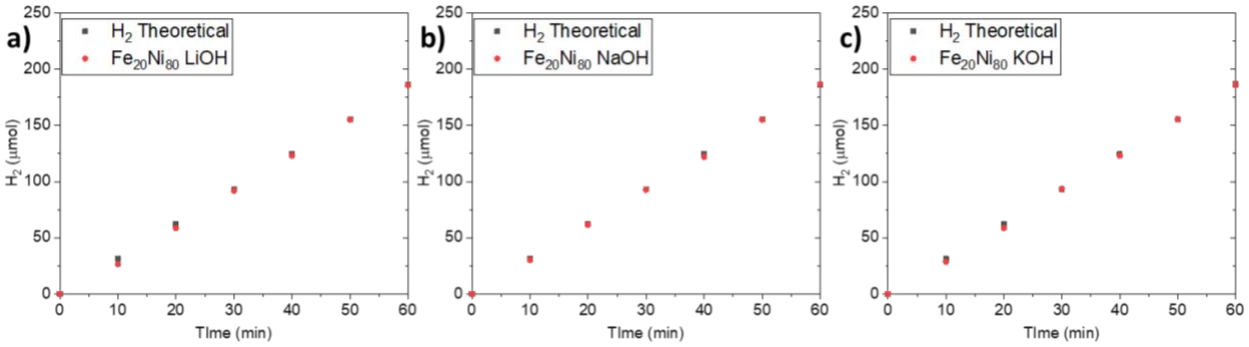

Fig. S3.6: Hydrogen quantification of $Fe_{20}Ni_{80}$ film in different electrolytes a) LiOH, b) NaOH, and c) KOH.

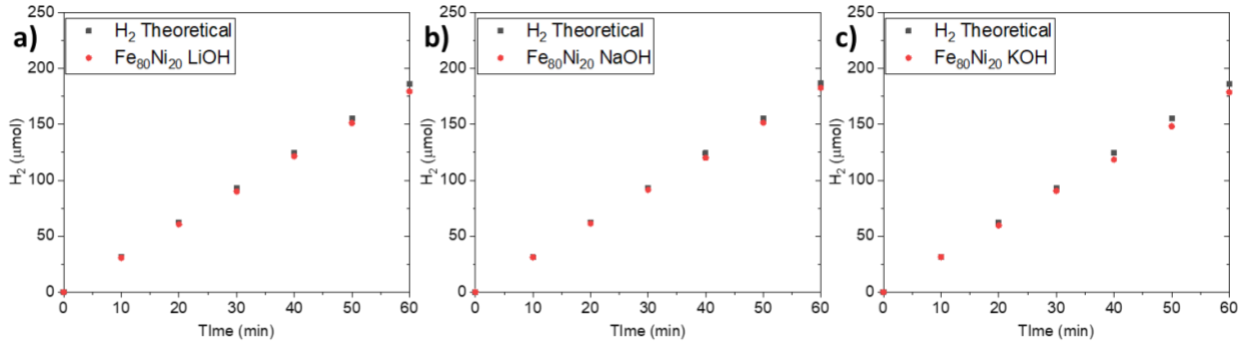

Fig. S3.7: Hydrogen quantification of $Fe_{80}Ni_{20}$ film in different electrolytes a) LiOH, b) NaOH, and c) KOH.

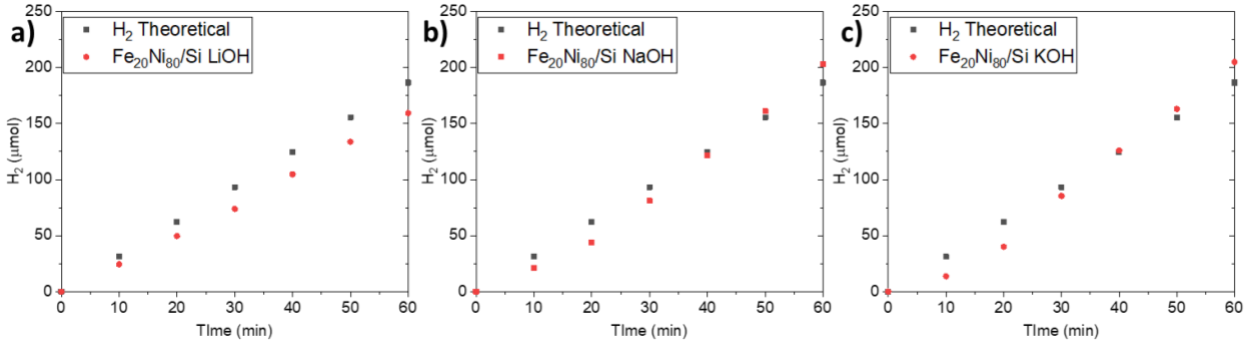

Fig. S8: Hydrogen quantification of $Fe_{20}Ni_{80}$/Si film in different electrolytes a) LiOH, b) NaOH, and c) KOH

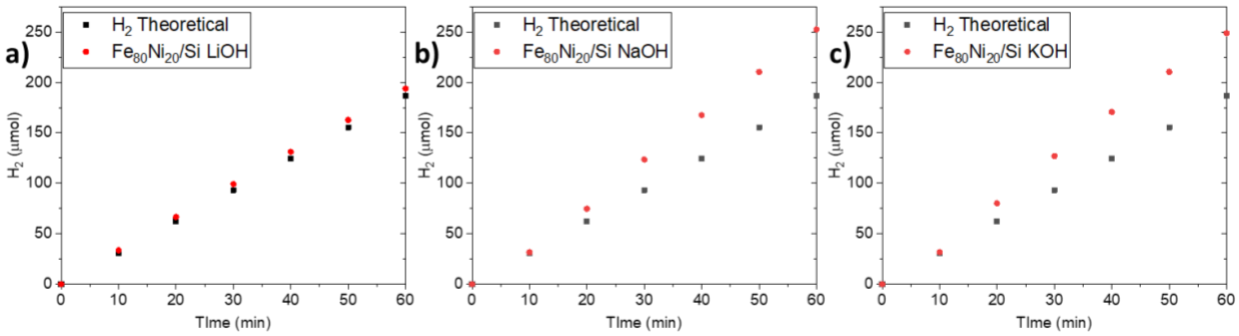

Fig. S3.9: Hydrogen quantification of $Fe_{80}Ni_{20}$/Si film in different electrolytes a) LiOH, b) NaOH, and c) KOH.

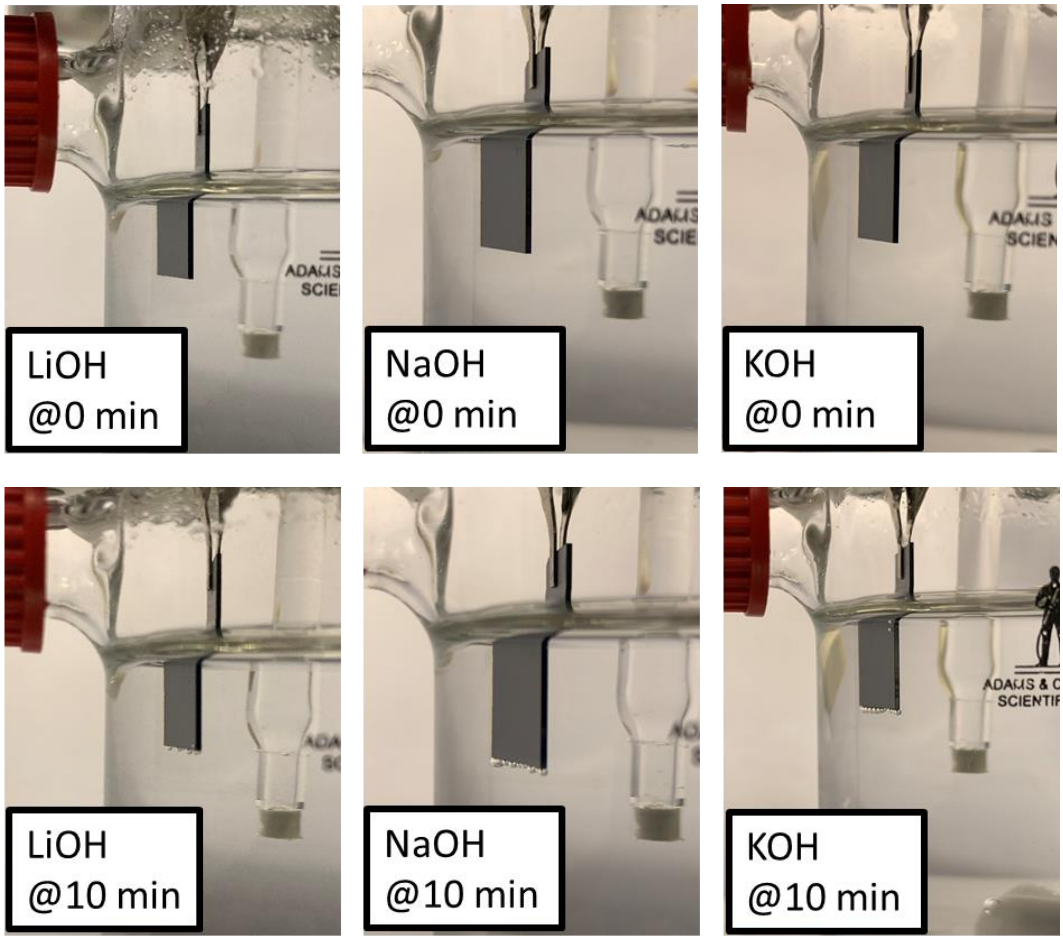

Fig. S3.10: Pictures taken of the Si side when evaluating the $Fe_{80}Ni_{20}$/Si in LiOH, NaOH, and KOH. Except for the picture at 0 min all pictures were taken after a 10 min interval of holding the current density at 10 mA cm^{-2} but before the solution was agitated and the H_2 was measured.

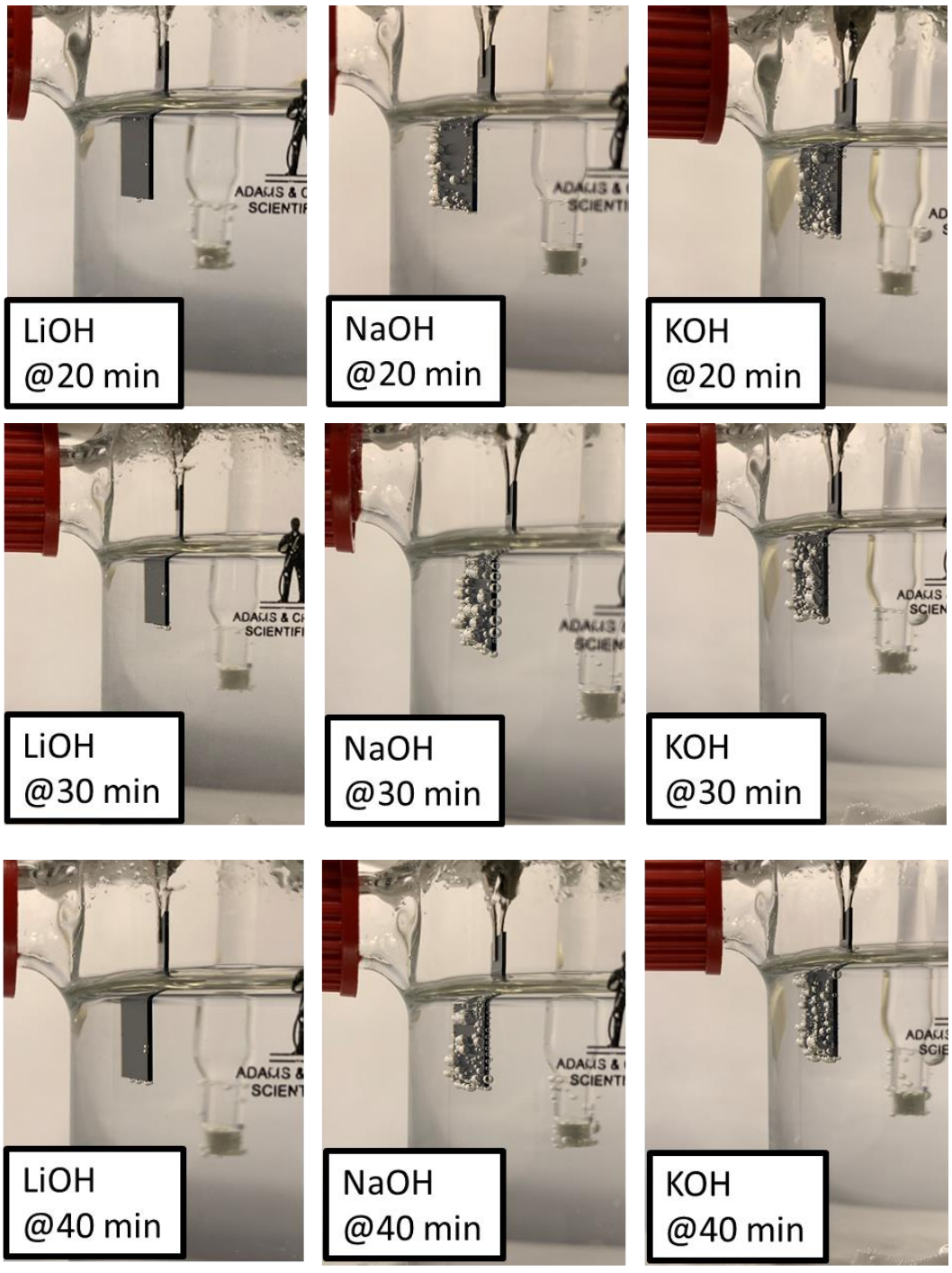

Fig. S3.10: Cont.

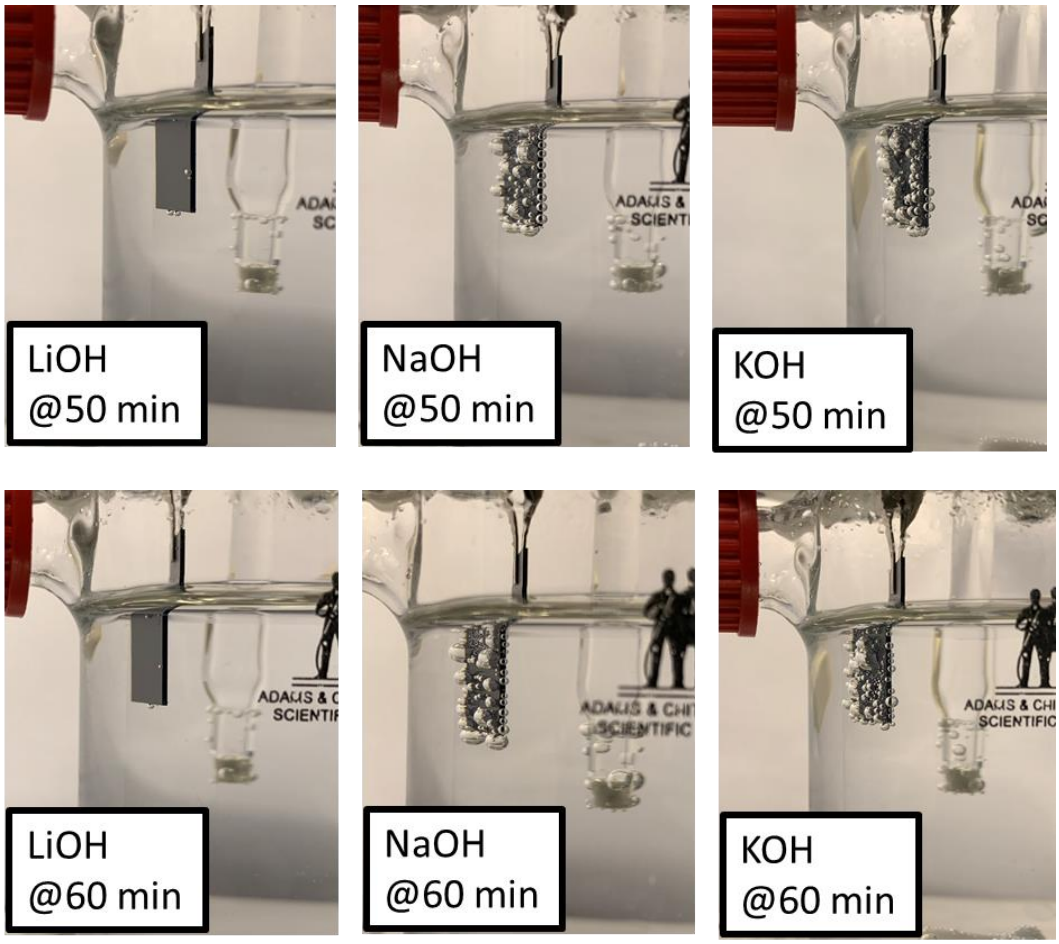

Fig. S3.10: Cont.

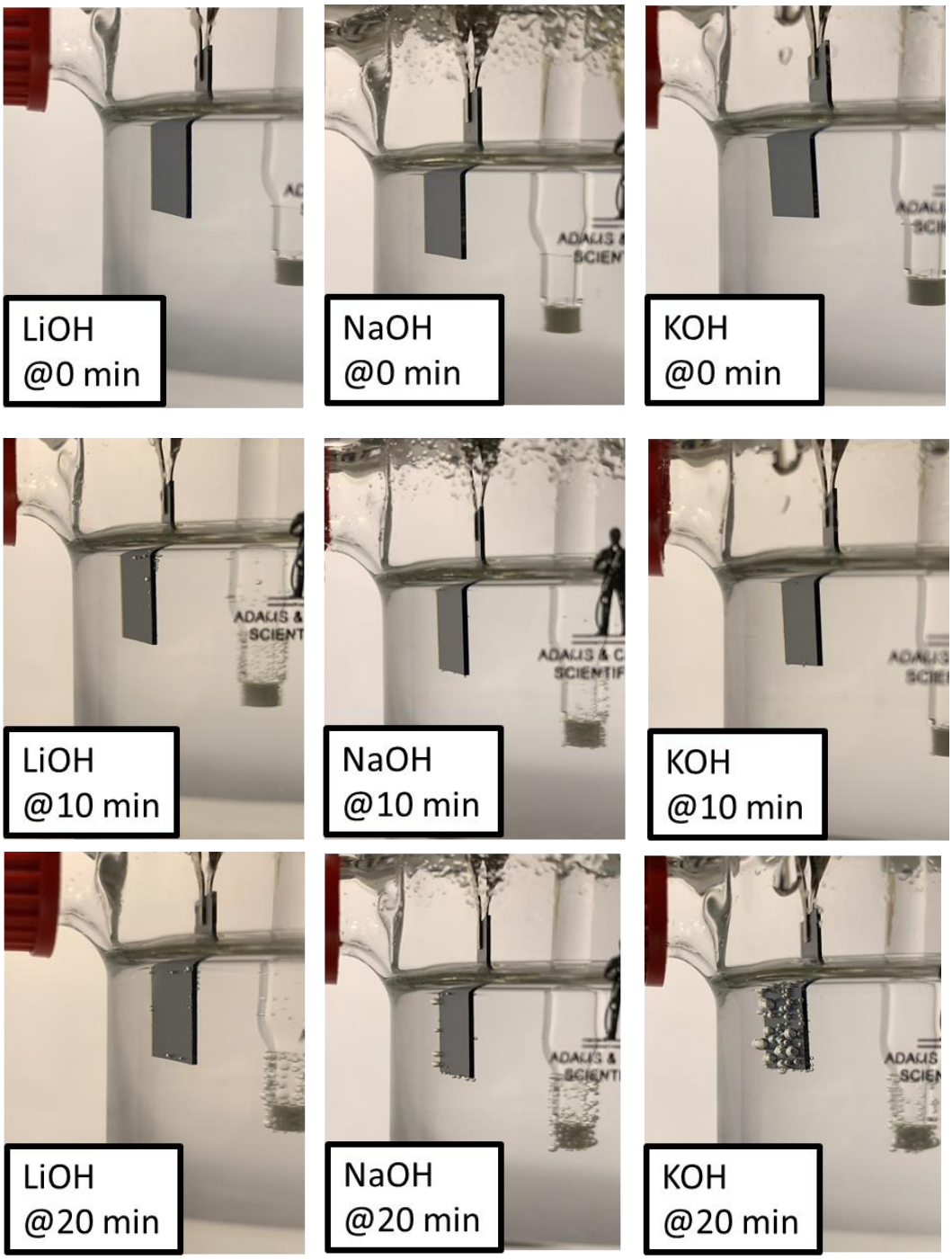

Fig. S3.11: Pictures taken of the Si side when evaluating the $Fe_{20}Ni_{80}$/Si in LiOH, NaOH, and KOH. Except for the picture at 0 min all pictures were taken after a 10 min interval of holding the current density at 10 mA cm^{-2} but before the solution was agitated and the H_2 was measured.

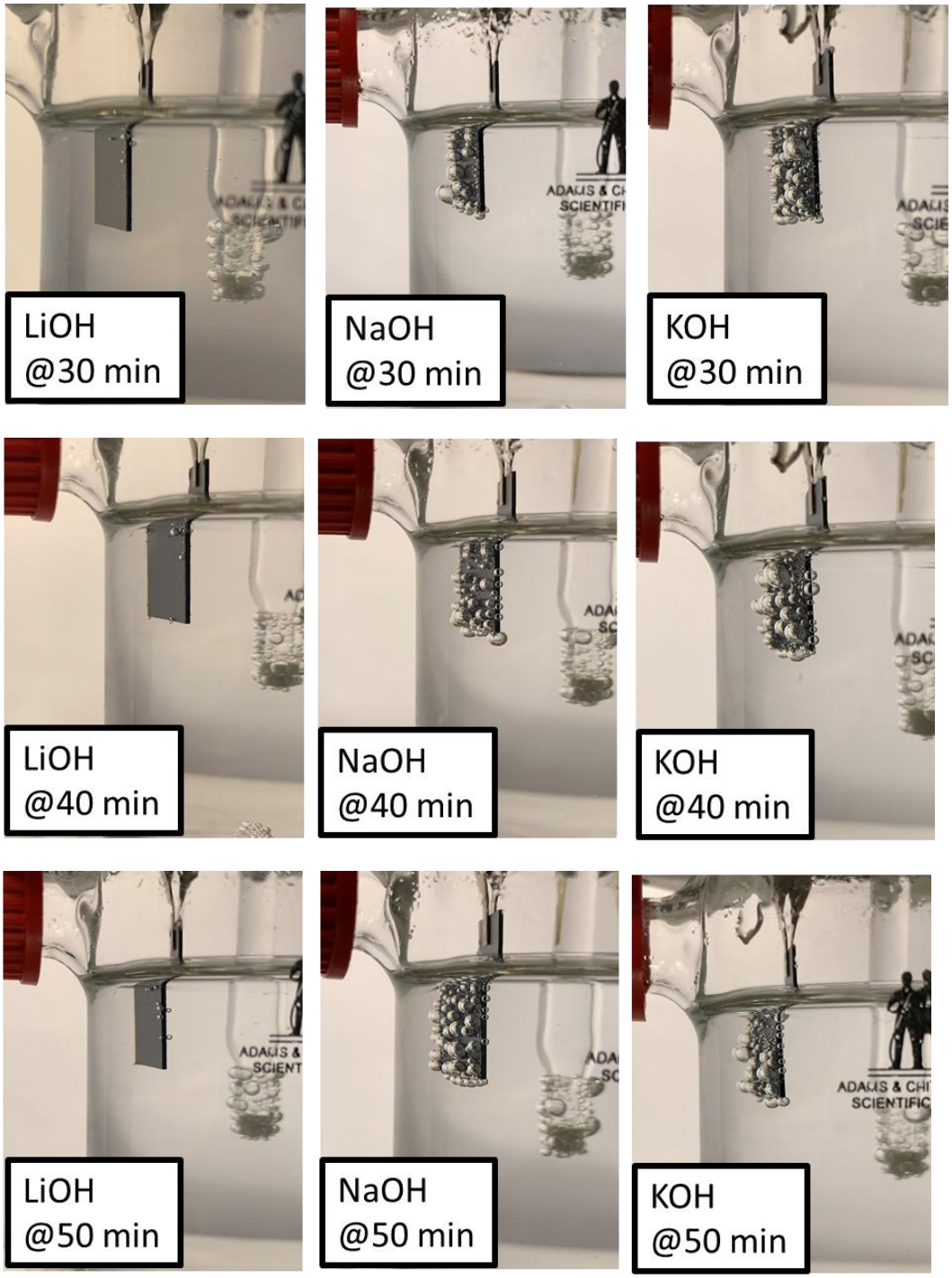

Fig. S3.11: Cont.

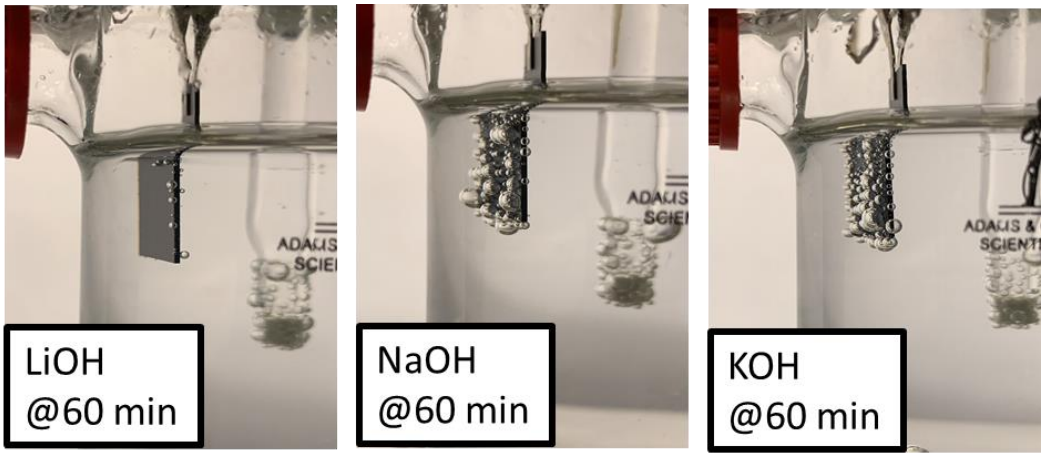

Fig. S3.11: Cont.

Appendix 3. Supplementary information for Hydrogen evolution reaction (HER) under buffered neutral conditions: Evaluation of $Fe_xNi_{100-x}O_y$ electrodes in sodium phosphate electrolyte

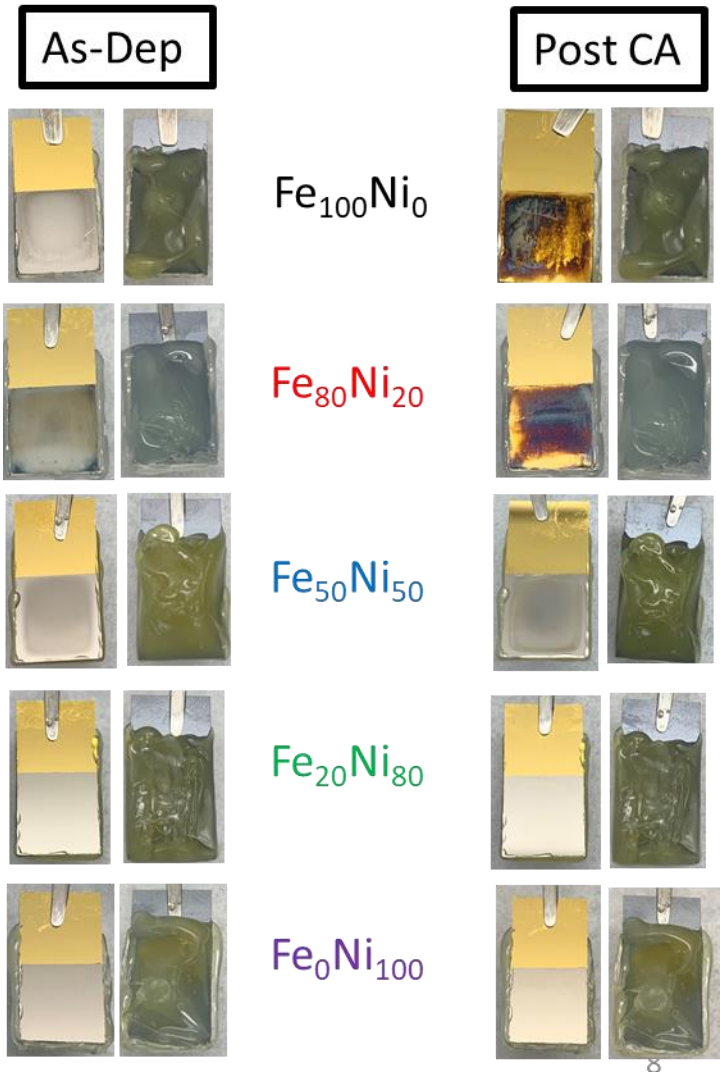

Fig. S4.1. Pictures of $Fe_xNi_{100-x}O_y$ electrodes as-deposited vs. Post-CA.

Table. S4.1. Hydrogen amount measured in the cathode and anode side of the H-cell after a CA at -0.7 V vs. RHE in sodium phosphate 0.1 M of 7.2 pH for 1 h.

Electrode	H_2 (µmol) in Cathode/Working Electrode Chamber	H_2 (µmol) in Anode/Counter Electrode Chamber	Total H_2 (µmol)
$Fe_{100}Ni_0$	165	5	170
$Fe_{80}Ni_{20}$	207	8	215
$Fe_{50}Ni_{50}$	166	9	175
$Fe_{80}Ni_{20}$	73	4	77
Fe_0Ni_{100}	67	4	71

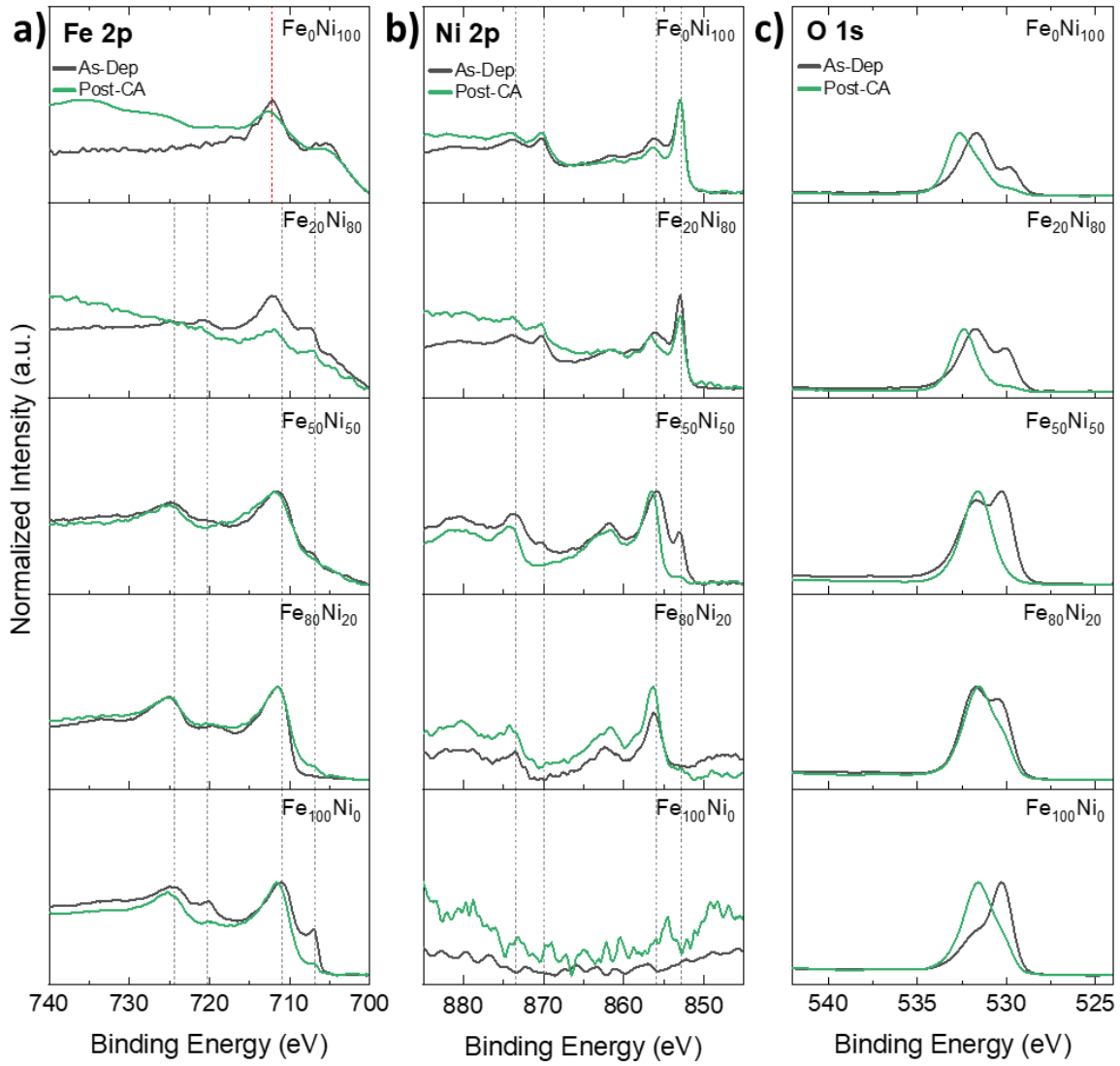

Fig. S4.2. XPS spectra of a) Fe 2p, b) Ni 2p, and c) O 1s for $Fe_xNi_{100-x}O_y$ films as-deposited vs. post-CA no Ar^+ sputtered.

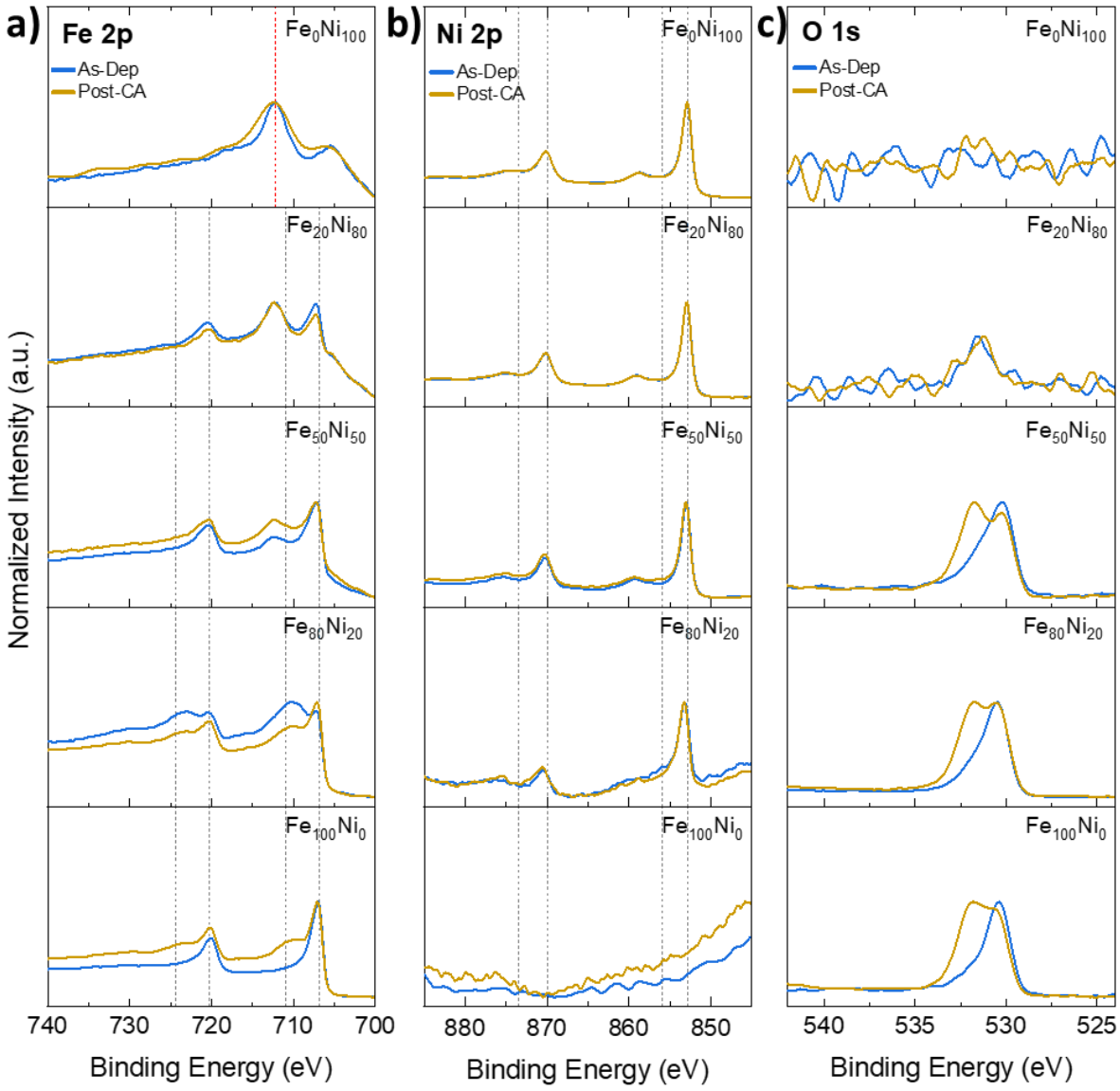

Fig. S4.3. XPS spectra of a) Fe 2p, b) Ni 2p, and c) O 1s for $Fe_xNi_{100-x}O_y$ films as-deposited vs. post-CA after Ar^+ sputtered for 10 min at 1 KeV.

Electrodes with Si exposed ($Fe_xNi_{100-x}O_y$/Si)

Electrodes that had the silicon backside exposed were also tested. The electrodes with the silicon exposed are labeled $Fe_xNi_{100-x}O_y$/Si. The electrochemical activity and stability were evaluated by performing a chronoamperometry at -0.7 V vs. RHE for 1 h in a sodium phosphate buffer solution at a pH of 7.2. The electrochemical experiments were performed in an H-cell where the

electrolyte was mixed at 400 rpm and purged with argon gas. The CA results are presented in Fig. S3. Among the different compositions, we observe that overall, the catalytic activity decreases following $Fe_{80}Ni_{20}$/Si > $Fe_{100}Ni_{0}$/Si > $Fe_{50}Ni_{50}$/Si > $Fe_{20}Ni_{80}$/Si ≈ $Fe_{0}Ni_{100}$/Si. The trend follows the results obtained when only the $Fe_xNi_{100-x}O_y$ was exposed. An increase in the current density was observed for $Fe_{80}Ni_{20}$/Si and $Fe_{100}Ni_{0}$/Si. Unlike in the case when the silicon was covered the current when the silicon is exposed increases consistently over the period tested.

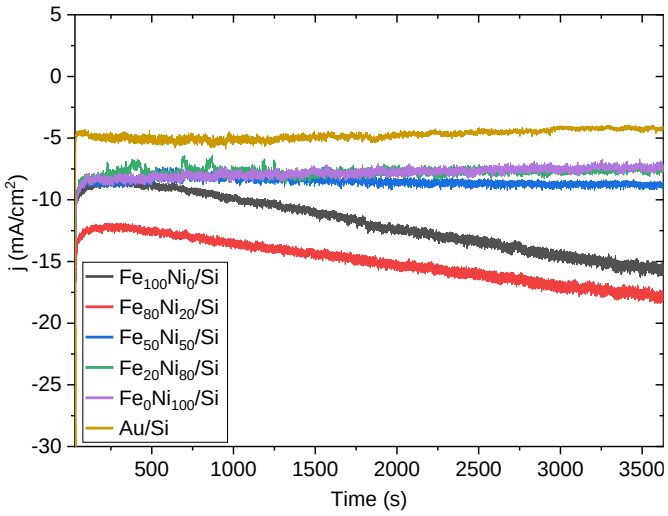

Fig. S4.4. Chronoamperometry results of different $Fe_xNi_{100-x}O_y$/Si performed at -0.7 V vs. RHE in 0.1 M phosphate electrolyte pH of 7.2 at 400 rpm.

Following the CA experiment, the electrodes were removed from the cell, rinsed with DI water, and dried with argon. Pictures of the $Fe_xNi_{100-x}O_y$/Si as-deposited and post-CA are presented in Fig. S5. Visual changes can be observed on the $Fe_xNi_{100-x}O_y$ side of the electrode only for $Fe_{80}Ni_{20}$/Si and $Fe_{100}Ni_{0}$/Si, as shown in Fig. S5. The visual images show that when the silicon was exposed, the loss of the $Fe_xNi_{100-x}O_y$ electrode is not visibly noticeable, unlike in the case when the silicon was covered. Nonetheless, changes on the electrode when the silicon was exposed as-deposited and post-CA can be observed.

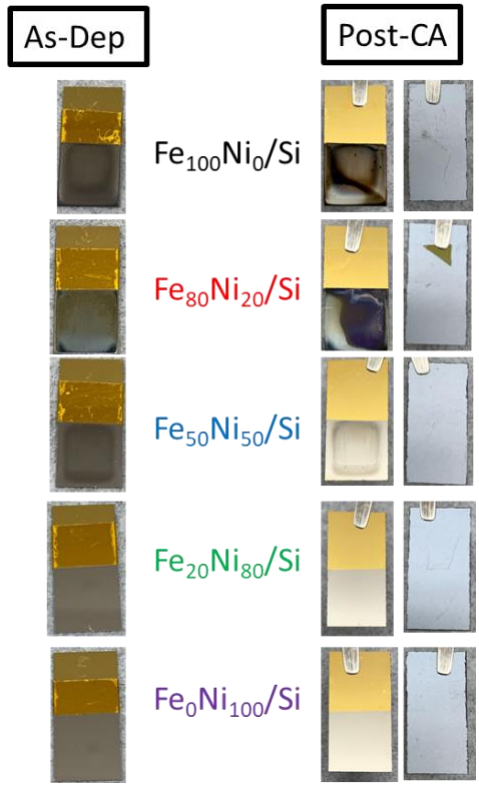

Fig. S4.5. Pictures of $Fe_xNi_{100-x}O_y$/Si electrodes as-deposited vs. post-CA.

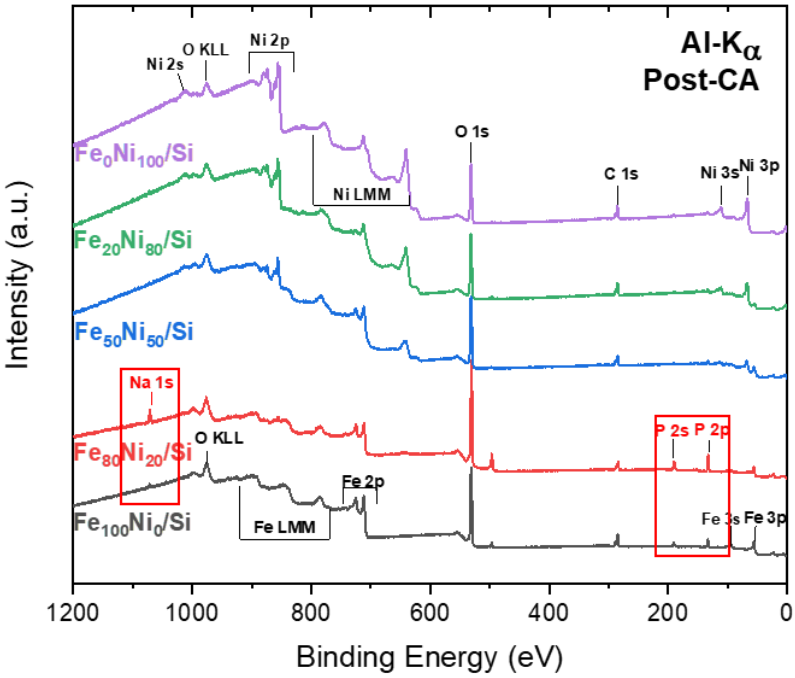

Fig. S4.6. XPS survey spectra of $Fe_xNi_{100-x}O_y$/Si post-CA in 0.1 M sodium phosphate at pH of 7.2 at 400 rpm.